Title: Advanced Hydrogen Transport Membranes for Vision 21 Fossil Fuel Plants

Type of Report: Final

Reporting Period Start Date: October 1, 2000

Reporting Period End Date: March 31, 2006

Principal Authors: Carl R. Evenson, Shane E. Roark

Project Participants:
Eltron Research Inc.: Carl R. Evenson, Harold A. Wright, Shane E. Roark, Richard A. Mackay, Sara L. Rolfe, Richard T. Treglio, Adam E. Calihman
Argonne National Laboratory: U. (Balu) Balachandran
CoorsTek: Richard N. Kleiner, James E. Stephan, Frank E. Anderson
Süd Chemie: Jon P. Wagner, Chandra Ratnasamy
NORAM Engineering & Constructors Ltd.: Clive Brereton, Warren Wolfs, James Lockhart
McDermott Technology Inc.: George Farthing
Oak Ridge National Laboratory: Tim R. Armstrong, Matt K. Ferber

Date Report was Issued: June 30, 2006

DOE Award Number: DE-FC26-00NT40762

Name and Address of Submitting Organization:
Eltron Research Inc., 4600 Nautilus Court South, Boulder, CO 80301-3241

TABLE OF CONTENTS

DISCLAIMER

This report was prepared as an account of work sponsored by an agency of the United States Government. Neither the United States Government nor any agency thereof, nor any of their employees, makes any warranty, express or implied, or assumes any legal liability or responsibility for the accuracy, completeness, or usefulness of any information, apparatus, product, or process disclosed, or represents that its use would not infringe privately owned rights. Reference herein to any specific commercial product, process, or service by trade name, trademark, manufacturer, or otherwise does not necessarily constitute or imply its endorsement, recommendation, or favoring by the United States Government or any agency thereof. The views and opinions of authors expressed herein do not necessarily state or reflect those of the United States Government or any agency thereof.

ABSTRACT

The objective of this project was to develop an environmentally benign, inexpensive, and efficient method for separating hydrogen from gas mixtures produced during industrial processes, such as coal gasification. A family of hydrogen separation membranes was developed including single phase mixed conducting ceramics, ceramic / ceramic composites, cermet membranes, cermet membranes containing a hydrogen permeable metal, and intermediate temperature composite layered membranes. Each membrane type had different operating parameters, advantages, and disadvantages that were documented over the course of the project. Research on these membranes progressed from ceramics to cermets to intermediate temperature composite layered membranes. During this progression performance was increased from 0.01 $mL \bullet min^{-1} \bullet cm^{-2}$ up to 423 $mL \bullet min^{-1} \bullet cm^{-2}$. Eltron and team membranes not only developed each membrane type, but also membrane surface catalysis and impurity tolerance, creation of thin film membranes, alternative applications such as membrane promoted alkane dehydrogenation, demonstration of scale-up testing, and complete engineering documentation including process and mechanical considerations necessary for inclusion of Eltron membranes in a full scale integrated gasification combined cycle power plant. The results of this project directly led to a new $15 million program funded by the Department of Energy. This new project will focus exclusively on scale-up of this technology as part of the FutureGen initiative.

EXECUTIVE SUMMARY

Eltron Research Inc. and team members developed an environmentally benign, inexpensive, and efficient method for separating hydrogen from gas mixtures produced during industrial processes, such as coal gasification. This project was motivated by the National Energy Technology Laboratory (NETL) Vision 21 initiative, which seeks to economically eliminate environmental concerns associated with the use of fossil fuels. The project focused on four basic categories of dense membranes: i) single phase ceramics and mixed conducting ceramic/ceramic composites, ii) mixed conducting ceramic/metal (cermet) composites, iii) cermets with hydrogen permeable metals, and iv) layered composites containing hydrogen permeable alloys. Research on these membranes progressed from ceramics to cermets to intermediate temperature composite layered membranes. During this progression performance was increased from 0.01 $mL \bullet min^{-1} \bullet cm^{-2}$ up to 423 $mL \bullet min^{-1} \bullet cm^{-2}$. Other key aspects of this technology that were developed include surface catalysis, ceramic processing methods, and engineering support to demonstrate inclusion of Eltron hydrogen separation membranes in gasified coal power plants. The results of this project led to a new $15 million program funded by the Department of Energy as part of the FutureGen initiative.

PROJECT SUMMARY

The objective of this project was to develop an environmentally benign, inexpensive, and efficient method for separating hydrogen from gas mixtures produced during industrial processes, such as coal gasification. This project focused on four basic categories of dense membranes: i) single phase ceramics and mixed conducting ceramic/ceramic composites, ii) mixed conducting ceramic/metal (cermet) composites, iii) cermets with hydrogen permeable metals, and iv) layered composites with hydrogen permeable alloys. In addition to optimizing membrane compositions to enable practical hydrogen separation rates and chemical stability, other key aspects of this technology developed include surface catalysis, ceramic processing methods, separation of hydrogen under high pressure, and engineering support to demonstrate inclusion of Eltron hydrogen separation membranes in gasified coal power plants. To achieve these technical goals, Eltron Research Inc. organized a consortium of relevant companies and national laboratories. The companies involved in this consortium changed throughout the project. The companies involved included CoorsTek, McDermott Technology Inc., Süd Chemie, Argonne National Laboratory, Oak Ridge National Laboratory, and NORAM Engineering & Constructors Ltd.

Key project results were as follows:

Ceramic Hydrogen Separation Membranes

- Single phase perovskite based hydrogen separation membranes were prepared as mixed proton and electron conductors. Ceramic membranes operated at 700 to 950°C, had an ambipolar conductivity less than 1 x 10^{-4} S/cm, and an observed permeation rate of 0.01 mL•min^{-1}•cm^{-2}.
- Ceramic / ceramic composites were prepared containing a proton conducting ceramic phase and an electron conducting phase. For a selected perovskite mixed proton/electron conducting ceramic with the general composition $AB_{(1-x)}B'_xO_{3-\delta}$, maximum ambipolar conductivity of 5 x 10^{-3} S/cm was achieved for x = 0.3. Ceramic / ceramic composites were tested at temperatures between 700 and 950°C and had an observed permeation rate of 0.1 mL•min^{-1}•cm^{-2}.
- Ceramic membranes exhibited high tolerance to potential feed stream poisons and had low manufacturing costs.

Cermet Hydrogen Separation Membranes

- To increase electronic conductivity cermet membranes were prepared with a ceramic proton conducting phase and a metal electron conducting phase.
- For cermets, continuity of the metal phase was observed for all samples between 38 and 48 wt.% metal. However a maximum in hydrogen transport and conductivity was achieved at a metal phase content of 44 wt.%.
- Cermet membranes were tested between 700 and 950°C, had an ambipolar conductivity up to 1 x 10^{-2} S/cm, and a permeation rate of 1.0 mL•min^{-1}•cm^{-2}.

- Cermet permeation was increased by replacing the electron conducting metal with a hydrogen permeable metal. This allowed lowering the operating temperature to 550°C and resulted in a permeation rate of 4.0 $mL \bullet min^{-1} \bullet cm^{-2}$.
- Mechanical testing results indicated higher material strength and improved Weibull modulus for cermets relative to ceramics.
- Preparation of a novel cermet referred to as EC101 containing a high permeability metal was initiated. Cermet disks were prepared with distinct ceramic and metal phases with less than 1% porosity. Permeability was measured under ambient pressure conditions.

Thin Film Hydrogen Separation Membranes

- Dense thin films of BCY / Ni were deposited on the inner surface of porous BCY / Ni closed-one-end tubes. Thicknesses between 20 and 100 microns were found depending on thin film deposition conditions.

Intermediate Temperature Composite Layered Hydrogen Separation Membranes

- Composite layered hydrogen separation membranes were prepared that allowed operating temperatures as low as 320°C. Composite layered membranes are dense and produce 99.999% pure H_2.
- Under ambient pressure feed conditions, permeation rates of 20-25 $mL \bullet min^{-1} \bullet cm^{-2}$ were observed. With pressurized feed streams higher permeation rates were observed up to 423 $mL \bullet min^{-1} \bullet cm^{-2}$.
- Composite layered membranes are compatible with water gas shift reactor temperatures and require desulfurization of feed stream gases.
- Membrane mass transfer limitations were overcome by improving flow dynamics and gas flow rates within high pressure reactors.
- Composite layered membranes were tested at 400°C and 300 psig of a 40% hydrogen feed stream for up to 400 hours. Permeation greater than 50 $mL \bullet min^{-1} \bullet cm^{-2}$ was observed after 400 hours.
- Permeation of composite layered membranes was measured at feed side pressures up to 1010 psig.

Membrane Stability

- Catalysts were prepared to maximize hydrogen dissociation and hydrogen desorption on respective sides of the membrane. Catalysts were designed for sulfur tolerance.
- Membrane stability was tested with CO_2, H_2O (steam), H_2S and CO. Hydrogen separation membranes exhibited tolerance to CO_2 and steam but performance decreased upon exposure to hydrogen sulfide or carbon monoxide.

Engineering Development

- A process report was prepared for evaluation of the criteria for incorporation of Eltron hydrogen separation membranes into IGCC power plants.

- Five flow sheets were prepared for Eltron's membranes operating under various conditions.
- A mechanical report was prepared of design criteria and manufacturing concepts for pilot and full scale hydrogen separators.
- An evaluation matrix was prepared to rank each of Eltron's different membrane types as well as competing technologies.
- A process and control document was prepared for a hydrogen separation system utilizing multiple separator units.
- A cost estimate was prepared for a complete, installed hydrogen separation system.

Alkane Dehydrogenation

- Alkane dehydrogenation was accomplished in a catalytic membrane reactor, and the ratio of olefin to alkane increased with increasing temperature. A maximum H_2 transport rate 0.009 $mL \bullet min^{-1} \bullet cm^{-2}$ was measured at 800°C.
- Membrane promoted alkane dehydrogenation was tested as a function of catalyst surface area.

Membrane Scale-Up Demonstration

- A scale-up reactor was designed and constructed.
- A composite layered membrane was tested with a 15-fold scale up in surface area. The membrane had a surface area of 31.7 cm^2 and had a measured permeation rate of 51 $mL \bullet min^{-1} \bullet cm^{-2}$.

RESULTS AND DISCUSSION

The work plan for this project was divided into nine tasks:

Task 1 *Preparation & Characterization of Membrane Materials*
Task 2 *Evaluation of Hydrogen-Transport Membranes*
Task 3 *High-Pressure Hydrogen Separation*
Task 4 *Thin-Film Hydrogen Separation Membranes*
Task 5 *Construction & Evaluation of Prototype Hydrogen Separation Unit*
Task 6 *Membrane-Promoted Conversion of Alkanes to Olefins*
Task 7 *Candidate Membrane Compositions for Scale Up*
Task 8 *Manufacturing Processes for Demonstration-Scale Hydrogen Separation Membranes*
Task 9 *Fabrication and Evaluation of Demonstration-Scale Hydrogen Separation Unit*

Work in each task is described in detail below.

I. Tasks 1 & 2 Preparation, Characterization, and Evaluation of Hydrogen-Transport Membranes

Contributors: Eltron, CoorsTek, ANL

Over the course this project, five different types of hydrogen separation membranes were prepared, characterized and evaluated for hydrogen separation performance. Hydrogen separation membranes developed included single phase ceramics, ceramic / ceramic composites, high temperature cermets, cermets containing a hydrogen permeable metal, and finally intermediate temperature composite layered membranes. All membrane types were composed of a dense ceramic, metal, or cermet that conducted protons or hydrogen atoms across the membrane. Figure 1 shows schematically the general concept for how these membranes work. Both sides of the membrane contain a catalytic surface. On the feed or retentate side of the membrane a good hydrogen dissociation catalyst is needed. H_2 is oxidized to two hydrogen protons at high pressure. On the low pressure sweep or permeate side of the membrane hydrogen is reduced back to H_2. This catalyst must be a good hydrogen desorption catalyst to promote rapid removal of H_2 from the membrane surface. The membrane itself conducts hydrogen by one of two different mechanisms. Single phase ceramics, ceramic / ceramic composites, and high temperature cermets separate hydrogen from a mixed feed stream based on a Nerstian driving force. In this case hydrogen is conducted across the membrane as protons. Cermets containing a hydrogen permeable metal and intermediate temperature composite layered membranes separate hydrogen based on the difference in hydrogen partial pressure across the membrane. In this case it is generally accepted that hydrogen is conducted across the membrane as hydrogen atoms; however, this is currently under debate. The difference between these hydrogen separation mechanisms is significant and described in detail below.

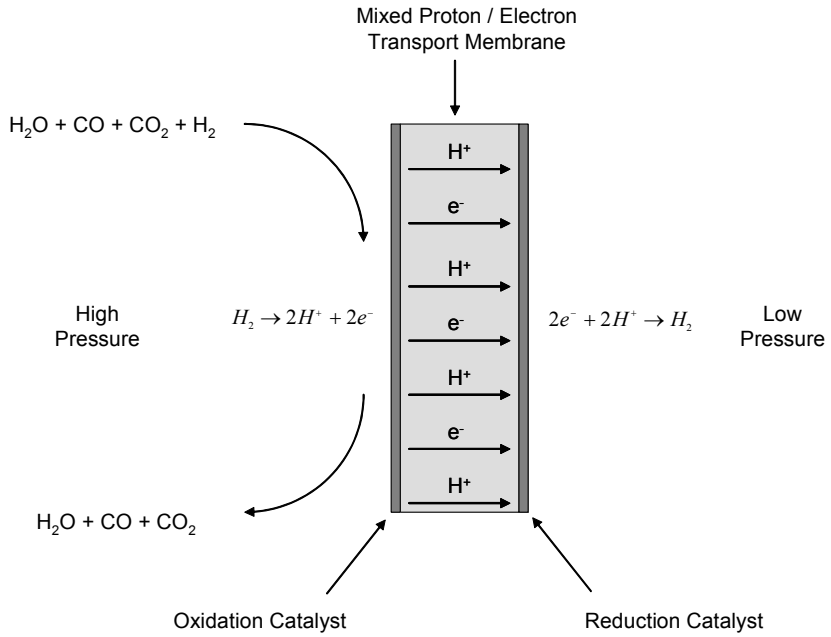

Figure 1. General schematic of the hydrogen separation process using Eltron's family of hydrogen separation membranes.

Hydrogen Separation Based on a Nerstian Driving Force

Hydrogen transport through dense high-temperature ceramic membranes is limited by mixed proton and electron conduction, which is referred to as ambipolar conductivity, σ_{amb} (S/cm). Membrane proton and electron conductivity, σ_{H+} and σ_{e-}, is proportional to σ_{amb} according to the relationship,

$$\frac{1}{\sigma_{amb}} \propto \frac{1}{\sigma_{H+}} + \frac{1}{\sigma_{e-}} \tag{1}$$

Based on this relationship if the electron conductivity is very high, then $\sigma_{amb} \sim \sigma_{H+}$. The apparent σ_{amb} was calculated according to,

$$\sigma_{amb} = \frac{JnFt}{E} \tag{2}$$

where J is the measured permeation, n is the number of moles of charge carrier per mole of hydrogen, F is Faraday's constant, t (cm) is the membrane thickness, and E is the Nernst potential across the membrane. The Nernst potential was calculated from,

$$E = -\frac{RT}{nF} \ln \frac{C_{H2,out}}{C_{H2,in}} \tag{3}$$

where R is the gas constant, T is temperature, and $C_{H2,out}$ and $C_{H2,\ in}$ are the concentrations of hydrogen in the outlet and inlet streams of the reactor. Since σ_{amb} accounts for the membrane thickness and hydrogen concentration gradient, it is a convenient parameter for comparing the performance of membranes tested under different conditions.

Hydrogen Separation Based on a Hydrogen Partial Pressure Driving Force

The mechanism for hydrogen transport through membranes containing hydrogen permeable metals is fundamentally different than for ceramics. Membrane permeability, P ($mol \bullet m^{-1} \bullet s^{-1} \bullet Pa^{-x}$), is used rather than σ_{amb} to characterize performance. Permeability was calculated according to,

$$P = \frac{Jt}{p_f^x - p_s^x} \tag{4}$$

where p^x_f and p^x_s are the hydrogen partial pressures on the feed and sweep sides, respectively. It was assumed that the exponent x is ½ according to Sieverts' Law; however, significant deviation from the square root dependence can occur when permeation is limited by surface kinetics or mass transport.[1] An important distinction between these two categories of membranes is apparent by comparing Equations 3 and 4. For proton-conducting ceramic membranes, hydrogen

transport is dependent on the *ratio* of hydrogen concentrations on opposite sides of the membrane; whereas, for membranes with hydrogen permeable metals transport is dependent on the *difference* in concentrations.

For all membranes tested in this project, hydrogen permeation, J ($mL \bullet min^{-1} \bullet cm^{-2}$), was calculated according to,

$$J = \left[C_{H2,out} - C_{He,out} \left(\frac{C_{H2,in}}{C_{He,in}} \right) \right] F_T \frac{1}{A} \qquad (5)$$

where $C_{H2,out}$, $C_{He,out}$, $C_{H2,in}$, and $C_{He,in}$ are the concentrations (volume fraction) of hydrogen and helium in the outlet sweep stream and inlet feedstream, respectively, F_T is the total flow rate (mL/minute) on the sweep side, and A is the membrane area (cm^2). The concentration of hydrogen in inlet and sweep streams was determined using a Shimadzu GC 14-A with a Carbosphere 80/100 column (Alltech) and thermal conductivity detection. Argon was used as the carrier gas to maximize sensitivity to hydrogen. Equation 5 corrects the hydrogen permeation rate for leaks, if any, by subtracting the permeate helium (adjusted for the relative inlet concentrations of hydrogen and helium). In this equation, it is assumed that hydrogen and helium leak at the same rate, which was not necessarily true for the small leaks typical in these types of experiments. Therefore, only data obtained with leak rates less than a few percent of the total hydrogen permeation rate are presented for high-temperature samples, and only leak-free data are presented for intermediate temperature layered composite membranes. The performance observed and key advantages / disadvantages for all five membrane types are summarized in Table 1 for each membrane type.

Table 1 clearly shows the development of Eltron's family of hydrogen separation membranes as the project progressed. Single phase ceramics were the first type of hydrogen separation membrane tested. These were ceramics compounds with a perovskite (ABO_3) structure. Doping on the A and/or B sites allowed perovskite ceramics to simultaneously conduct protons and electrons. This conduction process was thermally activated. Ceramic membranes performed best at high temperatures between 700 and 950°C although the best performance was only on the order of 0.01 $mL \bullet min^{-1} \bullet cm^{-2}$. It was determined that low conductivity of electrons across the membrane was limiting the hydrogen separation performance. To improve electron conductivity ceramic / ceramic composites were prepared that contained a perovskite ceramic phase which conducted protons and a second transition metal oxide phase which conducted electrons across the membrane. These ceramic / ceramic composites still operated at high temperatures and a ten fold increase in hydrogen permeation to 0.1 $mL \bullet min^{-1} \bullet cm^{-2}$ was observed. It was rationalized that the electron conductivity could be increased further by replacing the transition metal oxide phase with a metal such as nickel. These cermets still utilized a perovskite ceramic phase to conduct protons across the membrane and therefore the best permeation was observed at high temperatures. Permeation rates up to 1.0 $mL \bullet min^{-1} \bullet cm^{-2}$ were observed. In addition these materials possessed a higher mechanical strength than pure ceramic membranes. At this point in the evolution of Eltron's hydrogen separation membranes a fundamental switch was made to membranes whose performance was based on a partial pressure hydrogen driving force rather than a Nerstian driving force. By replacing metallic nickel with a metal that was permeable to hydrogen such as palladium a four fold increase in permeation up to 4.0 $mL \bullet min^{-1} \bullet cm^{-2}$ was achieved. In this type of cermet the

metallic palladium was responsible for both hydrogen and electron conduction and the ceramic phase provided a mechanical support for the metal. Since the hydrogen separation mechanism was no longer thermally activated these membranes could be operated as low as 550°C. While these palladium cermets possessed a permeation advantage, the high cost of palladium would likely prevent their use on a large scale. This finally led Eltron to low cost layered metal alloy hydrogen separation membranes. These membranes operated at 320-440°C which is consistent with water-gas-shift (WGS) and impurity clean-up temperatures in gasified coal feed streams. The performance of these membranes was unparalleled and permeation rates as high as 423 $mL \bullet min^{-1} \bullet cm^{-2}$ were achieved. Eltron Research Inc. focused almost exclusively on this type of membrane during the final two years of the project. Results led directly to a new $15 million program funded by the Department of Energy as part of the FutureGen initiative. The synthesis, characterization, development, and evaluation of each of these types of membranes is described in detail below.

Four ambient pressure hydrogen separation units were constructed for membrane evaluation. A schematic diagram for two of the membrane evaluation units is shown in Figure 2, and a photograph is shown in Figure 3. The hydrogen-separation cells are positioned inside the furnaces using appropriate Swagelok fittings to join the quartz tubing to stainless steel inlet and outlet tubing. The concentrations of the constituents of the inlet hydrogen-rich gas stream (*e.g.,* syngas) were adjusted at a flow control manifold, then introduced through the top of the separation cell. Humidity can be introduced by flowing the gas through a temperature-controlled water bubbler, and measured using an in-line humidity sensor. A diagram of the hydrogen separation cell is shown in Figure 4. When testing tubular membranes a seal was formed between the membrane and an alumina cup by heating crushed Pyrex above the melting temperature under a flow of argon. When testing planar samples the sealing mechanism was changed to a mechanical seal formed at room temperature. During evaluation, a hydrogen inlet stream is passed through the separation cell, where hydrogen is transferred across the membrane into the sweep chamber. Argon sweep gas enters the sweep chamber through an inner gas line concentric with a larger exit line, and the separated hydrogen and sweep gas exit the cell through the outside exit line. Sampling of inlet and outlet streams was achieved through ports located just outside the furnaces. Flow rates for the evaluations were between 30 and 100 mL/min on each side of the membrane. Reactors for testing membranes at high pressure are described in Task 3.

Table 1.
Summary of Hydrogen Separation Membrane Characteristics.

Membrane Type	Thickness (mm)	Operation Temperature (^oC)	Observed Max. Separation Rate ($mL \cdot min^{-1} \cdot cm^{-2}$)	Ambipolar Conductivity (S/cm)	Permeability ($mol \cdot m^{-1} \cdot s^{-1} \cdot Pa^{-0.5}$)	Potential Advantages	Potential Disadvantages
Single Phase Ceramic	0.1 to 0.5	700 to 950	0.01	$< 1 \times 10^{-4}$	N/A	• Inexpensive • Resistant to poisons	• Low H_2 Flux • Brittle
Ceramic / Ceramic	0.1 to 0.5	700 to 950	0.1	1×10^{-4} to 5×10^{-3}	N/A	• Inexpensive • Resistant to poisons	• Low H_2 Flux • Brittle
Cermet	0.1 to 0.5	700 to 950	1.0	2×10^{-4} to 1×10^{-2}	N/A	• Better H_2 flux than pure ceramics • Inexpensive • Integrated catalyst • Less Brittle	• Susceptible to poisons • Lower H_2 flux than H_2 permeable metal
Cermet w/ H_2 Permeable Metal	0.1 to 0.5	550 to 950	4.0	N/A	$\sim 10^{-8}$ (600 to 950^{o}C)	• High H_2 flux • Integrated catalyst • Less Brittle	• Expensive • Susceptible to poisons
Composite Layered Membrane	0.05 to 0.5	320 to 440	423	N/A	$\sim 10^{-7}$ (320 to 440^{o}C)	• Highest H_2 flux • Compatible with WGS and desulfurization	• Susceptible to poisons • Difficult to fabricate

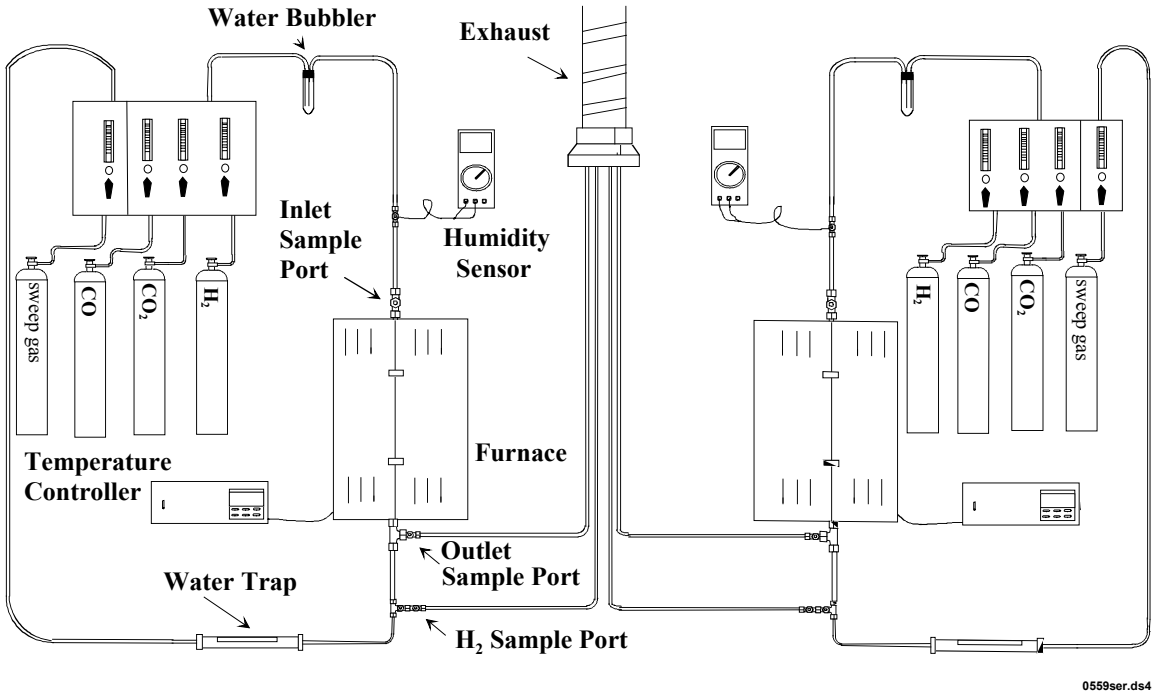

Figure 2. **Schematic diagram of the apparatus used for hydrogen separation membrane evaluation.**

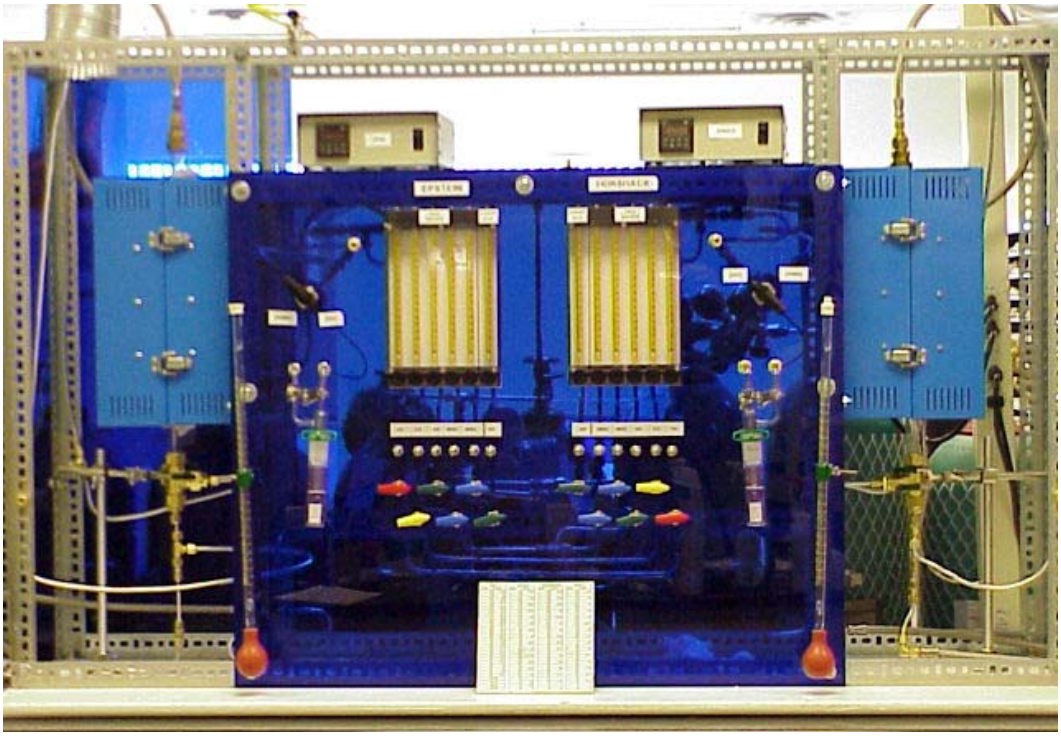

Figure 3. **Photograph of the apparatus for ambient pressure hydrogen separation membrane evaluation.**

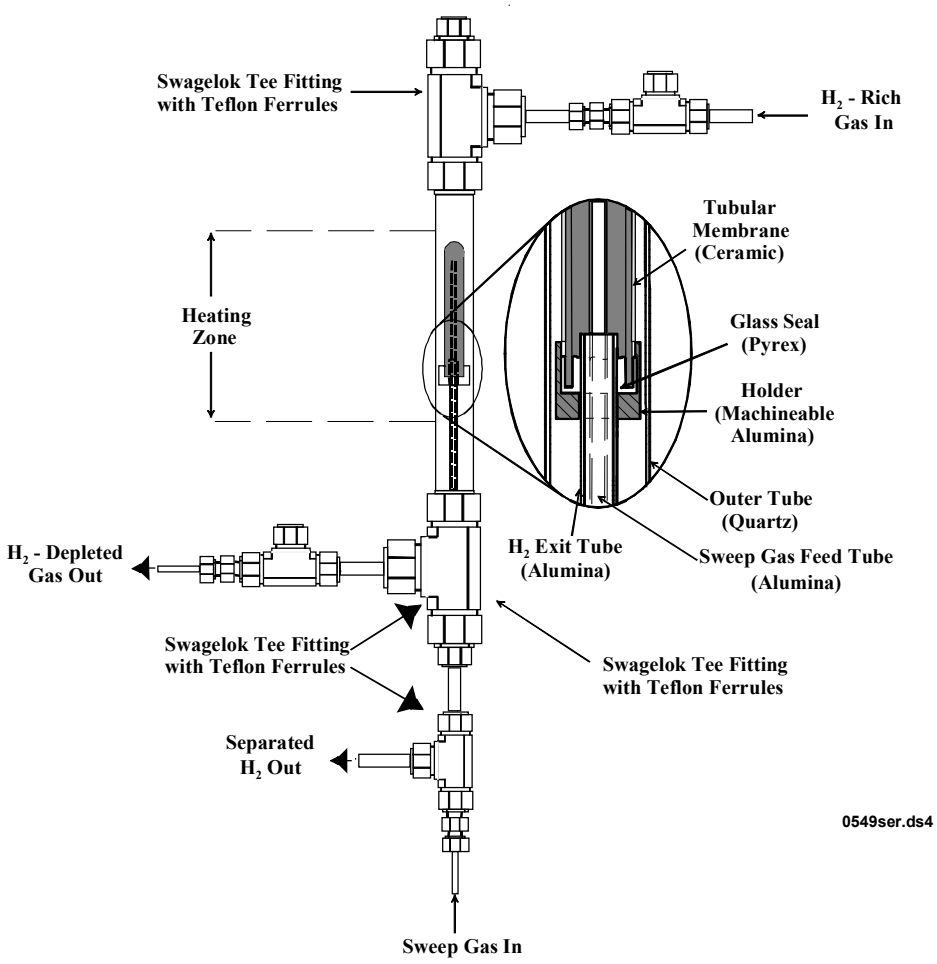

Figure 4. Schematic diagram of the hydrogen separation cell.

A. Single Phase Ceramics

1. Preparation of Ceramic Powders & Fabrication of Membranes

Ceramic powders were prepared by combining oxide precursors in the appropriate stoichiometric ratio with several yttria-stabilized zirconia (YSZ) grinding media. The mixtures were thoroughly ground by ball milling for approximately 24 hours, then passed through a 355-μm sieve, and placed in an alumina crucible for calcination to achieve the desired perovskite composition. Samples were calcined between 1200° and 1400°C for approximately 6 hours in air, then again sieved to 355 μm. Powder particle size was reduced by attrition using a Union Process Model 01 Attritor. Spherical YSZ grinding media and isopropanol were included in the tank during attrition to promote grinding of the precursor powders. After attrition, isopropanol was evaporated, and powders were passed through, respectively, 355-μm, 90-μm, and 38-μm sieves.

Tubular membranes with one closed end were prepared from the powders described above. The general procedure was to obtain an appropriate weight of the powder materials and add 2 wt.% of polyvinyl butyral (PVB) binder using isopropanol as a solvent. The solvent was

evaporated from the powder/binder mixtures, and the powders were passed in series through 355-µm, 90-µm, and 38-µm sieves. Ceramic membrane tubes were prepared by molding under isostatic pressure using a Fluitron CP2-10-60 isostatic press. For each tube, the necessary amount of powder (~10 g) was poured into a rubber mold (Trexler Rubber Co.) containing a stainless steel mandrel. The assembly was placed into the isostatic press, de-aerated by vacuum, and formed at 20,000 psi for two minutes. After depressurization, the mold was removed from the press, and the 'green' tube removed from the mold. Tubes were placed on a bed of powder of the same composition in a ceramic boat (Coors Ceramics) and the binder material was burned out by heating in air at 1°C/min to 600°C. Tubes then were heated at 3°C/min to the desired sintering temperature and maintained for 4 hours, followed by cooling to 500°C at 1°C/min, then to room temperature at 5°/min. The sintering temperatures were between 1400°C and 1600°C. Densities were measured using the Archimedes method.

Disk membranes were prepared by pouring ~2 g of material powder into a die, and pressing uniaxially at 15,000 psi for ~30 seconds. The disks were sintered as described above, and had diameters of ~10 mm and a thickness between 1 and 5 mm.

Tables 2 and 3 contain a summary of preparation conditions and characteristics for several ceramic powders tested.

Table 2.
Summary of Membrane Preparation Conditions and Characteristics.

Material	Calcine Temp. (^{o}C)	Ave. Particle Size (µm)	Sintering Temp. (^{o}C)	Sintering Time (hr)	Density (g/cm^3)	Phase Purity
H01-01	1200	0.996	1475	4	6.287	>98%[1]
H02-01	1250	0.785	1475	4	6.237	>85%[1]
H04-01	1225	0.439	1475	4	6.126	>92%[1]
H04-03	1225	0.624	1475	4	n/a	>92%[1]
H05-01	1350	0.562	1475	4	n/a	2nd Phase[2]
H07-01	1300	1.073	1475	4	5.588	2nd Phase[2]
H10-02	1250	0.612	1275	6	n/a	2nd Phase[2]

[1] Approximate amount of perovskite phase, remainder is unidentified second phase.
[2] Second phase is identified additional reaction product in amounts greater than 5%.

Table 3.
Summary of Membrane Crystallographic Data.

Material	Analysis State	a (Å)	Theoretical Density (g/cm^3)[1]	Second Phase[2]
H01	Sintered	4.393(1)	6.28	Minimal
H02	Sintered	4.394(2)	6.24	Unidentified
H03	Sintered	4.395(1)	6.18	Unidentified
H04	Sintered	4.395(1)	6.00	Unidentified
H05	Sintered	4.188(2)	6.06	K_2NiF_4, SM
H07	Sintered	Orthorhombic	5.39	K_2NiF_4, SM
H10	Sintered	4.399(1)	6.16	$ATO_{2.5}$

[1] Reported theoretical density of the perovskite phase. Not representative for mixed phase materials.
[2] K_2NiF_4 is the parent structure for these secondary phases, SM = starting material, $ATO_{2.5}$ is a second phase formed between the A-site cation and the transition metal dopant.

The compositions are represented by H01, H02, etc., and the two-digit appendage indicates the batch number. The materials were perovskite based with the general formula $AB_{1-x}B'_xO_{3-\delta}$. Comparing results for materials H01 (x = 0.05), H02 (x = 0.3), and H04 (x = 0.1) indicated that as the level of dopant increased, there was a decrease in perovskite phase purity. This trend also was observed by comparing lattice parameters of the three materials in Table 3. The lattice parameters were essentially equivalent, which suggested that the perovskite phase contained the same level of transition metal doping, while the remainder of the dopant formed an unidentified second phase. Density measurements were obtained for three to twelve samples of each composition using the Archimedes' method, and the results are shown in Figure 5. The un-doped perovskite (not shown) had a density of 5.87 ± 0.03 g/cm^3; thus, addition of a transition metal dopant significantly increased sample density. However, the greatest increase in density was attained for the sample with x = 0.05, and further doping decreased density concurrent with the emergence of the second crystallographic phase. At the highest transition metal level (x = 0.3) there was an increase in density and, as indicated above, an additional phase was present in the XRD pattern.

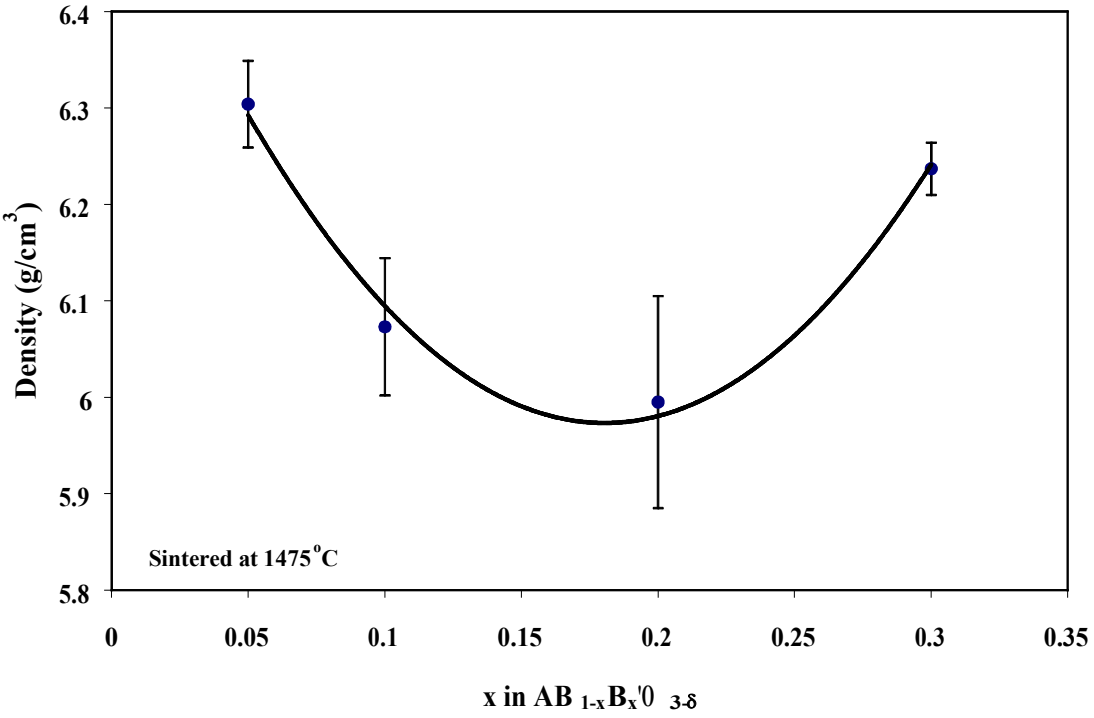

Figure 5. **Plot showing the effect of transition metal doping level on sample density. The error bars represent ±1σ from 3 to 12 measurements using the Archimedes method. All samples were sintered at 1475°C for 4 hours.**

There was very good agreement between the measured densities listed in Table 2 and the theoretical densities in Table 3. In most cases, the theoretical density was slightly lower than the experimental value due partly to the presence of a second phase. For two-phase samples, the theoretical perovskite density was not representative of the entire experimental sample. The results in the tables suggested that the materials were at least 95% dense, with the exception of H07. The second-phase portion of H07 was too large to make this determination.

A representative scanning electron microscope (SEM) image is shown in Figure 6, and the average grain diameter for each sample is plotted as function of doping level in Figure 7. The grain sizes were roughly between 20 and 40 μm in diameter, and as evident in the plot, there was no apparent relationship between grain size and doping level. Also, there were no obvious qualitative differences in the grain shapes.

The coefficient of thermal expansion (CTE) was determined for each sample using sections of tube membranes between 6 and 18 mm in length. Heating and cooling cycles were performed between 100° and 950°C at 5°C/min under nitrogen. Below about 600°C, there was considerable hysteresis in the curves for heating and cooling. However, at higher temperatures the CTE measurements were fairly stable. Figure 8 summarizes the expansion characteristics at 800°C as a function of dopant level. The values represent the averages of one heating and two cooling cycles. Although the CTE values between x = 0.5 and 0.2 were the same within error, the CTE was significantly lower at x = 0.3.

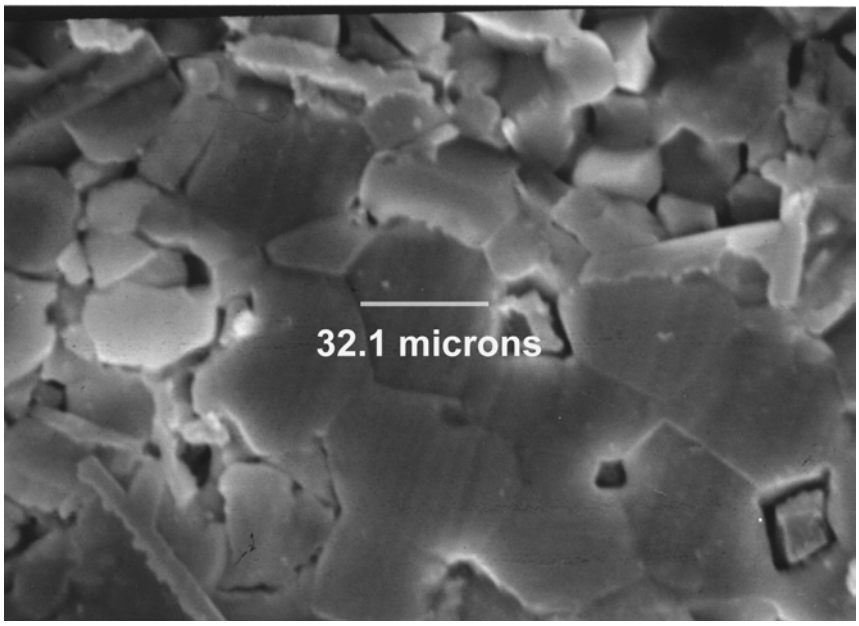

Figure 6. SEM image showing grain sizes for a representative dense ceramic hydrogen transport membrane.

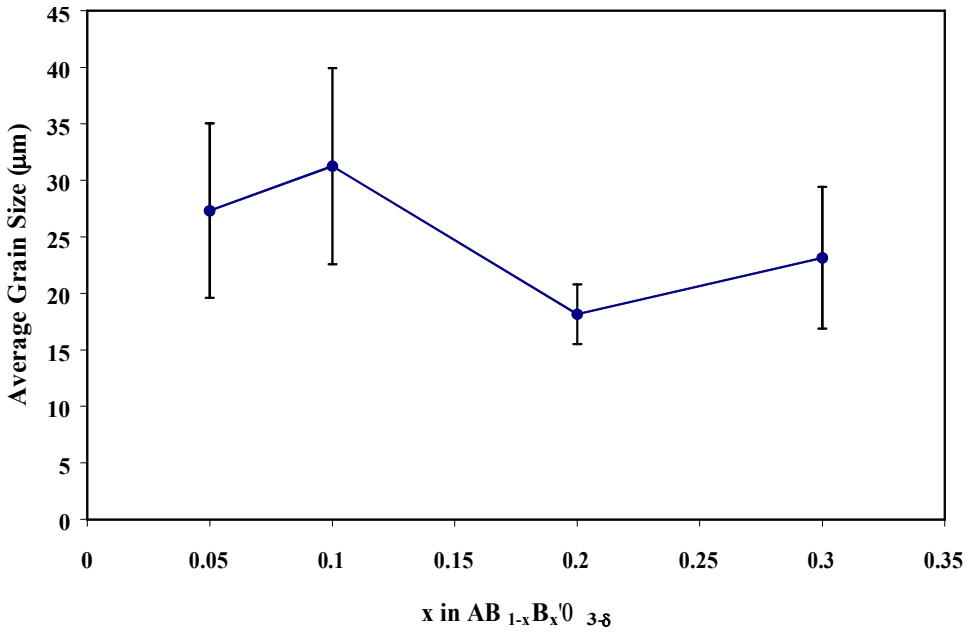

Figure 7. **Plot showing grain diameter as a function of doping level for dense ceramic hydrogen transport membranes. The grain sizes are averages from 10 to 15 grain measurements for each sample, and the error bars (±1σ) represent the range in grain sizes.**

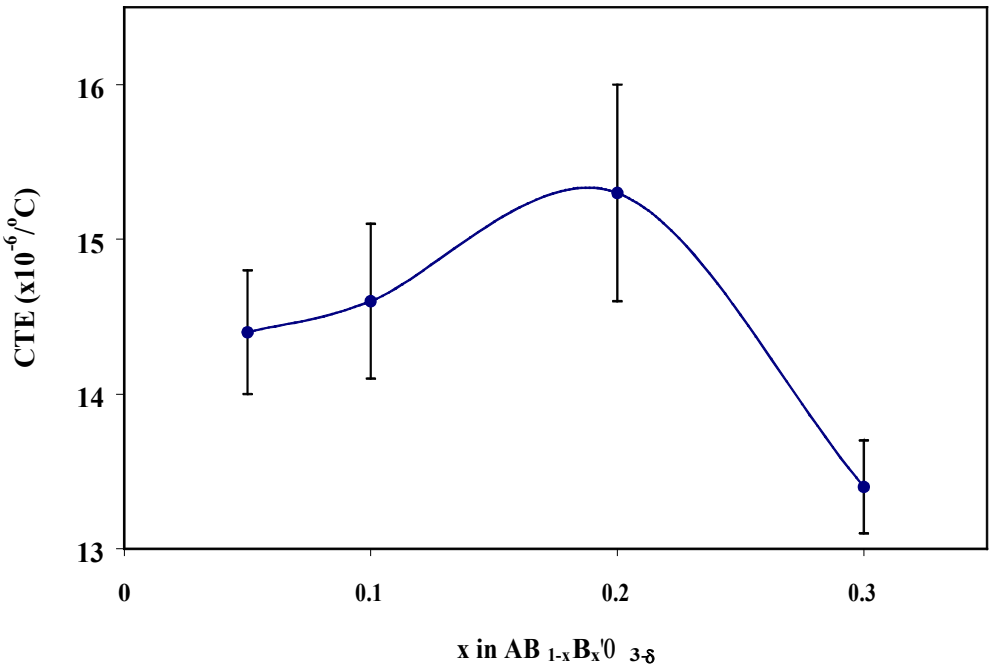

Figure 8. **Plot showing the coefficient of thermal expansion for model perovskite hydrogen transport membranes as a function of dopant level. The values represent averages from one heating cycle and two cooling cycles. The error bars represent ±1σ.**

2. Hydrogen Transport and Conductivity of Single Phase Ceramics

Measurements of membrane proton and electron conductivity proceeded by incorporating disk membranes into an electrochemical cell represented by H_2 (1 atm)/Pt/Ceramic Membrane/Pt/Ar, H_2 (<<1 atm). A diagram of the cell is shown in Figure 9, and a photograph of the apparatus is shown in Figure 10. Pt ink (Heraeus) was used to screen print porous Pt electrodes onto each side of the disks. Pt leads (Alpha Omega) were attached to each surface using Ag epoxy (SPI, Inc.). To seal the disks in the reactor, Pyrex rings were positioned between the disks and tubing, and the assembly heated past the Pyrex softening temperature (> 850°C) under a spring-loaded pressure. The cell temperature was controlled by a furnace, and gases were supplied through needle valve flow meters. Electrochemical measurements were recorded across leads extending from the ends of the reactor using a Hewlett-Packard 34970A Data Acquisition/Switch Unit.

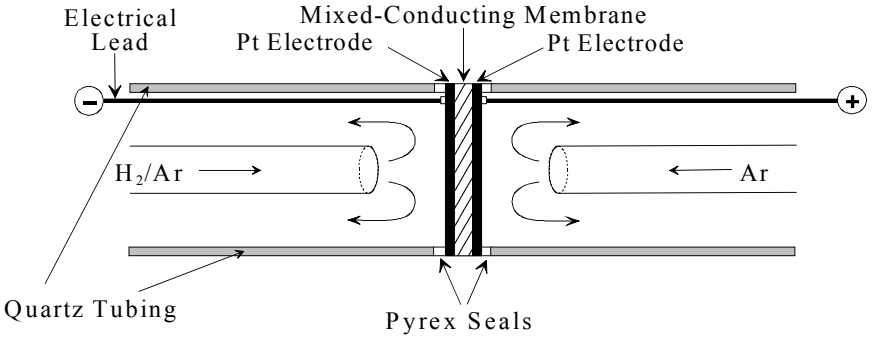

Figure 9. Diagram of the electrochemical cell used for measurement of proton and electron conductivity of membrane materials.

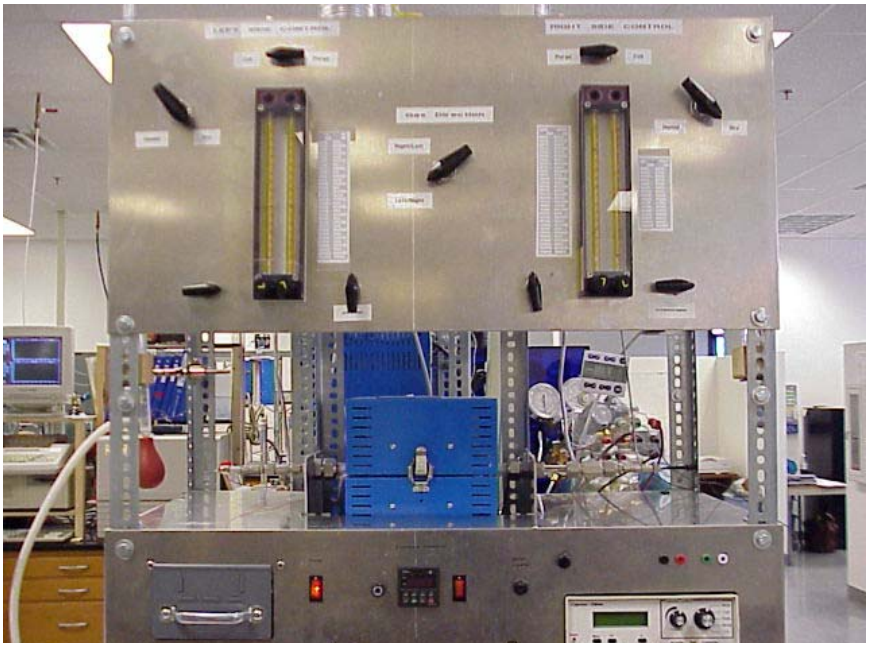

Figure 10. Photograph of the apparatus used for measurement of membrane proton and electron conductivity.

Conductivity measurements were acquired using a H_2 concentration gradient across the membrane. The gradient was established by flowing pure H_2 on one side and only Ar on the other. The H_2 transported to the Ar side was measured using gas chromatography, and the resulting transport potential, E, was calculated from the Nernst equation,

$$E = -\frac{RT}{2F}\ln\frac{\left[H_2^{'}\right]}{\left[H_2\right]} \tag{6}$$

where R is the Gas Constant, T is temperature, F is the Faraday Constant, and $[H_2']/[H_2]$ is the ratio of the dilute to concentrated side. The ionic transfer number was calculated from E and the measured open cell voltage, OCV, according to,

$$t_i = \frac{OCV}{E} \tag{7}$$

The membrane total resistance, R_m, was determined from the slope of cell voltage, V, versus current, I, curves prepared for a range of ten precision resistors included in the circuit. The membrane total conductivity, σ_m, was calculated from,

$$\sigma_m = \frac{d}{AR_m} \tag{8}$$

where d is the membrane thickness and A is the area on one side. Finally, the ionic conductivity, σ_i, was calculated from,

$$\sigma_i = t_i\sigma_m \tag{9}$$

and the electron conductivity, σ_e, was calculated from,

$$\sigma_e = \left(1 - t_i\right)\sigma_m \tag{10}$$

These experiments were repeated over a temperature range of ~600° to 900°C, and the activation energy for proton and electron conduction, E_a, was determined from Arrhenius-type plots according to,

$$\sigma_{i,e} \propto \frac{1}{T}\exp\left(\frac{-E_a}{kT}\right) \tag{11}$$

where T is temperature and k is the Boltzmann Constant.

Hydrogen transport data for material H01 are shown in Figure 11. This data was obtained for a 2.4-mm thick disk membrane in the conductivity apparatus using Pt catalyst screen printed on each side of the disk. At temperatures less than 500°C, a steady transport rate of ~0.4 mL/min/cm^2 was observed and presumed to be from a leak in the seal. Accordingly, this transport rate was subtracted from the data and results in Figure 11 represent corrected values. The transport rate increased from 0.17 to 1.6 mL/min/cm^2 over the temperature range from 638°C to 868°C.

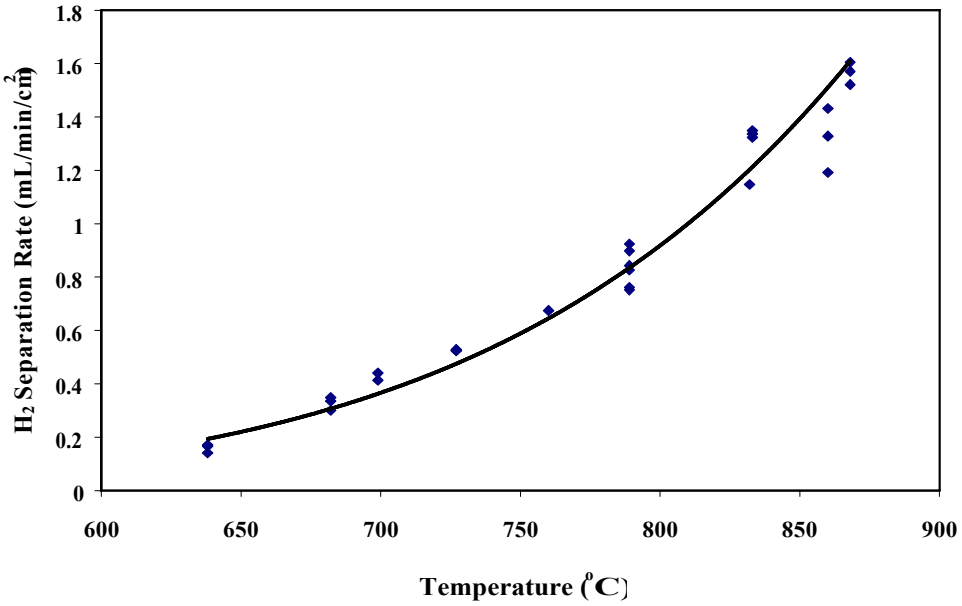

Figure 11. Plot showing hydrogen transport as a function of temperature for membrane material H01.

Conductivity data for this sample is shown in Figure 12. There are significant limitations to this technique and the conductivity values likely are underestimated. However, it is anticipated that this method will enable simple and rapid relative comparisons between samples that will facilitate optimizing compositions. The data in Figure 12 was surprising since the electronic conductivity was higher than the ionic conductivity despite having only 5% doping of a transition metal in the B site. The ionic conductivity appeared to level off at higher temperatures, whereas the electronic conductivity increased sharply. This increase in electronic conductivity at high temperatures likely was responsible for increased transport rates since, in this case, the ambipolar conductivity increased with temperature, *i.e.*, $\sigma_{amb} \rightarrow \sigma_i$ as $\sigma_e \rightarrow \infty$. However, the range of conductivity values obtained from these measurements did not support the observed transport rates. For example, at 638°C a transport rate of 0.17 mL/min/cm^2 corresponded to σ_{amb} = 0.025 S/cm, compared to $\sigma_{amb} = 4 \times 10^{-5}$ S/cm based on conductivity measurements.

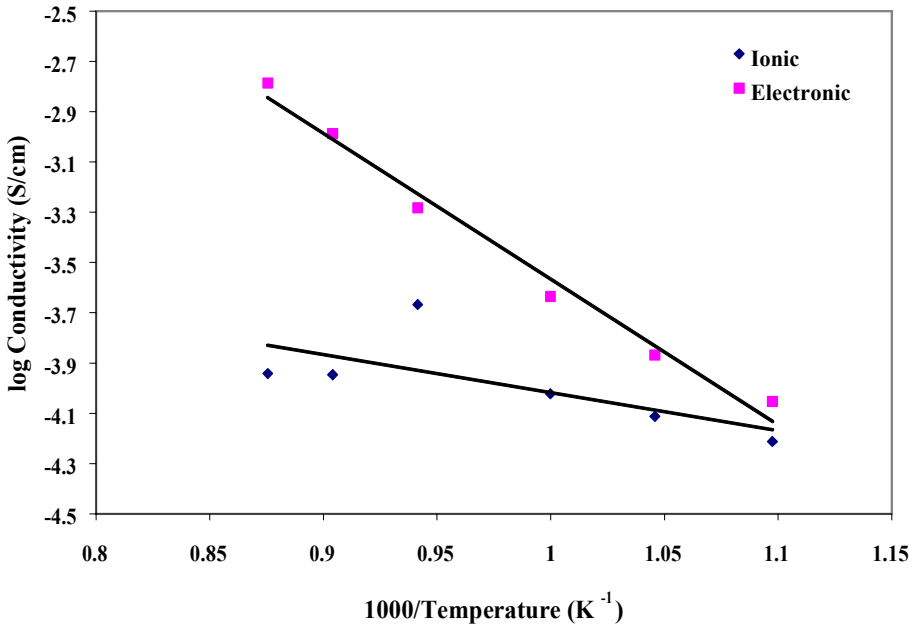

Figure 12. Plot showing ionic (diamonds) and electronic (squares) conductivity as a function of temperature for membrane material H01.

As shown in Figure 13, the transport data for sample H02 was much lower than H01. This sample demonstrated a maximum in transport of only 0.024 mL/min/cm^2 at 700°C. At higher temperatures the transport rate decreased. Conductivity data is shown in Figure 14, and demonstrated overall higher electronic conductivity than H01. This result was not surprising since the transition metal doping at the B site was 30%. Although these transport rates also did not agree with the conductivity values, the agreement was better than for H01. In particular, the ionic conductivity decreased at higher temperature as did the transport rate, although the temperatures for the decrease did not perfectly correlate. Furthermore, the maximum transport of 0.024 mL/min/cm^2 corresponded to σ_{amb} = 1x10^{-3} S/cm, compared to 3x10^{-4} S/cm based on measured conductivity. If the conductivity values are to be trusted, it was surprising that the transport rate for H02 was so low compared to H01 considering that both the ionic and electronic conductivity was higher, and the membrane thickness was only 1.3 mm (relative to 2.4 mm for H01).

Sample H04 had an intermediate B-site doping level of 10% and, as seen in Figure 15, this sample demonstrated the highest transport rate. Hydrogen transport increased from ~0.5 mL/min/cm^2 at 560°C to ~2 mL/min/cm^2 at 740°C. This disk sample was about one half as thick as H01, which might explain the relatively higher transport rate. Acceptable conductivity data was not obtained for this sample. In fact, three samples from different batches generated a wide range of conductivity values. It is not known if the irreproducibility was due differences in batch composition or microstructure, or experimental limitations.

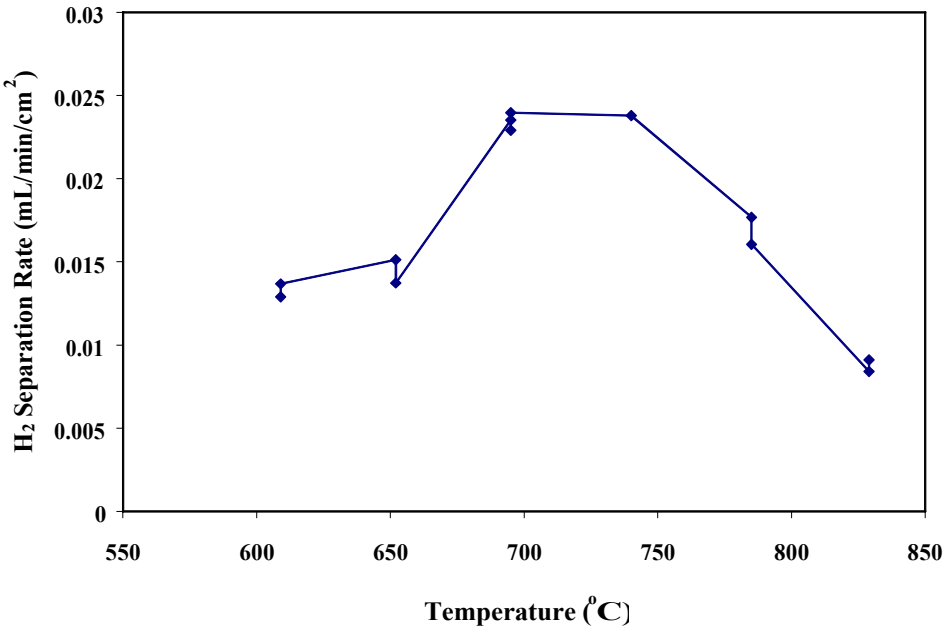

Figure 13. **Plot showing hydrogen transport as a function of temperature for membrane material H02.**

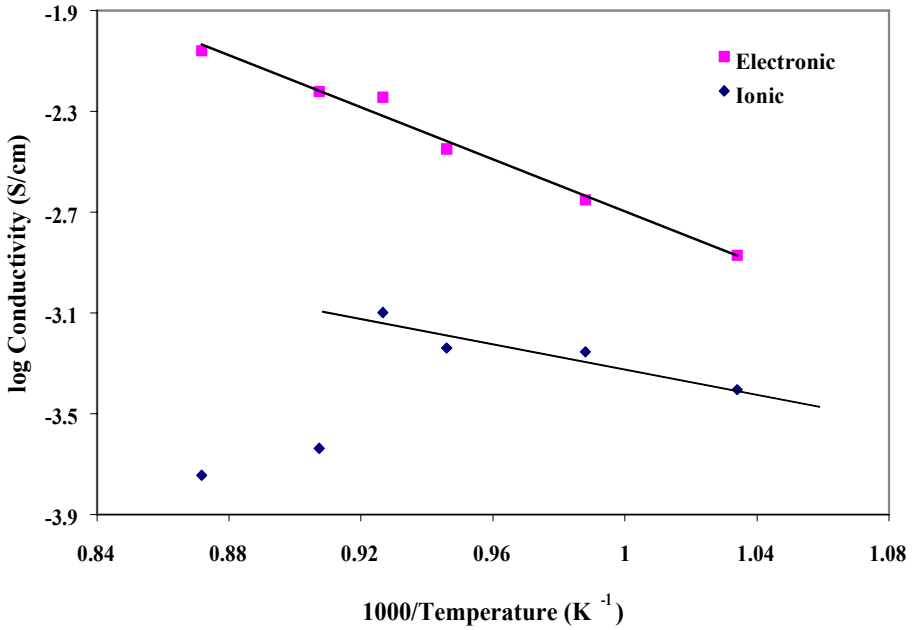

Figure 14. **Plot showing ionic (diamonds) and electronic (squares) conductivity as a function of temperature for membrane material H02.**

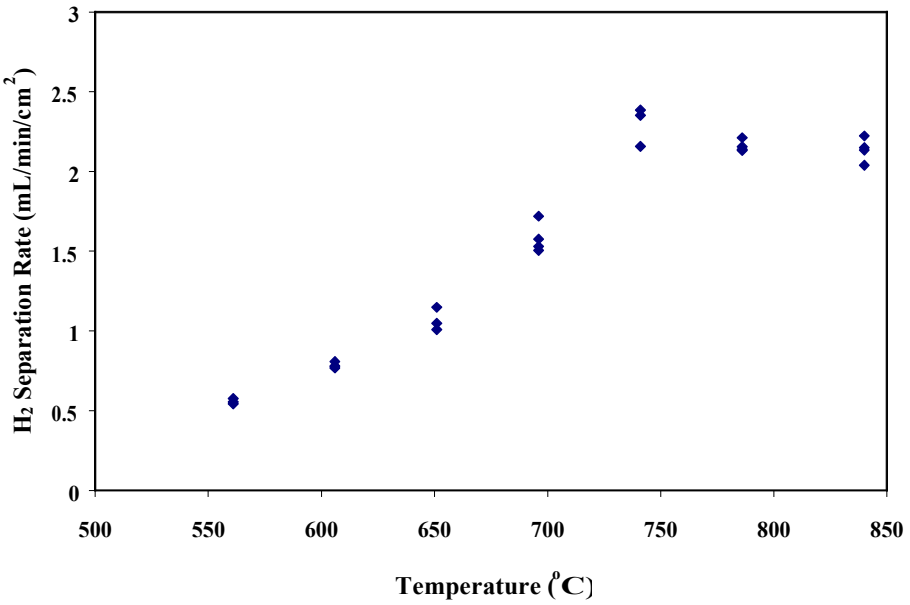

Figure 15. Hydrogen transport as a function of temperature for membrane material H04.

A series of relatively thick tube membranes (~0.9 mm) were tested with the general composition $AB_{1-x}B_x'O_{3-\delta}$, where B′ represents a transition metal. Figure 16 shows hydrogen transport versus temperature for the composition $AB_{0.7}B_{0.3}'O_{3-\delta}$, which demonstrated the best performance of the series. The transport/temperature curves were characterized by an increase in hydrogen flux between ~600° and 850°C, followed by a decrease at temperatures greater than ~900°C. Figure 17 compares the maximum transport rate as a function of transition metal dopant concentration (x in $AB_{1-x}B_x'O_{3-\delta}$) for a series of tube membranes tested under identical conditions. From x = 0.05 to 0.2, there was approximately a four-fold increase in transport. However, increasing x to 0.3 generated approximately a 35-fold increase in transport. X-ray diffraction patterns indicated significant phase differences between these samples. Specifically, at x = 0.05 the material was primarily a single-phase pseudo-cubic perovskite with a lattice parameter of 4.393(1) Å. This value was approximately equal to the undoped ABO_3 analog. At x = 0.1, a second unidentified phase was evident, which became more prominent at x = 0.2. However, at x = 0.3 the unidentified second phase was completely absent and a new phase appeared that was consistent with a rhombohedral perovskite with lattice parameters a = 5.797 Å and c = 28.595 Å. Each composition had essentially the same lattice parameter for the pseudo-cubic perovskite phase (a = 4.39 Å), indicating minimal substitution of the transition metal into the cubic perovskite lattice.

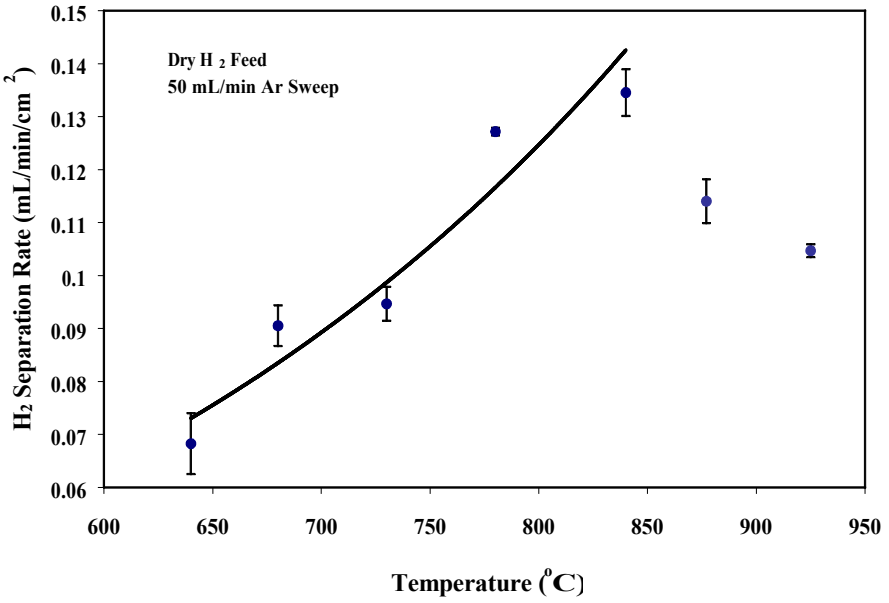

Figure 16. **Plot of hydrogen transport rate versus temperature for a tube membrane with the empirical composition $AB_{0.7}B'_{0.3}O_{3-\delta}$. The membrane was 0.9 mm thick. The flow rate was 50 mL/min for both the hydrogen feed and argon sweep gases. The catalyst was porous platinum.**

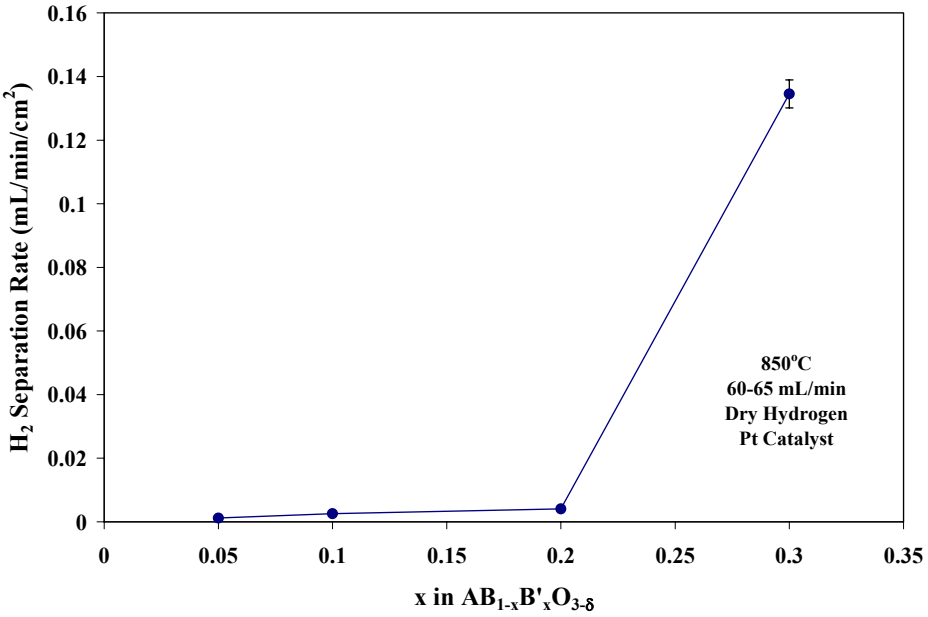

Figure 17. **Relationship between maximum hydrogen transport and dopant concentration for tube membranes with the general formula $AB_{1-x}B'_xO_{3-\delta}$. Each point was taken at 850°C using dry hydrogen as the feed and argon as the sweep gas. The flow rate for both gases was 60-65 mL/min. The catalyst was porous platinum.**

Based on the fact that higher permeation rates were found in perovskite ceramics with increasing doping levels the study was extended to compositions with x = 0.4 and 0.8. The results are presented in Figure 18 as conductivity versus the fraction of B-site transition metal doping. Conductivity is shown rather than H_2 transport to normalize for differences in membrane thickness. As evident in the figure, conductivity was not increased at higher doping levels, and remained at a sharp maximum for x = 0.3. X-ray diffraction patterns indicated that at x = 0.05, the material was primarily a single-phase pseudo-cubic perovskite with a lattice parameter of 4.393(1) Å, which was approximately equal to the undoped ABO_3 analog. At x = 0.1, a second unidentified phase was evident, which became more prominent at x = 0.2. However, at x = 0.3 the unidentified second phase was completely absent and a new phase appeared that was consistent with a rhombohedral perovskite with lattice parameters a = 5.797 Å and c = 28.595 Å. This new phase was even more apparent at x = 0.4 along with the cubic perovskite phase; however, at x = 0.8 the cubic perovskite phase was completely absent.

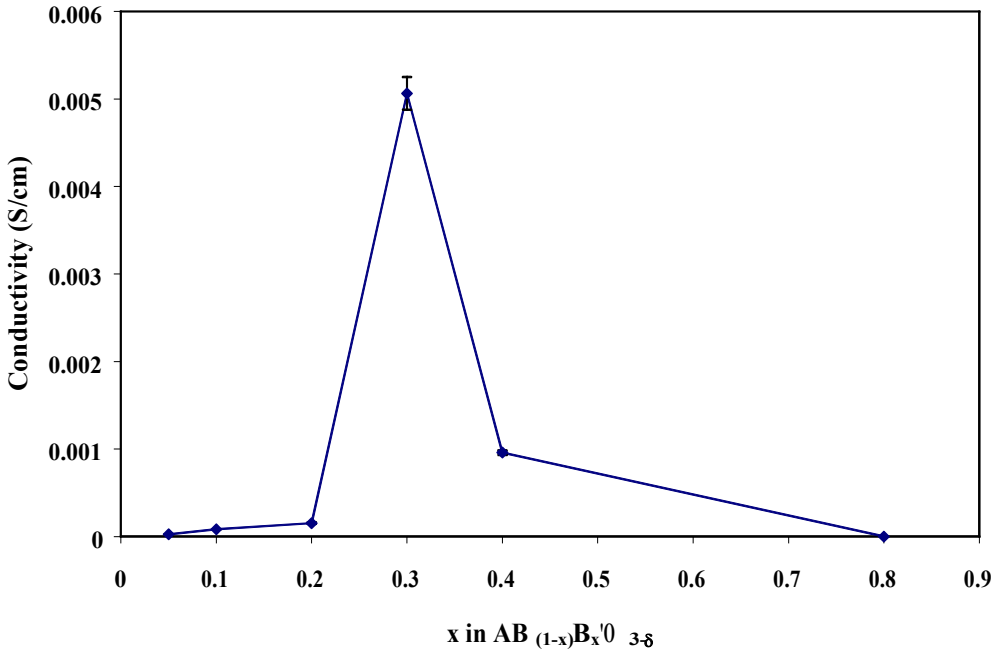

Figure 18. Plot showing ambipolar conductivity as a function of transition metal doping (B′) for ceramic tube membranes with the general composition $AB_{1-x}B'_xO_{3-\delta}$. The analysis temperature was 850°C, and Ni was used as a catalyst. The sweep gas (Ar) flow rate for x = 0.05 through 0.3 was ~65 mL/min, and no humidity was added. However, for X = 0.4 and 0.8, the samples were tested under humid conditions with a sweep rate of 120 mL/min. The error bars represent ±1σ.

Tube membranes prepared from this material (*i.e.*, $AB_{0.2}B'_{0.8}O_{3-\delta}$) had a tendency to crack after only about 1 day under H_2 separation conditions. Coefficient of thermal expansion measurements were performed on a section of the material under air, and a normal expansion curve was observed giving a CTE value of ~6.5 x 10^{-6} K^{-1}. Under 10% H_2 (bal. Ar), a gradual steady expansion was observed between room temperature and 600°C; however, above 600°C a

rapid expansion was observed followed by material failure. Post-mortem X-ray diffraction patterns indicated that the transition metal had been reduced from a 4+ to a 2+ oxidation state. Such material failures were not observed under H_2 separation conditions for the other compositions, however, this data indicates that high levels of this particular transition metal dopant dramatically compromises stability.

Additional ceramic membrane samples with the general composition $AB_{0.8}B'_{0.2}O_{3-\delta}$ were tested with a range of transition metal dopants (B′). Figure 19 shows the ambipolar conductivity of these samples as function of relative atomic number of the transition metal additive. There was a gradual increase in conductivity from 1.1 x 10^{-4} to 3.3 x 10^{-4} S/cm as the transition metal dopant moved three positions from left to right across the periodic table (*i.e.*, *N* to *N+3*). However, at *N+4* the conductivity increased almost 20-fold to 6 x 10^{-3} S/cm. A 1-mm thick membrane of this composition gave a H_2 separation rate of ~0.3 mL/min/cm^2. X-ray diffraction measurements indicated that each sample contained an orthorhombic perovskite phase in addition to a second phase that was dependent on the transition meta dopant. The perovskite phase for each sample had the same lattice parameters, and the data indicated that very little transition metal was incorporated into the perovskite lattice.

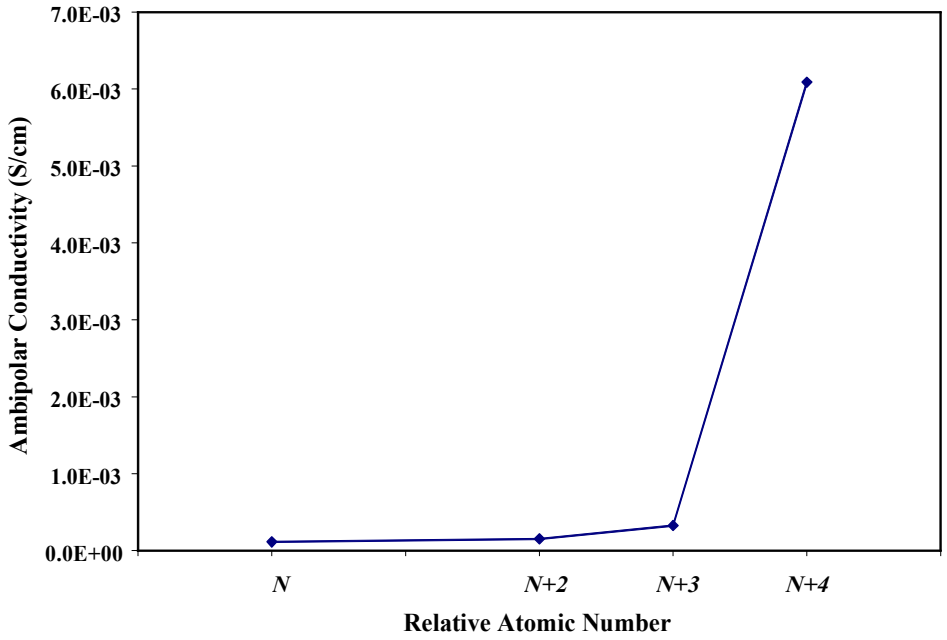

Figure 19. Plot showing ambipolar conductivity as a function of relative atomic number for four transition metal dopants (B′) in the general composition $AB_{0.8}B'_{0.2}O_{3-\delta}$. The inlet gas was humidified 80%H_2 (bal. He), and the sweep gas was Ar. Flow rates were 120 mL/min, and the temperature was 850°C. Data was taken for tube membranes, except for (N+4) which was a disk. Ni was used as a catalyst.

In an effort to identify the most appropriate experimental conditions for evaluating dense ceramic hydrogen transport membranes, hydrogen flux was measured as function of gas flow rate and moisture content. Figure 20 demonstrates that as the gas flow rate (on both sides of the membrane) was increased from 30 to 120 mL/min, there was a steady increase in hydrogen separation rate at each temperature tested. Since presumably increasing the sweep rate decreases hydrogen partial pressure, it is reasonable to expect a corresponding increase in potential and hydrogen flux. This presumption was supported by the 850°C data in Figure 21 A and B. However, at 800°C there was no significant difference in hydrogen concentration or potential between 65 and 120 mL/min, and at 750°C the hydrogen concentration actually increased slightly at 120 mL/min. When this data was used to calculate ambipolar conductivity (σ_{amb}), an apparent increase in conductivity with increasing flow rate was observed at each temperature, as shown in Figure 22. This dependence of apparent σ_{amb} on flow rate is typical, and underscores and experimental limitation when using bulk hydrogen partial pressure to represent the actual interfacial hydrogen partial pressure. It is possible that at lower flow rates there is a significant hydrogen partial pressure gradient between the membrane/gas phase interface and the bulk. Under these conditions, the apparent σ_{amb} calculated from the bulk hydrogen partial pressure will be lower than the actual σ_{amb}. As the sweep flow rate is increased and more permeate hydrogen is removed from the surface, the difference between hydrogen partial pressure in the bulk and interface likely is reduced, and the apparent σ_{amb} is closer to the actual value. Since the bulk hydrogen partial pressure values are not necessarily representative of the membrane interface, it is not unreasonable that hydrogen transport increased with sweep flow rate at 800° and 750°C although the calculated potentials did not show the expected trend.

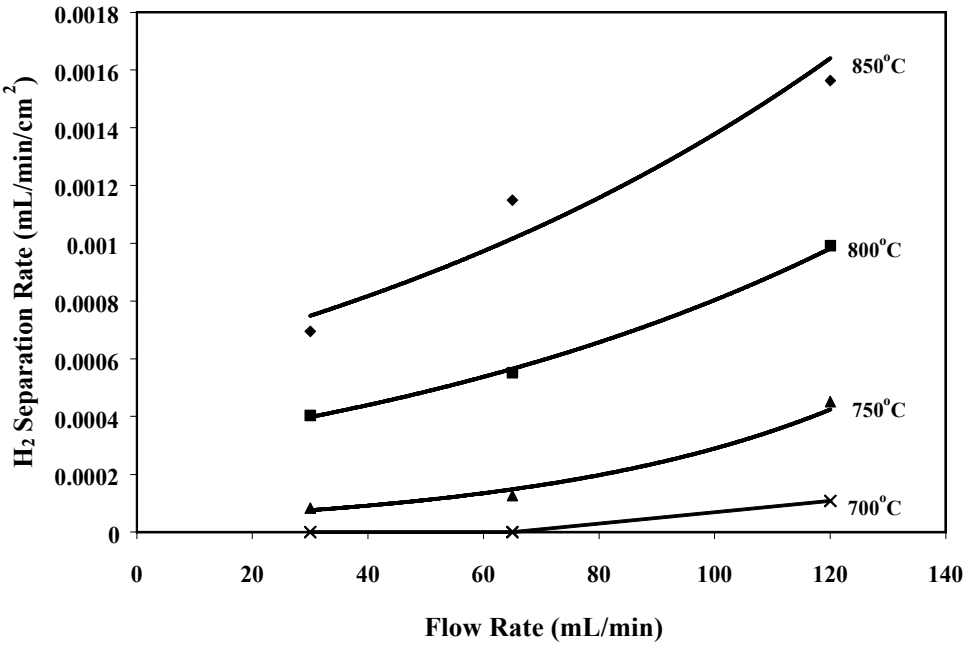

Figure 20. Plot showing the dependence of gas flow rate on hydrogen separation rate for several temperatures. Gases on both sides of the membrane were adjusted simultaneously to the values indicated.

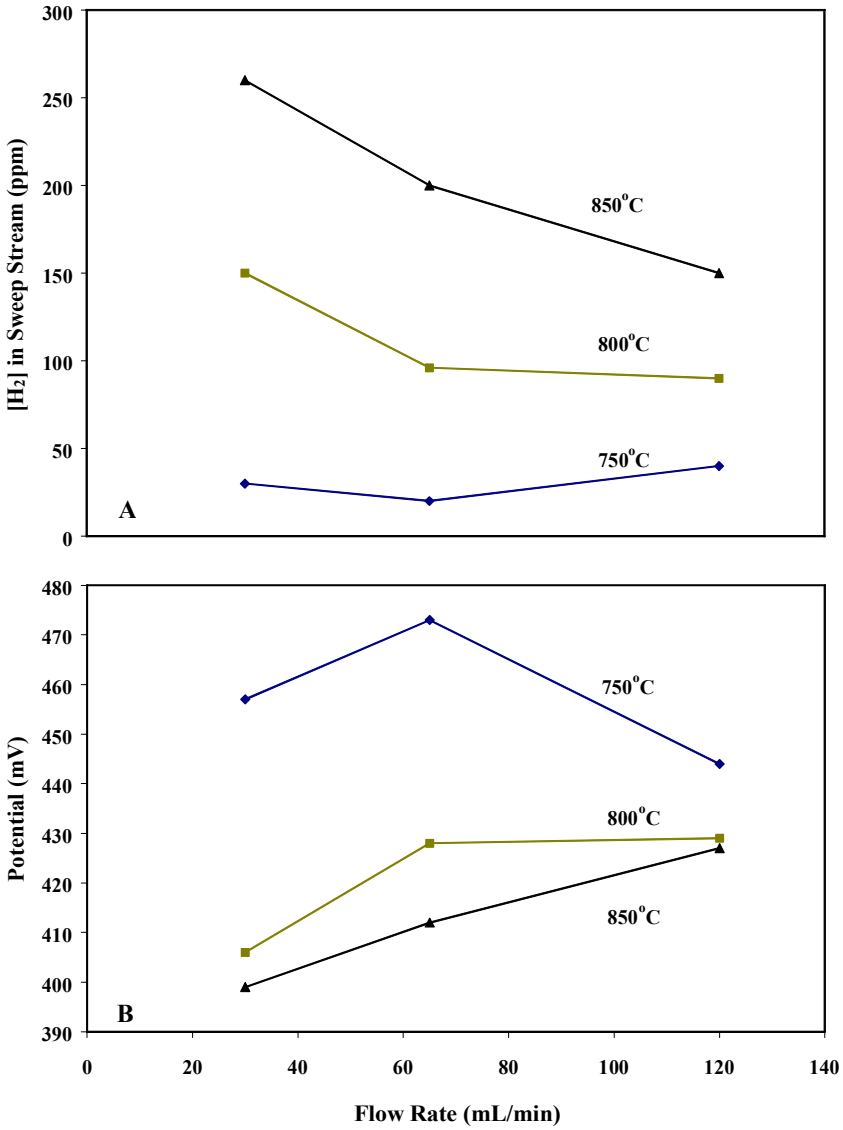

Figure 21. **Plot (A) shows the concentration of hydrogen in the argon sweep stream as a function of sweep flow rate for several temperatures. The corresponding potentials across the membrane as calculated from the Nernst equation are shown in (B).**

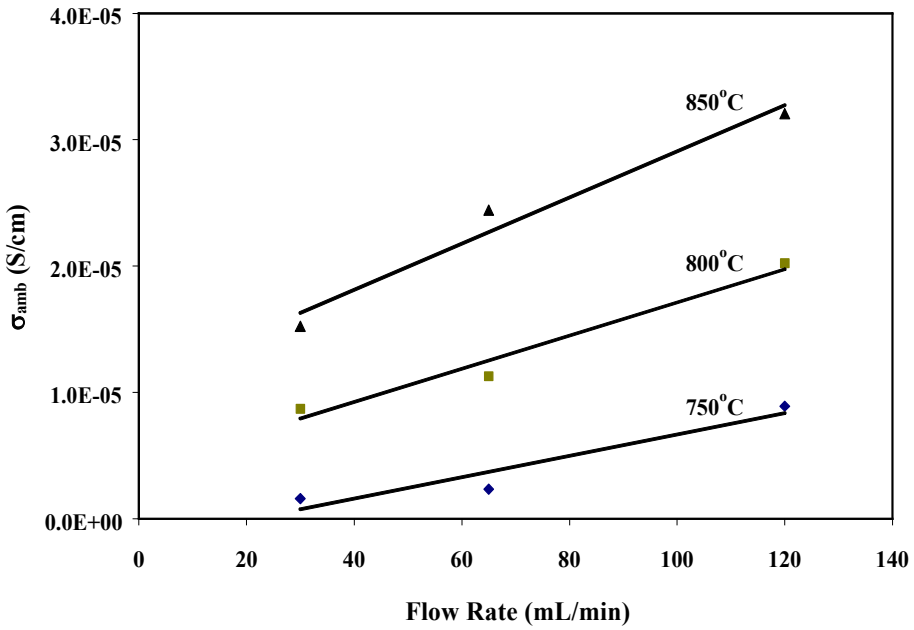

Figure 22. Plot showing the effect of sweep gas flow rate on calculated conductivity based on cell temperature and partial pressure of hydrogen in the exit stream.

Figure 23 shows a comparison of hydrogen transport rates using dry and humidified hydrogen. Humidified hydrogen (~2 to 5%) was prepared by bubbling the gas stream through water at room temperature prior to entering the separation cell. Approximately 5 hours were required after introducing humidity to achieve stable transport rates. Higher transport rates were observed with the humidified stream, and the improvement increased with temperature. However, the difference between the humid and dry stream was very small. Similar results were obtained for other membrane compositions. The improved separation rates in the presence of moisture presumably is due to preferential uptake of hydrogen through reaction of water with oxygen vacancies, relative to dry hydrogen.

New proton conducting materials with improved properties were investigated by ANL. Cerate-based perovskites exhibit high proton conductivity in hydrogen-containing atmospheres at elevated temperatures,[2] however, they easily decompose in the presence of CO_2 at low temperatures (below 800°C) and hence lose their proton conduction.[3] Lack of good mechanical properties is another factor that hinders the application of cerate-based materials. To develop a more rugged alternative to the cerates, Eltron and ANL investigated acceptor-doped titanates because they may have better mechanical strength and better stability in CO_2-containing atmosphere. While these compounds do not possess high proton conductivity because of their very low proton concentrations, the diffusivity of protons in these compounds is extremely high.[4] Therefore, although these materials may not yield high hydrogen fluxes, the results from this study may give useful information to engineer new formulations with both high hydrogen flux and good stability.

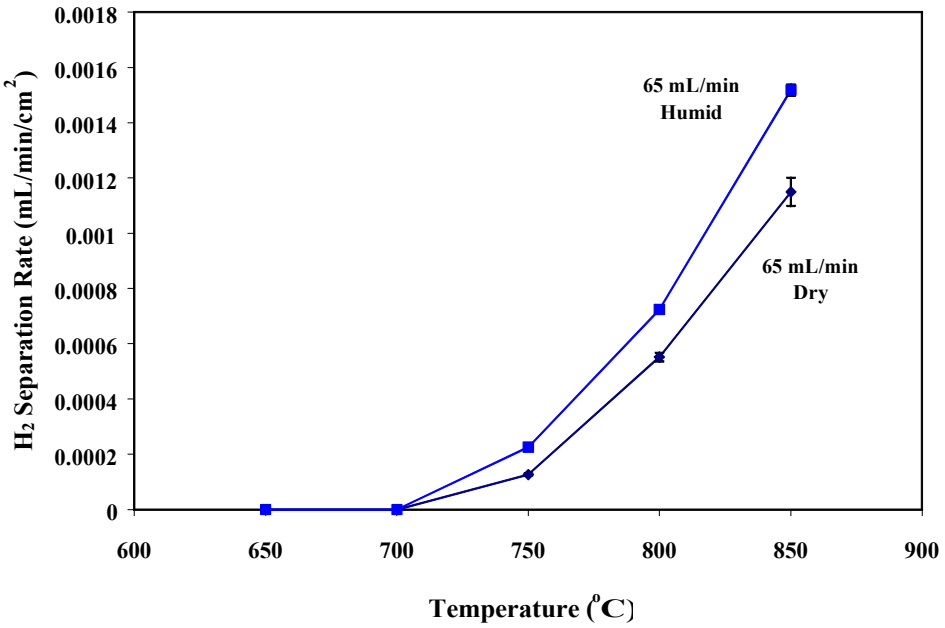

Figure 23. Plot comparing hydrogen transport rates in dry and humid hydrogen. Humidified gas was prepared by bubbling hydrogen through water at room temperature prior to entering the separation cell. The flow rate of hydrogen and sweep gas was 65 mL/min. The error bars represent ±1σ.

Titanate ceramics were synthesized using two different dopants over a wide concentration range, and XRD analysis indicated that these materials were single phase. Total conductivity was measured under a variety of atmospheres using a four-point DC method. The range of total conductivity measured for these samples was between 10^{-3} and 10^{-1} S/cm. The samples with the higher presumed proton conductivity showed poor stability under reducing conditions, and crumbled after prolonged exposure to a H_2/N_2 atmosphere. The second category of materials appeared stable under reducing conditions and had a maximum total conductivity of ~5 x 10^{-2} S/cm. However, based on the conductivity dependence on atmosphere, it is likely that these materials had low proton conductivity and therefore were not investigated further.

B. Ceramic / Ceramic Membranes (Eltron, CoorsTek)

Ceramic/ceramic composites were developed as possible alternatives to cermets. In these composites a one ceramic phase is a perovskite proton conductor and the second ceramic phase is an electron conducting transition metal oxide. In addition to improved permeation it was thought that these composites might have greater mechanical stability due to similar characteristics between the two phases, and might have greater chemical stability in the presence of sulfur. A preliminary composition represented as $AB_{0.8}B^c_{0.2}O_{3-\delta}$ / CER1 was prepared by mixing the appropriate powders and sintering at 1375-1390°C. Compositions with 60 wt.% $AB_{0.8}B^c_{0.2}O_{3-\delta}$ and 40 wt.% CER1 were extremely brittle and fractured during preparation for hydrogen transport measurements. However, adjusting the proportions to 75 wt.% $AB_{0.8}B^c_{0.2}O_{3-\delta}$ and 25 wt.% CER1 resulted in a much stronger membrane. A 0.94-mm thick membrane with this composition achieved a hydrogen separation rate of only 0.006 $mL \cdot min^{-1} \cdot cm^{-2}$, which

corresponded to an ambipolar conductivity of 1.7 x 10^{-4} S/cm. The relatively poor performance likely was due to cross diffusion of constituents from each phase, which compromised proton conductivity. This assumption was supported by XRD patterns. A similarly prepared membrane of the same composition was ground down to 0.21 mm and results for this sample are presented in Figure 24. Both samples showed a maximum permeation at 850°C; however the thinner membrane demonstrate more than a three fold increase in performance. The highest permeation was 0.027 mL•min^{-1}•cm^{-2}, which correlated to a conductivity of 1.69 x 10^{-4} S/cm — exactly the same as the thicker sample.

A second ceramic / ceramic composite was fabricated with the formula $AB_{0.8}B^{c}_{0.2}O_{3-\delta}$/CER2. As with $AB_{0.8}B^{c}_{0.2}O_{3-\delta}$/CER1, the challenge in fabricating this category of membranes is to achieve a dense membrane without migration of constituents between the two phases. For this composition, the main problem is migration of the perovskite B-site cation into the CER1 phase. Such migration of cations can compromise both the proton and electron conductivity of the material, and dramatically reduce H_2 permeation. Numerous batches of both $AB_{0.8}B^{c}_{0.2}O_{3-\delta}$/CER1 and $AB_{0.8}B^{c}_{0.2}O_{3-\delta}$/CER2 were prepared with varying quantities of each phase and with an excess of the B^c dopant in an effort to minimize migration; however, none of these approaches were successful.

Figure 25 shows H_2 permeation and ambipolar conductivity as a function of temperature for a 1-mm thick $AB_{0.8}B^{c}_{0.2}O_{3-\delta}$/CER2 membrane. A maximum permeation of about 0.025 mL·min^{-1}·cm^{-2} was obtained, corresponding to an ambipolar conductivity less than 10^{-3} S/cm.

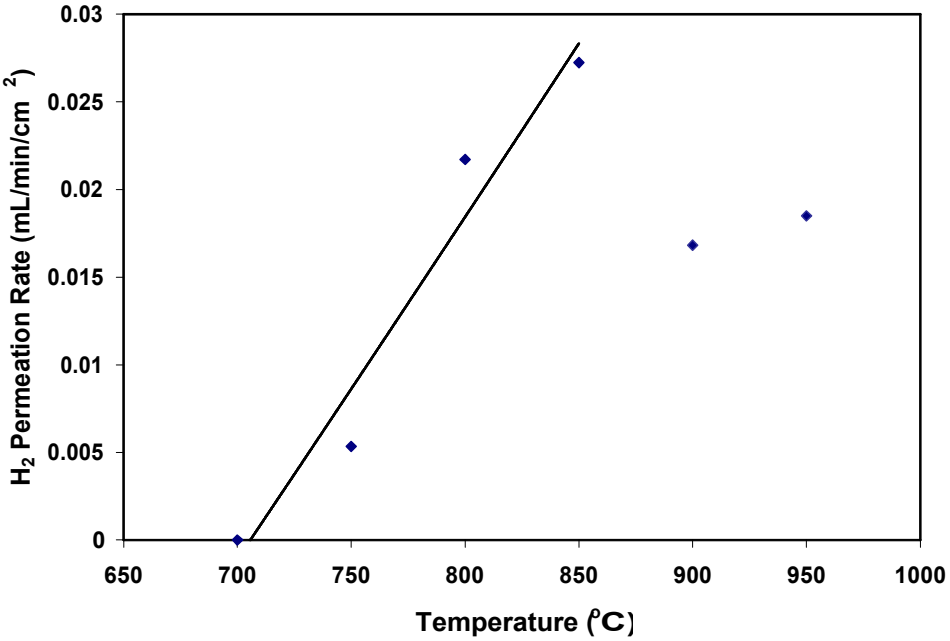

Figure 24. Hydrogen permeation as a function of temperature for a ceramic / ceramic composite membrane. The feed stream was humidified 80 vol.% H_2 (bal. He) and the sweep gas was Ar.

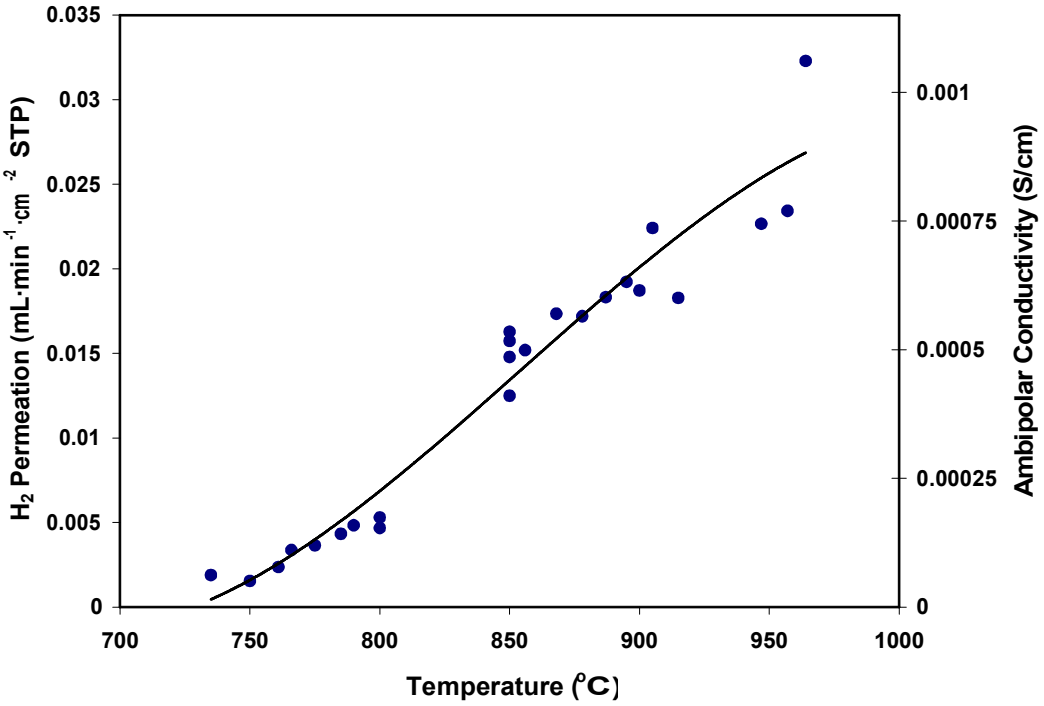

Figure 25. H_2 permeation and ambipolar conductivity as a function of temperature for a 1-mm thick ceramic / ceramic composite membrane ($AB_{0.8}B^c_{0.2}O_{3-\delta}$ / CER2). The feed gas was approximately 80 mL/min of 80 vol.%H_2 (bal. He) and the sweep gas was 150 mL/min Ar.

Two-phase ceramic / ceramic composites had low hydrogen permeability, likely due to interdiffusion of constituents between phases. In this respect, two-phase ceramic / ceramic composites had no advantage over single phase hydrogen separation ceramics. However, as discussed below, ceramic / ceramic composites posses mechanical and corrosion resistance benefits compared to single phase ceramics and cermets.

C. High Temperature Cermets (Eltron, CoorsTek, ANL)

Ceramic metal (cermet) membranes were prepared in an effort to further increase the electronic conductivity across a hydrogen separation membrane. It was expected that a higher electronic conductivity through a metal phase rather than a ceramic phase would result in higher proton conductivity through the perovskite ceramic phase. Metals such as nickel are somewhat permeable to hydrogen, but the hydrogen conducted through the metal is negligible compared to the proton conduction of the perovskite. Therefore these membranes are considered cermets containing a no-permeable metal phase. Cermets containing permeable metals are discussed in the next section.

Dense cermet membranes were prepared using a doped perovskite with the general composition $AB_{1-x}B_x'O_{3-\delta}$ as the ceramic phase. Numerous samples were prepared with varying ceramic/metal ratios and particle sizes. Large ceramic particles (0.4 - 1.5 μm) were prepared using solid-state synthesis without attrition, and small ceramic particles (40 nm) were prepared

using coprecipitation. Large metal particles (3-7 μm) were purchased commercially either as the reduced metal or metal oxide. Small metal particles (50 nm) were achieved by precipitating the metal onto the ceramic powder from a metal nitrate precursor solution. The powders were mixed by ball milling for 1 hour, then pressed into pellets at 15 kpsi for 2 minutes. The pellets were sintered at 1425°C for 4 hrs under 10% H_2 (bal. Ar), then sanded to the desired thickness and polished. Disk membranes prepared with 38, 41, 44, and 47 wt.% metal (29,33,36, and 38 vol.%) all showed continuous metal phases in the electron micrographs. Figure 26 shows an SEM image of the 44 wt.% metal sample. Continuity of the metal phase was confirmed by testing electrical continuity using a voltmeter. SEM results also showed that smaller particle sizes led to smaller grain sizes in the densified membrane; however, there was no apparent difference in phase continuity using smaller particles relative to larger particles.

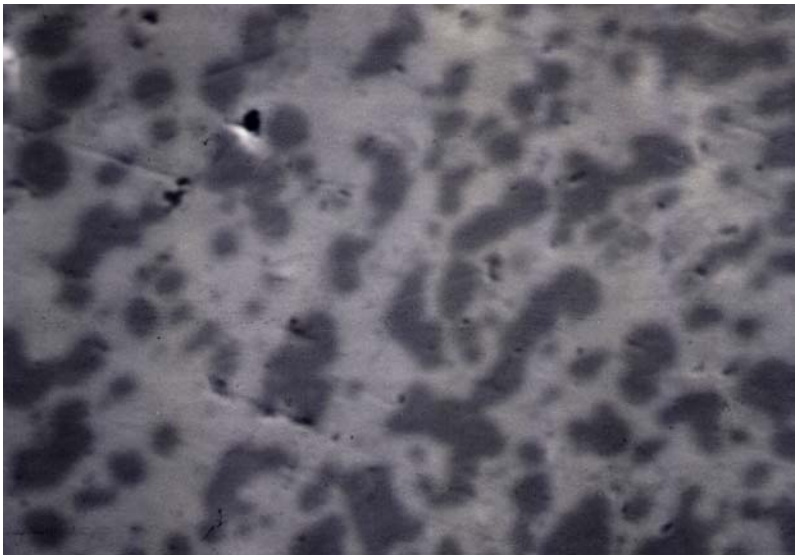

Figure 26. SEM image of a 56/44 wt.% ceramic/metal membrane. The dark regions are the metal phase and the light regions are the proton conducting ceramic.

Figure 27 demonstrates the improvement in hydrogen flux upon compositing a mixed-conducting ceramic with a metal. The top curve is hydrogen flux across a 2.3-mm thick cermet membrane with 47 wt.% metal component and 53 wt.% mixed proton/electron conducting ceramic component. The bottom curve corresponds to a 1-mm thick membrane of the ceramic material only. The maximum hydrogen transport for the cermet membrane was one order of magnitude higher than the ceramic membrane. Similar improvement in hydrogen flux for cermet materials have recently been published by Balachandran *et al.*[5] Furthermore, it is significant that the cermet was more than twice as thick as the ceramic membrane. Using these hydrogen transport rates and membrane thicknesses, the apparent σ_{amb} for the cermet and ceramic was ~10^{-3} S/cm and ~10^{-4} S/cm, respectively. Since the cermet was not limited by electron conductivity, $\sigma_{amb} \approx \sigma_{H+}$, which was consistent with ionic conductivity measurements obtained on the ceramic.

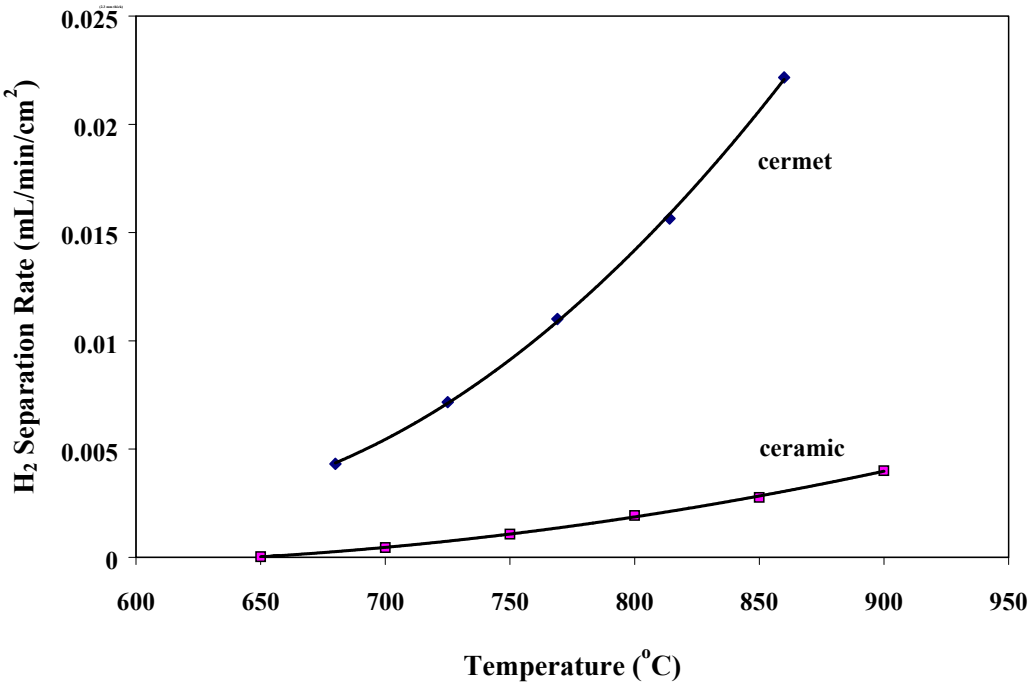

Figure 27. Plot showing the improvement in hydrogen flux upon compositing metal with a hydrogen-permeable ceramic. The cermet membrane (2.3 mm thick) was 47 wt.% metal, and the ceramic component was the exact same composition as the ceramic membrane (1 mm thick).

Figures 28 and 29 show the H_2 transport rates and conductivity of these samples as a function of the metal phase content (under humid conditions). Since a range of membrane thicknesses between 0.75 and 2 mm were used for these tests, the conductivity data in Figure 29 provides a better comparison of the materials. However, both plots show a maximum for the 44-wt.% (36-vol.%) sample. A 1.2-mm thick membrane of this composition generated a H_2 transport rate of 0.075 ± 0.004 mL/min/cm^2, and a conductivity of 0.003 S/cm at 900°C. Conductivity and transport did not change much between 800 and 950°C for this sample, which indicated a plateau in the temperature dependence. These results represent approximately a four-fold improvement over the data in the previous report, and are essentially equivalent to those obtained by Balachandran *et al.* for similar compositions.[5]

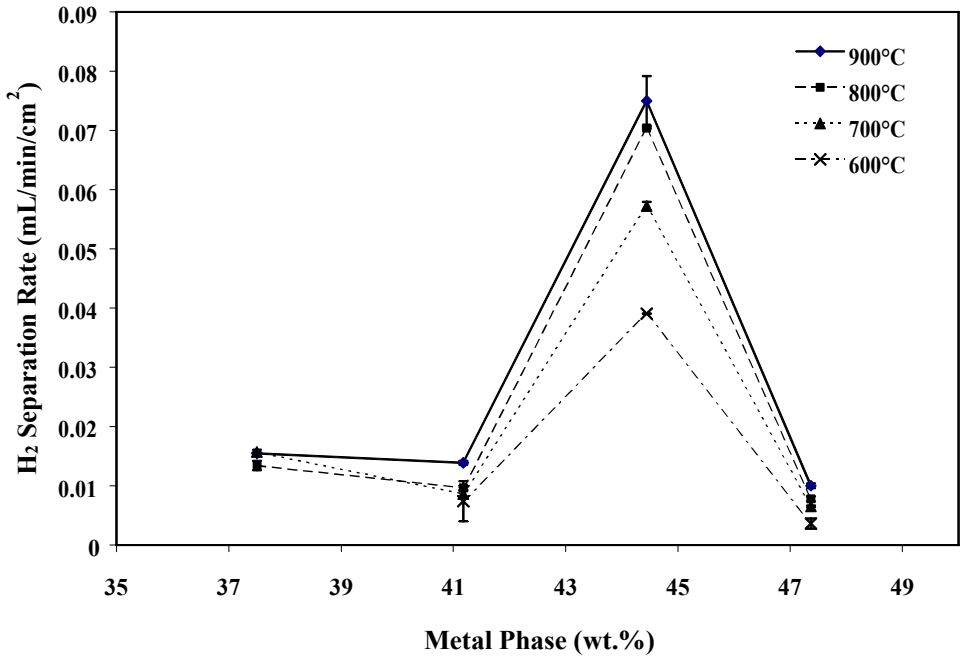

Figure 28. **Plot showing H_2 separation rate as a function of metal phase wt.% at temperatures between 600 to 900°C. The feed gas was ~ 80% H_2 (bal.He), and was bubbled through water prior to entering the cell. The sweep gas was Ar. Flow rates were maintained at ~100 mL/min. Membrane thickness varied between 0.75 and 2.0 mm, thus conductivities (Figure 29) provide a more useful comparison between samples.**

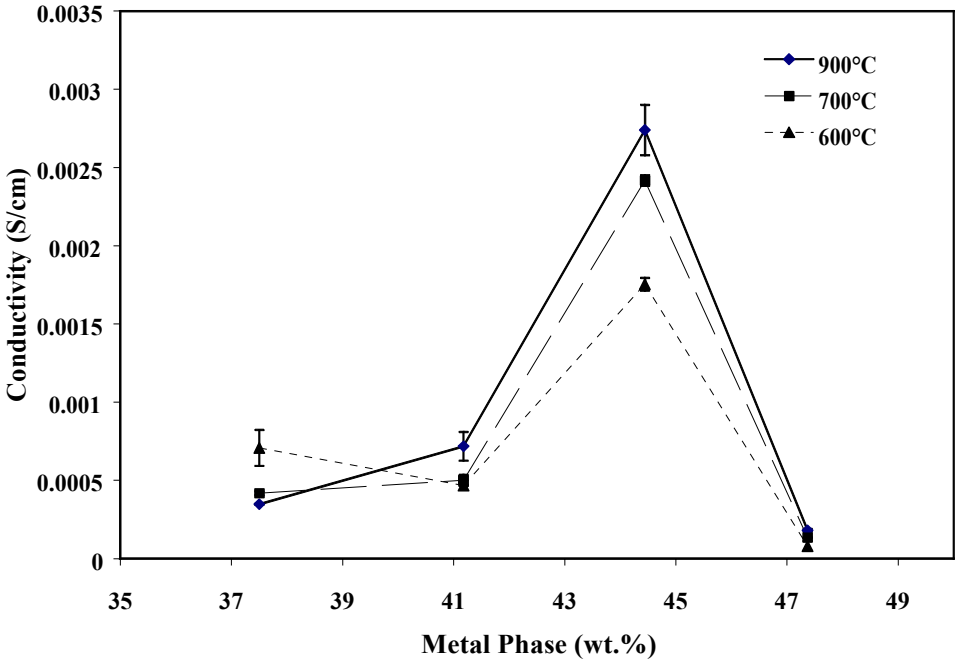

Figure 29. **Plot showing conductivity as a function of metal phase wt.% at temperatures between 600 and 900°C. Testing conditions were presented in Figure 28.**

Figure 30 shows the temperature dependence of the conductivity for the 44-wt.% metal phase cermet over the range of 600° to 950°C. There was a break in the data at ~800°C, which also was observed by Balachandran *et al.*, although at a lower temperature (700°C). The break in data was attributed to crystallographic changes at high temperatures that affect proton migration and/or proton concentration in the ceramic. Based on these results, the activation energy was calculated to be only 0.2 eV. Furthermore, although the other samples demonstrated much lower conductivity, activation energies also were between 0.2 and 0.3 eV. However, the pre-exponential factor was nearly ten-fold higher for the 44-wt.% metal phase sample.

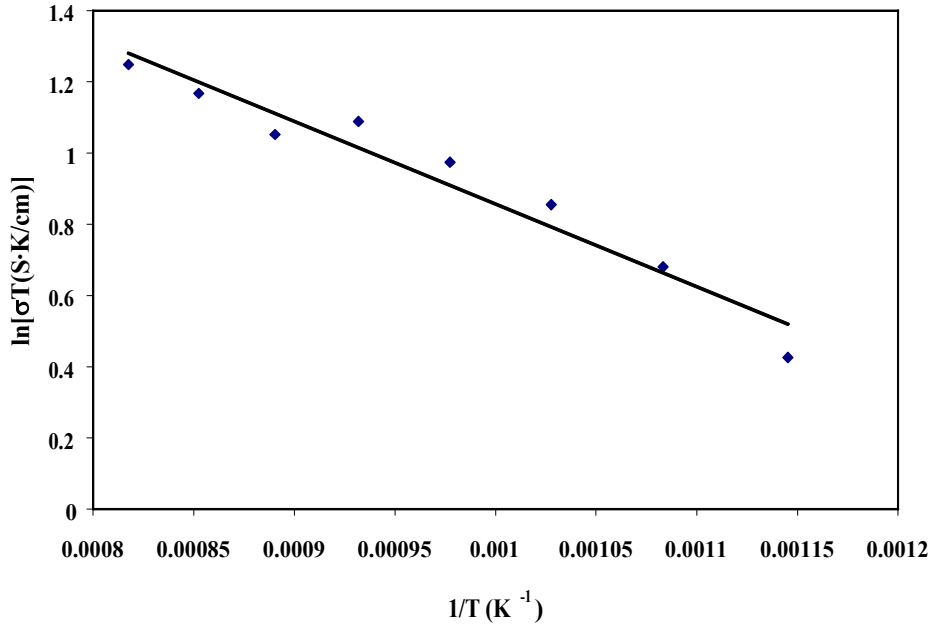

Figure 30. Plot showing temperature dependence of conductivity for the 44-wt.% metal phase cermet sample. Testing conditions were presented in Figure 28.

As discussed above, previous results showed that for perovskite-based ceramics ambipolar conductivity and corresponding H_2 transport of the ceramic phase could be increased by doping with selected transition metals. Moreover, there appeared to be a trend of increasing conductivity when moving from left to right across the periodic table within a row of transition metal dopants. Based on those results, several cermet compositions were prepared and tested using three different transition-metal-doped ceramic phases, designated as $AB_{0.9}B^{a}_{0.1}O_{3-\delta}$, $AB_{0.8}B^{b}_{0.2}O_{3-\delta}$, and $AB_{0.8}B^{c}_{0.2}O_{3-\delta}$, each combined with the same metal phase. Ceramic phases $AB_{0.9}B^{a}_{0.1}O_{3-\delta}$ and $AB_{0.8}B^{b}_{0.2}O_{3-\delta}$ were mixed proton and electron conductors, whereas ceramic phase $AB_{0.8}B^{c}_{0.2}O_{3-\delta}$ primarily was a proton conductor. The cermets were prepared with varying ceramic/metal ratios from powders with particle sizes between 0.4 and 1.5 μm. The powders were mixed by ball milling for one hour, then pressed into pellets at 15 to 17 kpsi for two minutes. The pellets were sintered between 1100° and 1425°C for 4 hours under 5% H_2 (bal. Ar), then sanded to the desired thickness and polished. The metal phase of these cermets is not a hydrogen transport material, however, it does have catalytic activity for dissociation of hydrogen. Thus, no catalyst was applied to the cermet samples for these studies.

The thicknesses of the membranes tested were between 0.5 and 1.2 mm, which enabled hydrogen transport rates between ~0.01 and 0.3 mL/min/cm^2. However, since membranes of a range of thicknesses were used for testing, and inevitably the hydrogen concentration on opposite sides of the membranes varied, the data below is presented in terms of conductivity to normalize for these variables. Figure 31 shows a plot of ambipolar conductivity as a function of the metal phase weight percent for each of the ceramic phases tested. Ohmmeter measurements across the thickness of the membrane samples indicated a resistance between 0.1 to 0.3Ω. Considering the very small contact area between the membrane surface and ohmmeter probes, this resistance range corresponded to very high electron conductivity, and indicated that the metal phase content was within the percolation range for each metal volume tested. Similar conclusion were derived from studies of $BaCe_{0.8}Y_2O_3$/Ni and $Bi_{1.5}Er_{0.5}O_3$/Ag cermets.[6,7] Therefore, the difference in ambipolar conductivity between the three curves in Figure 31 was the result of differences in the proton conductivity of the ceramic phases. The maximum conductivity for each curve was observed at a metal content of 44.4 wt.%, which corresponded to between 34 and 36 vol.% metal phase, and approximately 80 mol% metal phase. Since there was adequate metal phase for electrical continuity in each sample tested, the maximum in the curves at 44.4 wt.% likely was not the result of an optimum bulk electron conductivity. Instead, it is probable that the higher percentage of metal phase resulted in improved hydrogen exchange catalysis at the membrane surface, as also was observed by Siriwardane *et al.*[6] Specifically, as the bulk metal concentration increases, the membrane surface roughness increases due to formation metal nodules that facilitate dissociative adsorption of hydrogen on the feed side, and desorption of hydrogen on the permeate side. However, at the highest metal phase wt.% tested, the ambipolar conductivity fell sharply. There are two possible explanations for this result. First, when the quantity of metal at the surface is very high, metal annealing at elevated temperatures actually can smoothen surface features and reduce surface area, which can reduce catalytic activity. Second, at the highest metal phase content, continuity of the proton conducting phase could be lost.

The results in Figure 31 indicated that the ceramic phase $AB_{0.9}B^a_{0.1}O_{3-\delta}$ had significantly higher proton conductivity than the other two phases tested. However, as shown in the lower two curves of Figure 32, the *ambipolar* conductivity of $AB_{0.9}B^a_{0.1}O_{3-\delta}$ was actually lower than for $AB_{0.8}B^b_{0.2}O_{3-\delta}$ over the entire temperature range tested. Thus, it is likely that the higher ambipolar conductivity of $AB_{0.8}B^b_{0.2}O_{3-\delta}$ was the result of higher electron conductivity. Based on this explanation, it was reasonable that the $AB_{0.8}B^b_{0.2}O_{3-\delta}$/metal cermet demonstrated only slightly higher ambipolar conductivity than the corresponding ceramic phase alone. However, a very significant increase in ambipolar conductivity was observed for the $AB_{0.9}B^a_{0.1}O_{3-\delta}$/metal cermet (top curve) because of higher proton conductivity in $AB_{0.9}B^a_{0.1}O_{3-\delta}$.

The data in Figure 33 demonstrates that a similar improvement in ambipolar conductivity can be achieved by increasing the quantity of transition metal dopant, rather than adding a metal second phase. Specifically, ambipolar conductivity increased almost by a factor of 40 when the dopant B^a was increased from a fraction of 0.1 to 0.3. SEM images and energy dispersive X-ray (EDX) measurements of $AB_{0.7}B^a_{0.3}O_{3-\delta}$ demonstrated a distinct elongated rod-like phase consisting primarily of the B^a dopant embedded in a matrix containing mainly the A and B cations. XRD patterns of $AB_{0.9}B^a_{0.1}O_{3-\delta}$ indicated a primary pseudo-cubic ABO_3 phase, with a second pseudo-cubic phase consistent with AB^aO_3. As shown in the middle curve of Figure 33, adding a metal phase to this two-phase ceramic actually decreased conductivity. This result likely was due to a dilution of the proton conducting by an excessive quantity of electron conducting phase(s).

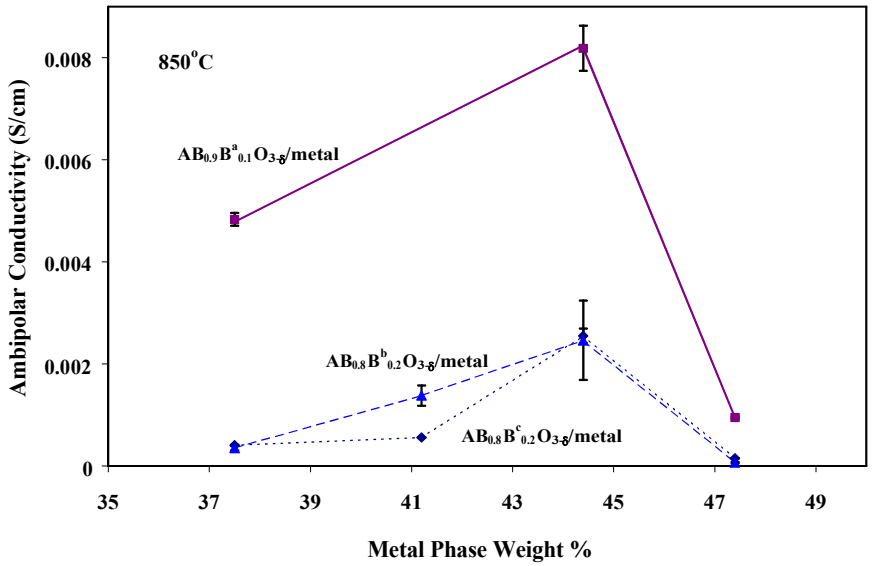

Figure 31. **Plot comparing ambipolar conductivity of three cermet compositions as a function of metal phase weight percent. The ceramic phases designated as $AB_{0.9}B^{a}_{0.1}O_{3-\delta}$ and $AB_{0.8}B^{b}_{0.2}O_{3-\delta}$ were mixed proton and electron conductors, whereas, the ceramic phase $AB_{0.8}B^{c}_{0.2}O_{3-\delta}$ was primarily a proton conductor. The concentration of hydrogen on the feed side was 80 vol.% (bal. He), and Ar was used on the permeate side. The flow rates were 120 mL/min.**

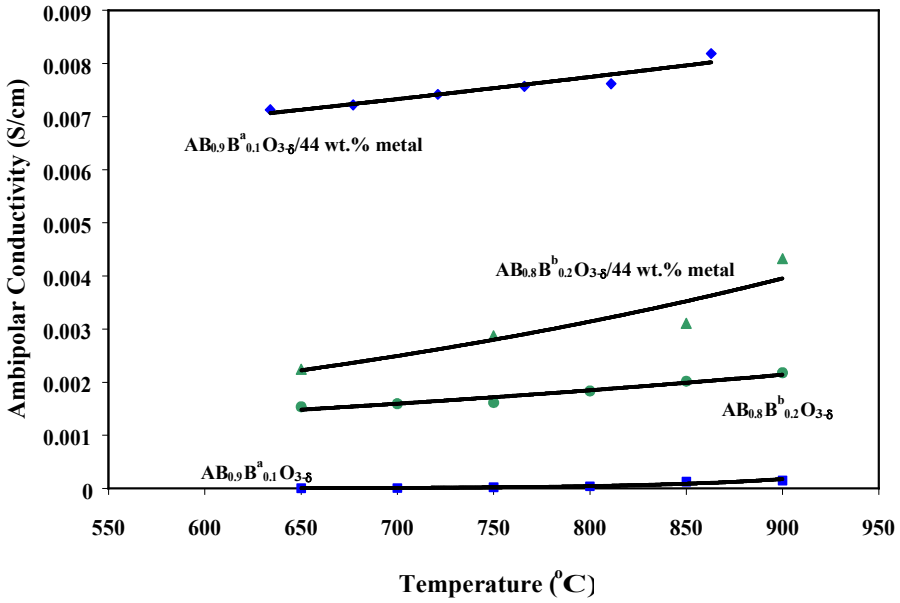

Figure 32. **Plot comparing ambipolar conductivity as a function of temperature for $AB_{0.9}B^{a}_{0.1}O_{3-\delta}$ and $AB_{0.8}B^{b}_{0.2}O_{3-\delta}$ mixed proton electron conducting ceramics, and their respective cermet analogs. The concentration of hydrogen on the feed side was 80 vol.% (bal. He), and Ar was used on the permeate side. The flow rates were 120 mL/min.**

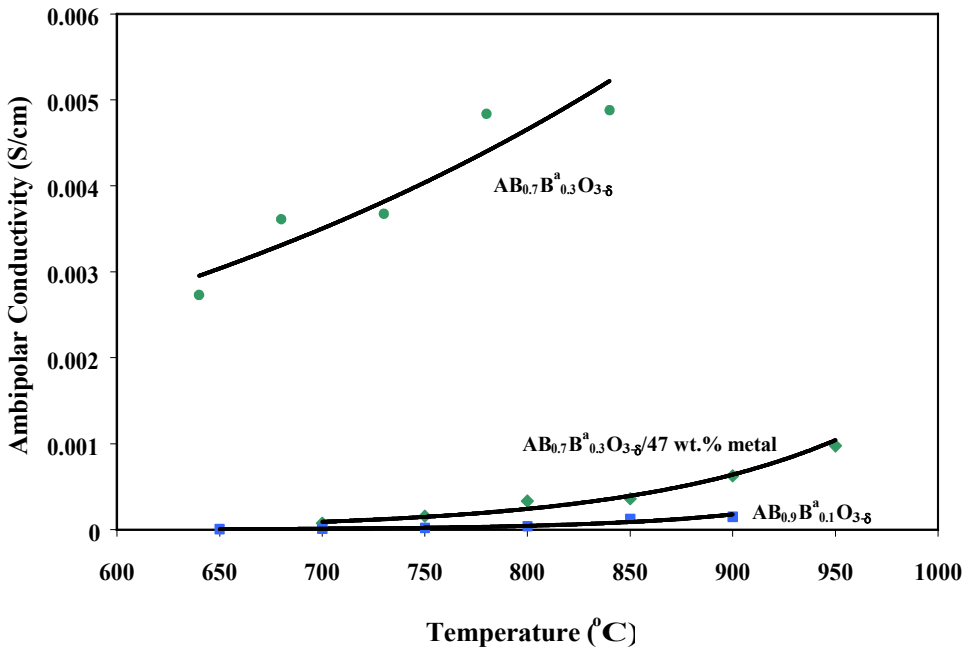

Figure 33. Plot comparing ambipolar conductivity as a function of temperature for dense hydrogen transport membranes. The concentration of hydrogen on the feed side was 80 vol.% (bal. He), and Ar was used on the permeate side. The flow rates were 120 mL/min.

Conductivity and activation energies for samples shown in the previous three figures are summarized in Table 4. Adding the metal phase to $AB_{0.9}B^{a}_{0.1}O_{3-\delta}$ significantly increased conductivity and the was a factor of 10 drop in activation energy. Similar results were observed comparing when the dopant concentration of $AB_{0.9}B^{a}_{0.1}O_{3-\delta}$ (x = 0.1) was increased to $AB_{0.7}B^{a}_{0.3}O_{3-\delta}$ (x = 0.3). The same trend in conductivity and activation energy was observed for $AB_{0.8}B^{b}_{0.2}O_{3-\delta}$ upon addition of the metal phase, however, the differences were small.

Table 4.
Comparison of Ambipolar Conductivity and Activation Energies for H_2 Transport Through Several Cermet and Ceramic Membranes.

Ceramic Phase	Wt.% Metal Phase	Ambipolar Conductivity (S/cm) at 850°C	E_a (eV)	ln A
$AB_{0.9}B^{a}_{0.1}O_{3-\delta}$	44	8.19×10^{-3}	0.14	3.6
$AB_{0.9}B^{a}_{0.1}O_{3-\delta}$	0	1.5×10^{-4}	1.4	11
$AB_{0.7}B^{a}_{0.3}O_{3-\delta}$	47	3.6×10^{-4}	1.1	11
$AB_{0.7}B^{a}_{0.3}O_{3-\delta}$	0	4.9×10^{-3}	0.34	5.3
$AB_{0.8}B^{b}_{0.2}O_{3-\delta}$	44	3.11×10^{-3}	0.30	4.5
$AB_{0.8}B^{b}_{0.2}O_{3-\delta}$	0	2.02×10^{-3}	0.22	3.1
$AB_{0.8}B^{c}_{0.2}O_{3-\delta}$	44	2.55×10^{-3}	0.20	3.2

Cermet compositions with the general formula $AB_{0.8}B^{d}_{0.2}O_{3-\delta}$/44 wt.% metal were fabricated and tested for comparison to compositions listed above. Figure 34 summarizes hydrogen transport rates for a 0.52-mm thick membrane under dry and humid conditions as a function of temperature. There was a steady increase in hydrogen permeation with temperature over the test range, with a maximum of 0.2 mL/min/cm^2 at 950°C. $AB_{0.8}B^{d}_{0.2}O_{3-\delta}$/44 wt.% metal had a maximum ambipolar conductivity of approximately 3 x 10^{-3} S/cm and an activation energy for hydrogen transport near 0.3 eV. These results essentially were equivalent to the best cermets listed in Table 4, and reflect the similar proton conductivity of $AB_{0.8}B^{c}_{0.2}O_{3-\delta}$ and $AB_{0.8}B^{d}_{0.2}O_{3-\delta}$. These newer compositions were slightly more expensive, and therefore further work was focused on the $AB_{0.8}B^{c}_{0.2}O_{3-\delta}$/44 wt.% metal cermet.

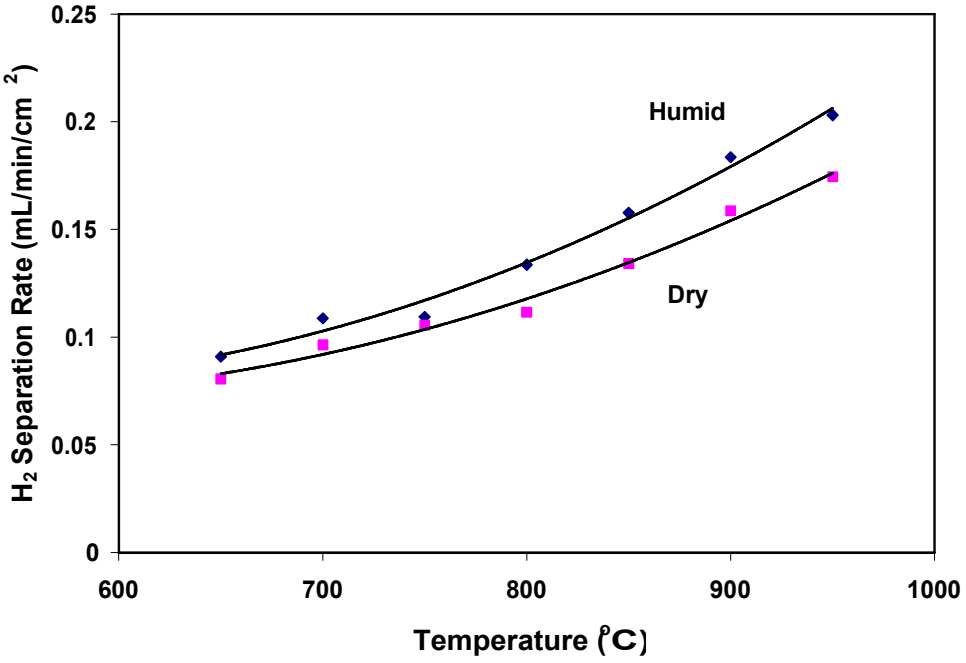

Figure 34. Plot of hydrogen transport as a function of temperature for a cermet membrane with the general formula $AB_{0.8}B^{d}_{0.2}O_{3-\delta}$ / 44 wt.% metal. The membrane thickness was 0.52 mm. The membrane feed side contained 80/20 vol.% H_2/He and Ar was used on the sweep side. Gas flow rates were between 80 and 120 mL/min.

Cermet membranes with the general composition $AB_{0.8}B^{c}_{0.2}O_{3-\delta}$/44 wt.% metal were used to measure H_2 permeation dependence on membrane thickness. The metal phase for this material had high catalytic activity for promoting H_2 dissociation, but low (negligible) H_2 permeability. Four membranes were prepared with an initial thickness >3 mm, then sanded down to 1.2, 1.0, 0.80, and 0.16 mm, respectively. Each side was sanded flat, then polished prior to testing. The results are summarized in Figure 35, and clearly show a substantial increase in H_2 permeation with decreasing membrane thickness. The increase in permeation was roughly inversely proportional to the membrane thickness, which suggested that bulk diffusion of H_2 was rate limiting, rather than interfacial reaction kinetics.[8] However, interfacial resistance does become significant for thin membranes, and this effect was evident by a slight increase in apparent activation energy for H_2 permeation as membrane thickness decreased.

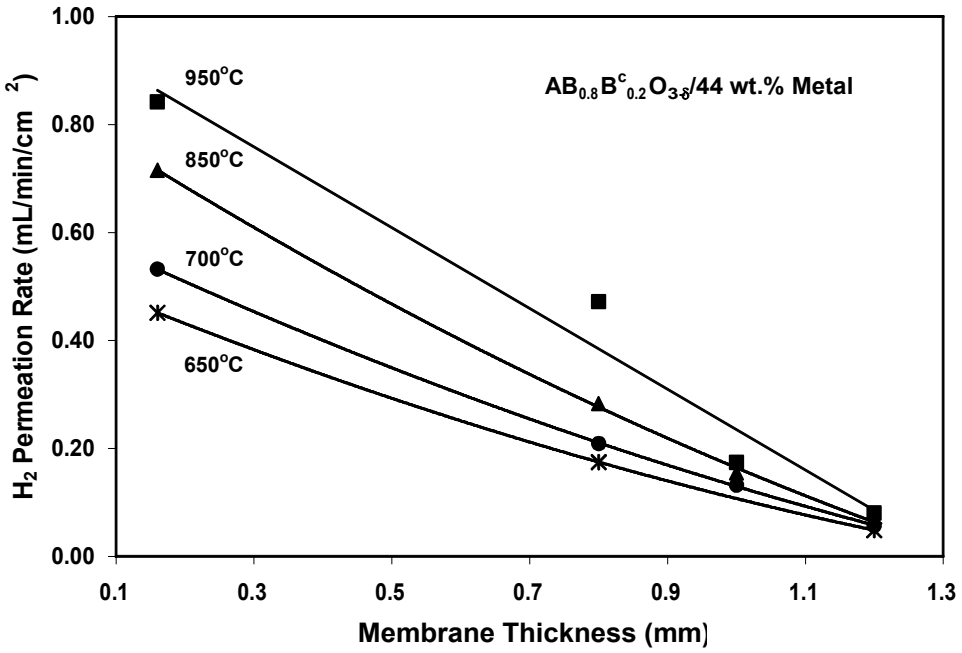

Figure 35. Plot showing H_2 permeation rate as a function of cermet membrane thickness. The inlet gas was 80 vol.% H_2 (bal. He), and the sweep gas was Ar.

The thinnest membrane in Figure 35 (0.16 mm) generated the highest H_2 permeation rate to date for this category of materials. Figure 36 shows H_2 permeation as a function of temperature under both dry and humid conditions. At 950°C, a maximum permeation rate of 0.84 mL/min/cm^2 was achieved. Moreover, at only 650°C, permeation was still significant at 0.45 mL/min/cm^2. Permeation was approximately twice as high under humid conditions than dry, which was a slightly larger difference than what is typically observed. Since moisture interacts more favorably with the ceramic surface than dry H_2, this result might reflect the greater contribution of surface kinetics to the rate limiting step of the overall permeation process for thinner membranes. However, in this case it also would be expected that moisture would improve transport more at lower temperatures than higher temperatures, which was not observed.

Figure 37 shows Arrhenius plots of conductivity (apparent, based on H_2 permeation) versus temperature, which indicated an activation energy of 0.23 eV under humid conditions compared to only 0.19 eV under dry conditions. The data fit well to a straight line, which suggested that the permeation mechanism did not change over this temperature range. Ambipolar conductivity for this sample over the temperature range shown in Figures 36 and 37 varied from 1.7 x 10^{-3} S/cm (650°C, dry) to 5.2 x 10^{-3} S/cm (950°C, humid). Since the metal phase of these materials was continuous (*i.e.*, negligible electron resistance), the ambipolar conductivity was roughly equal to the proton conductivity. However, since conductivity was calculated based on H_2 transport, the values incorporate surface polarization and are, therefore, underestimated.

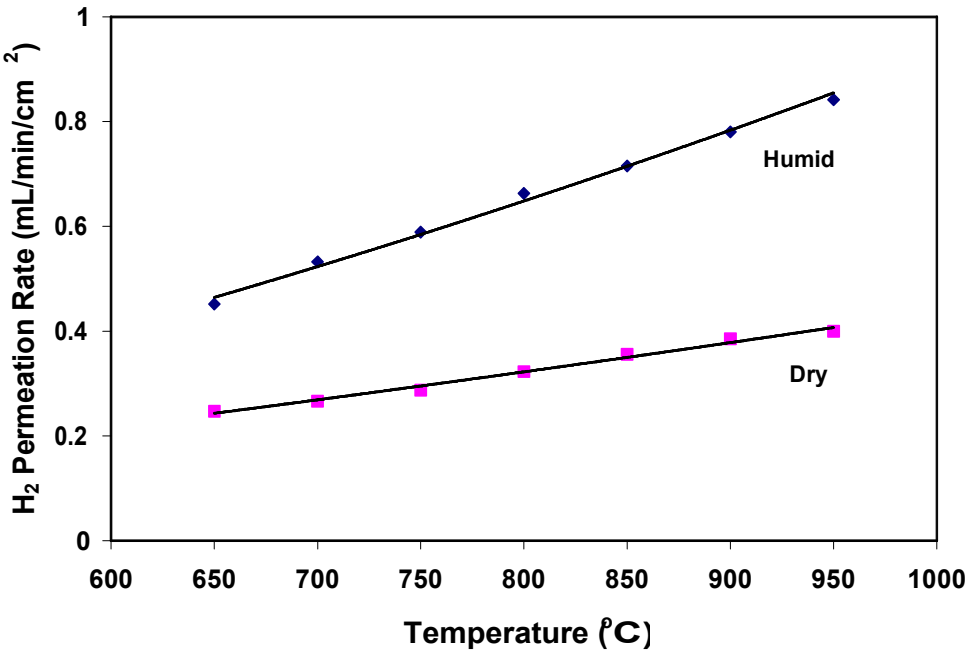

Figure 36. **Plot showing H_2 permeation as a function of temperature for a 0.16-mm thick cermet membrane with the general composition $AB_{1-x}B^{c}_{x}O_{3-\delta}$ / 44 wt.% metal. The inlet gas was 80 vol.% H_2 (bal. He) and the sweep gas was Ar.**

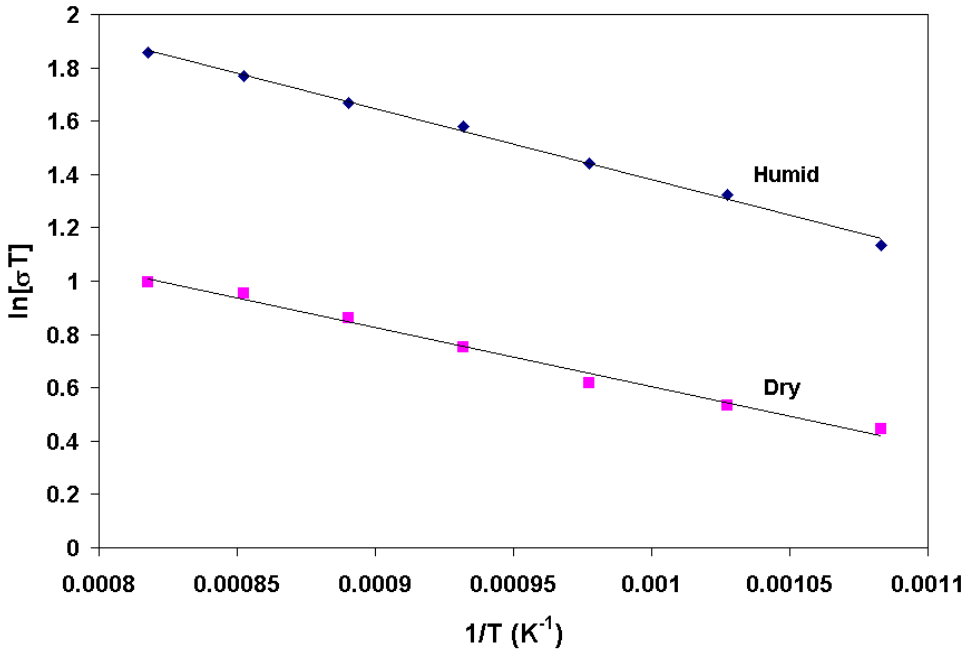

Figure 37. **Arrhenius plot showing conductivity (apparent ambipolar) versus temperature for a cermet membrane with the general composition $AB_{1-x}B^{c}_{x}O_{3-\delta}$ / 44 wt.% metal.**

Cermet development at ANL focused on the effect of microstructure, both in the ceramic and metal phases, on membrane performance. To demonstrate the range of grain size, cermet samples with the same composition (proton-conducting ceramic and 40 vol.% metal), hereafter referred to as ANL-1a, membranes were prepared with different microstructure by varying the particle size of the starting materials. The difference in resulting grain structure is shown in Figure 38. The left SEM image in Figure 38 shows that after sintering large grain sizes were found for the sample prepared using precursors with particles sizes between 2.2 and 3.0 μm. Additionally, this sample contained isolated pores, and did not sinter well. In contrast, the right side of Figure 38 shows that the sample prepared using 0.08- to 0.18-μm precursor particles sintered well, had no open pores, and much smaller grain sizes.

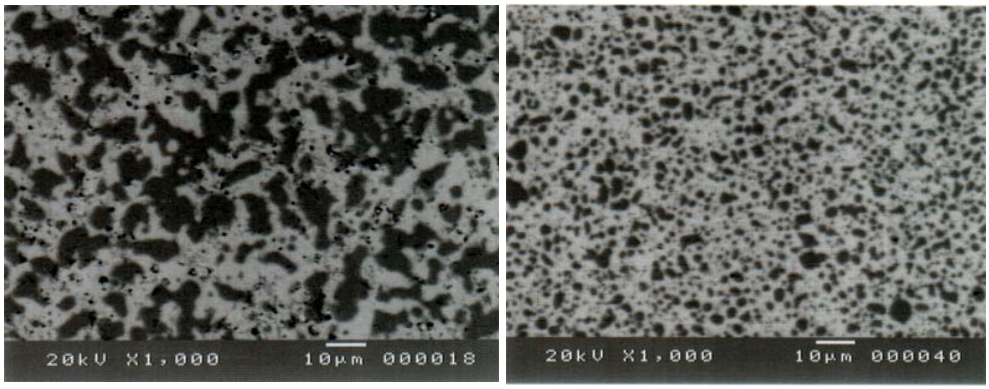

Figure 38. x1000 SEM images of 40 vol.% metal cermets prepared with micron (left) and submicron (right) precursor particles.

Figure 39 shows the hydrogen permeation of two ANL-1a membranes versus temperature, one made with small-grain metal and the other with large-grain metal. Both membranes contained 40 vol.% metal. The membrane with small-grain metal was sintered in 200 ppm H_2, that with large-grain metal was sintered in 4% H_2. The feed gas for permeation measurements was wet 4% H_2/balance He, i.e., dry 4% H_2/balance He was bubbled through water at room temperature to give ~3% H_2O. For comparison, the flux of the large-grain-metal membrane was normalized to 0.2 mm thick, the thickness of the membrane with small-grain metal. The flux of the small-grain membrane increased from 0.09 to 0.11 cm^3(STP)/cm^2-min as temperature increased from 600-900°C, while the flux of large-grain membrane increased from 0.14 to 0.17 cm^3(STP)/cm^2-min. These permeation results were counterintuitive. Decreasing the grain size increases the triple-phase-boundary at the membrane surface and hence decreases the surface resistance. This effect is expected to increase the flux of the membrane if the membrane is thin, or if the membrane is thick, have no effect on the flux. These results show that the small-grain-metal membrane gave lower flux, as seen in Figure 39. Several factors could contribute to this observation.

A lack of continuity in the small grain metal phase could result in high electrical resistance which in turn could limit flux. A series of membranes were prepared that contained 40, 42, 44, 46 and 48 vol.% of small-grain-metal powder (0.08 to 0.18 μm). When the metal content was less than 46 vol.%, the membrane was insulating, suggesting that the metal grains were isolated from one another. When the metal content was 46 vol.%, the resistance depended on where the multimeter leads contacted the membrane, with readings varying from several

hundred ohms to insulating. This suggests that metal grains were beginning to connect to one another but had not formed a completely continuous three-dimensional network. At 48 vol.%, the membrane was conductive, indicating that a three-dimensional network of metal had been formed. Microstructures of these samples were determined from back-scattered images (BEI). Compared with microstructures for membranes with 40, 42, and 44 vol.% metal, the metal grains were more irregularly shaped and had a broader size distribution when the metal content was 46 and 48 vol.%. The larger grain size and the irregular shape of the metal grains are both favorable to forming a continuous metal network, which is consistent with the conductivity results. These observations suggest that discontinuity of metal phase probably caused the small-grain-metal ANL-1a membrane to be insulating.

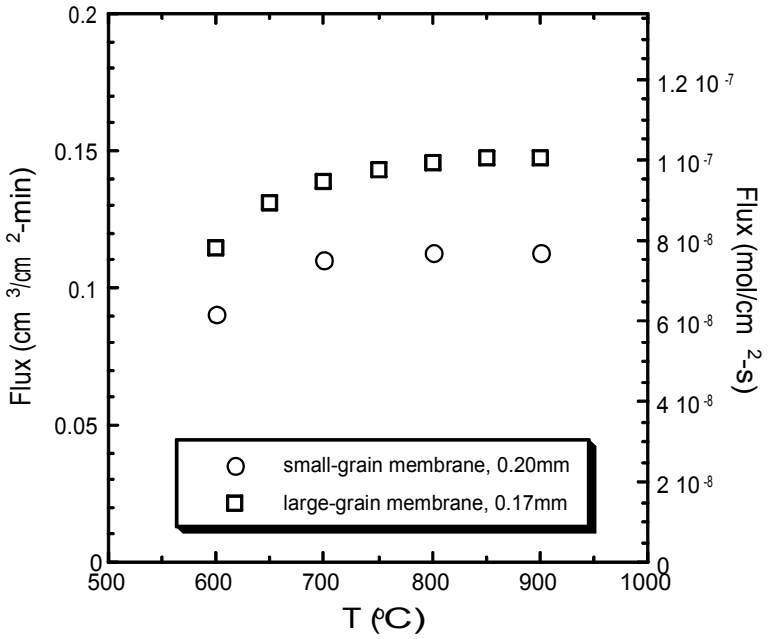

Figure 39. Hydrogen permeation of ANL-1a membranes vs. temperature with a feed gas of wet 4% H_2 / He (containing ~3% H_2O). Flux of large-grain membrane was normalized to 0.2-mm-thick for comparison. The actual thickness of 0.17 mm.

The sintering atmosphere can also affect the continuity and therefore electrical properties of the metal phase. Figure 40 shows the temperature dependence of the hydrogen flux of two ANL-1a membranes, one that was conductive after sintering in 200 ppm H_2 and another that was insulating after sintering in 4% H_2. For both types of membranes, the H_2 flux increased as temperature increased, but the flux through the conductive membrane was ~5-10 times higher than that through the insulating membrane. This result confirmed that the electronic conductivity of ANL-1a membranes limits the hydrogen permeation through its oxide phase.

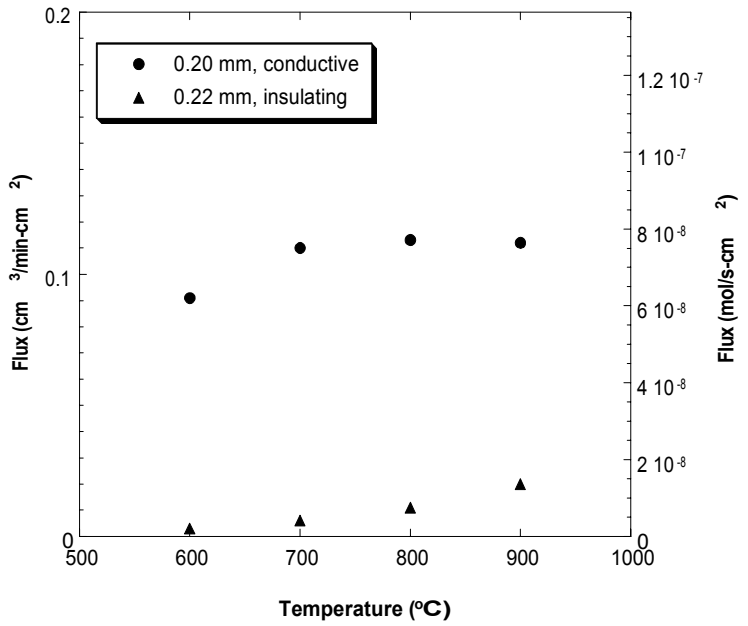

Figure 40. Temperature dependence of hydrogen flux for ANL-1a membranes in feed gas of 4% H_2 / He (containing ~3% H_2O). Membrane thickness given in inset.

Figure 41 shows the temperature dependence of the hydrogen flux of both large- and small-grained ANL-1a membranes. As expected, the flux increased for both types of membrane as the membrane thickness decreased. For membranes with thickness in the range 0.17-0.81 mm, the large-grained membranes gave higher flux than small-grained membranes. Hydrogen flux is re-plotted in Figure 42 as a function of temperature for large-grained membranes with thickness of 0.17, 0.38, and 0.81 mm. The hydrogen flux decreases as temperature increases for the thickest (0.81 mm) membrane. This result may be due to a decrease in proton conductivity with increasing temperature, which may result from a decrease in the proton charge-carrier concentration. The proton concentration may decrease because the water solubility for known perovskite-type proton conductors generally decreases with increasing temperature above about 500°C; below that temperature the water solubility is fairly constant. For the membrane with thickness of 0.38 mm, the hydrogen flux reached a maximum at approximately 650°C and then became flat. For the thinnest (0.17 mm) membrane, the hydrogen flux increased over the entire temperature range of study, although it was nearly flat above about 800°C. The results for the thinnest membrane may be related to hydrogen permeation through its metal phase. The metal phase in ANL-1a membranes is known to have a small, but measurable, hydrogen permeability at high temperatures; therefore, hydrogen permeation through the metal phase may become significant in thin membranes. For the thinnest membrane, hydrogen permeation through the oxide phase may decrease with increasing temperature, as was observed with the thick membrane, but the total hydrogen flux may still increase due to an increase in hydrogen permeation through the metal phase.

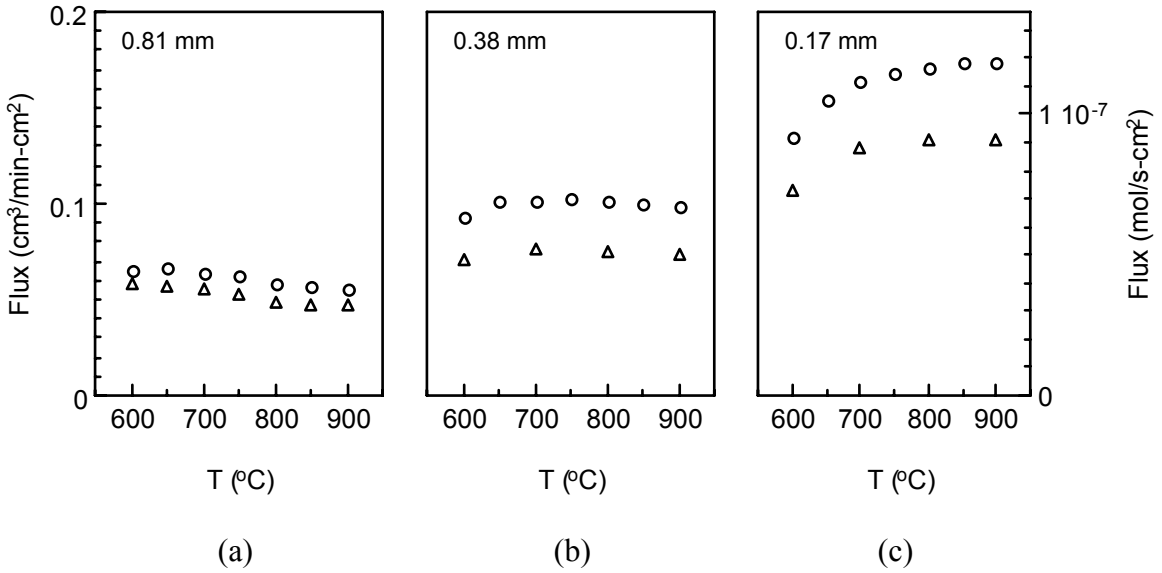

Figure 41. **Temperature dependence of the hydrogen flux for ANL-1a membranes containing metal with large-grains (circle) and small-grains (triangle). To compare the flux for small- and large-grained membranes, the flux for small-grained membranes was normalized to the same thickness as the large-grained membranes. The thickness for the large-grained membranes is given in each plot; the actual thickness for the small-grained membranes was (a) 1.16 mm, (b) 0.43 mm, and (c) 0.20 mm. Feed gas was 4% H_2/He (containing ~3% H_2O).**

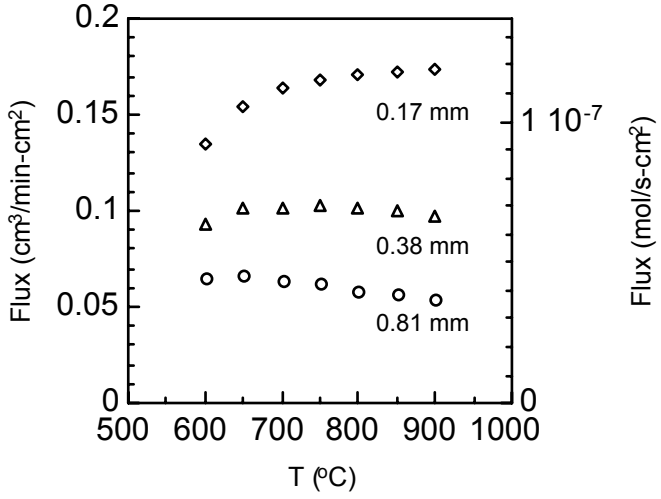

Figure 42. **Temperature dependence of the hydrogen flux of ANL-1a membranes with large-grained metal phase. Feed gas was 4% H_2/He (containing ~3% H_2O).**

The results described above clearly showed that the microstructure of the metal phase affects hydrogen permeation through ANL-1a membranes. ANL-1a membranes with large-grained metal phase gave higher hydrogen flux than those with small-grained metal phase. Alternatively, the effect of the oxide phase grain size on the hydrogen permeation of ANL-1a membranes was investigated.

To vary the grain size of the oxide phase, ANL-1a membranes were prepared using $BaCe_{0.8}Y_{0.2}O_{3-\delta}$ (BCY) powder from Praxair that was treated in two different ways. As-received BCY, so-called "fine" powder, was used to prepare one type of membrane; the other type of membrane was made with "coarse" BCY powder, which was prepared by annealing the same as-received BCY powder for 10 h at 1200°C in air. Membranes were prepared by mixing the two types of BCY powder with Ni powder (40 vol.%), which was then uniaxially pressed into disks and sintered at 1400°C in 200 ppm H_2. The same batch of fine (avg. particle size ≈0.08–0.18 μm) Ni powder was used to prepare both types of ANL-1a membrane.

Figure 43 shows scanning electron micrographs of the two types of ANL-1a membranes after sintering. The most notable difference in the two microstructures is that the average size of the metal phase (darker in color) is larger in the membrane prepared from BCY powder that had been pre-annealed. The difference in the BCY grain size is not obvious in these micrographs. In order to highlight differences in the BCY microstructure, the metal phase was removed by etching the membranes with nitric acid. SEM micrographs of the membranes after they were etched clearly show that the average BCY grain size is larger in the membrane made from pre-annealed powder (Figure 44a) than in the membrane made with as-received powder (Figure 44b). Because of its finer grain size, the membrane made with as-received BCY has a significantly larger grain boundary area. The difference in grain size was not as evident in Figure 43, probably because individual grains were blended together during polishing of the membrane.

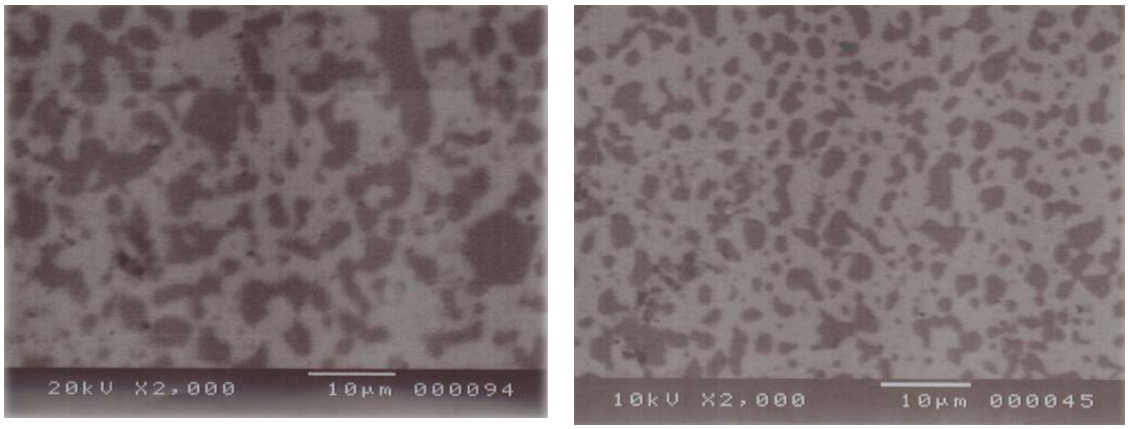

(a) (b)

Figure 43. Back-scattered electron micrographs of ANL-1a membranes sintered in 200 ppm H_2 at 1400°C. Membrane made with: (a) pre-annealed BCY, (b) as-received BCY.

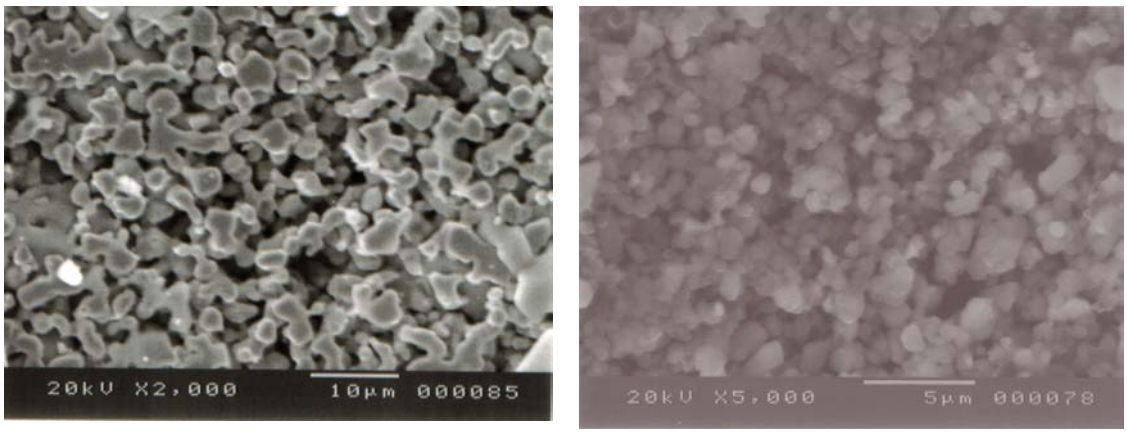

(a) (b)

Figure 44. SEM micrographs of ANL-1a membranes after being etched with HNO_3. Membrane made with: (a) pre-annealed BCY, (b) as-received BCY.

Figure 45 shows the temperature dependence of the hydrogen flux for two ANL-1a membranes, one made with as-received BCY powder and one made with pre-annealed powder. The thickness for both membranes was ≈0.35 mm. For both membranes, the flux reached a maximum at ≈650°C, similar to previous results. It is thought that the hydrogen flux reaches a maximum as temperature increases due to competition between two effects: a decrease in the proton concentration and an increase in proton mobility. Over the entire temperature range, the hydrogen flux was lower for the membrane made with as-received powder. Considering that the BCY grain size is smaller in this membrane (Figure 44b), its flux might be expected to be higher due to a larger triple-phase boundary area. The fact that the membrane made with as-received powder has a lower flux suggests that grain boundary resistance to proton diffusion may be a significant factor.

These results are consistent with ANL's previous study into the effect of metal grain size on the hydrogen flux through ANL-1a membranes, which showed that the hydrogen flux was higher for membranes with large-grained metal phase. In the present study, the membrane made with pre-annealed powder had the higher hydrogen flux, and Figure 43 shows that it had larger-grained metal phase. Although the effects of oxide grain size and metal grain size were not completely separated in the present study, the results show that higher hydrogen flux was obtained with larger-grained materials.

To further investigate the effect of microstructure on H_2 permeation in cermets ANL used impedance analysis to conduct a detailed investigation of the bulk/grain boundary conductivity of the oxide phase in ANL-la cermet membranes. To study the effect of microstructure on proton conductivity, BCY powder from Praxair was used to sinter two specimens in air for 10 hours, one at 1500°C (specimen I) and the other at 1600°C (specimen II). The fracture scanning electron micrographs of the specimens after sintering are shown in Figure 46. The sample sintered at higher temperature (Specimen II) showed larger grains and less grain boundary length per unit area.

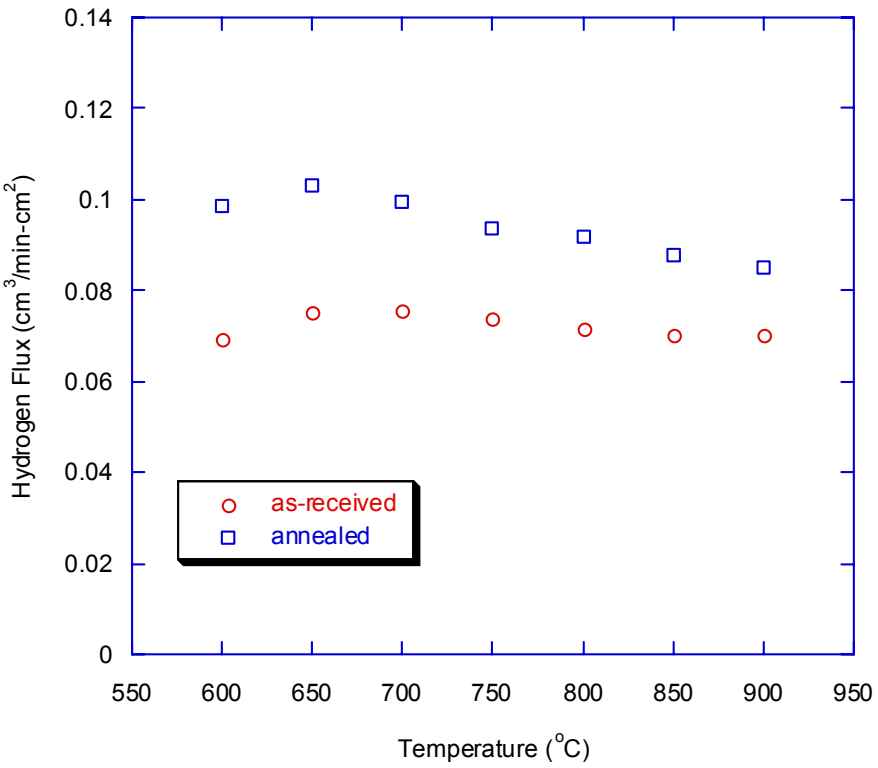

Figure 45. **Temperature dependence of the hydrogen flux of two ANL-1a membranes, one made with as-received powder (circles), another made with annealed powder (squares).**

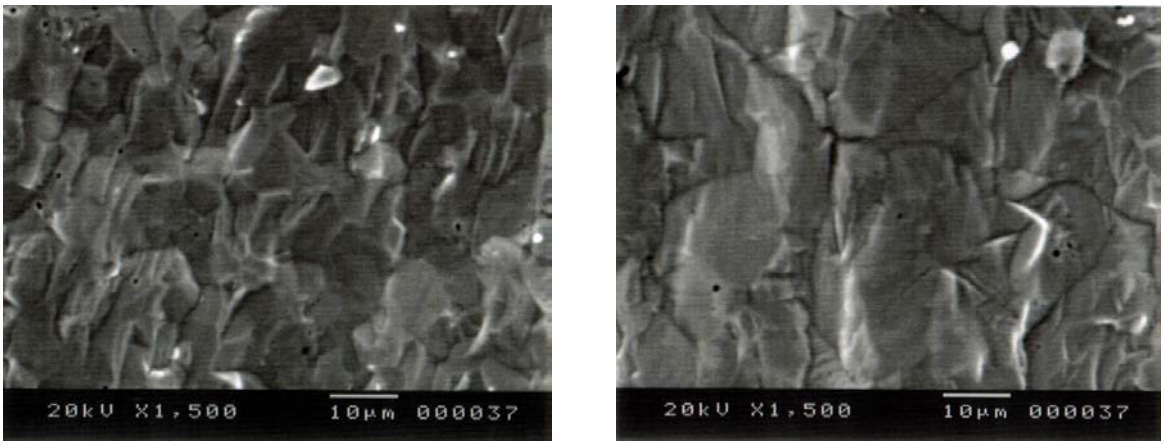

(a) (b)

Figure 46. **Scanning electron micrographs of BCY specimens sintered in air for 10 hours at (a) 1500°C, and (b) 1600°C.**

The electrical response of the BCY samples below 300°C typically showed three semicircles in the Nyquist plot: one at high frequencies corresponding to the bulk characteristics; one at medium frequencies related to the grain boundary resistance, and one at low frequencies associated with the electrode response. Comparing the impedance diagrams for specimens I and II shows that the medium frequency semicircle (associated with grain boundary resistance) was larger for specimen I than for specimen II. This result indicates that specimen I had a larger grain boundary resistance, which is reasonable because the mobile charge carriers encounter more boundaries in specimen I. Assuming a bricklayer model with an equivalent circuit of three parallel RC circuits connected in series, the impedance diagrams were fitted to obtain the resistance, characteristic frequency, and capacitance of bulk, grain boundary, and electrodes. The Arrhenius plot of the electrical conductivity is shown in Figure 47. The bulk conductivity was ≈two orders of magnitude higher than the grain boundary conductivity over the temperature range (100-300°C) in feed gas of 4% H_2/balance He (pH_2O = 0.03 atm). The significantly lower grain boundary conductivity indicates that larger-grained materials might be more suitable for proton transport.

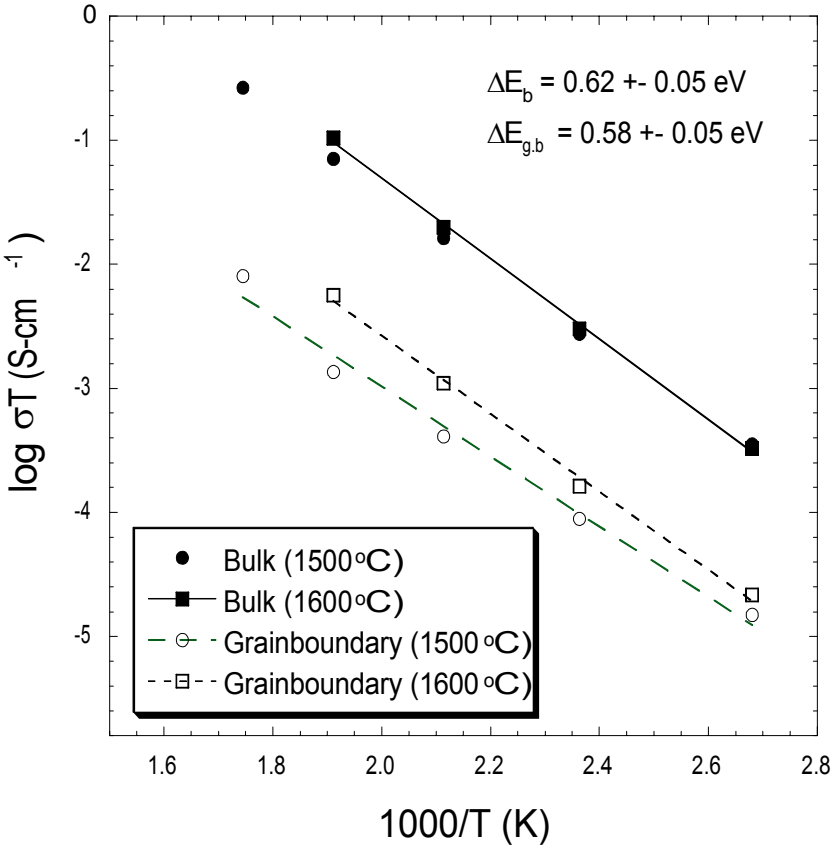

Figure 47. Arrhenius plot of bulk and grain boundary conductivity of two BCY specimens sintered in air for 10 hours, one at 1500°C, the other at 1600°C.

As temperature increases, the semicircle associated with grain boundary resistance becomes extremely small even for small-grained specimen I, therefore the grain boundary resistance cannot be separated from bulk resistance. Above 600°C, both the bulk and grain boundary response are incorporated into the high frequency offset, leaving the electrode response as the only semicircles. Figure 48 shows the Arrhenius plot of total conductivity in 4% H_2 (pH_2O = 0.03 atm) feed gas from 300-900°C. Specimen II, with larger grains, showed higher conductivity at 900°C (5.31 x 10^{-2} S-cm^{-1}) than did specimen I (2.68 x 10^{-2} S-cm^{-1}) with smaller grains. Because the two specimens have the same macroscopic geometry, and their bulk and grain boundary conductivities are expected to be identical, the difference in total conductivity should mainly reflect a difference in their microstructures. This suggests that the grain boundaries may not provide a pathway for fast proton transport, and that bulk transport makes a major contribution to the total conductivity at higher temperature.

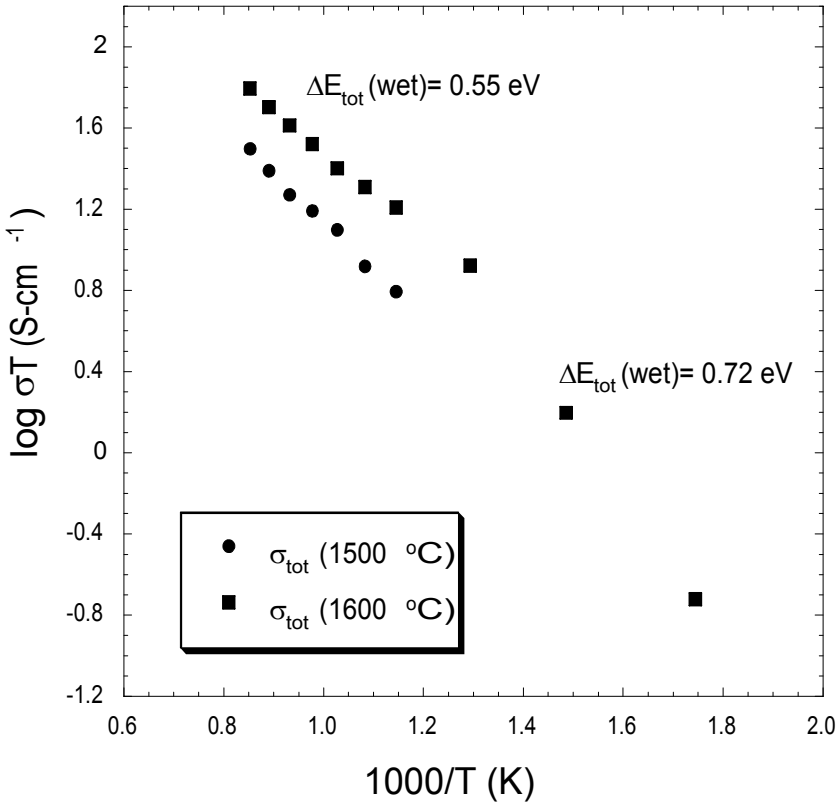

Figure 48. Temperature dependence of total electrical conductivity of two BCY specimens sintered for 10 hours in air, one at 1500°C, the other at 1600°C.

These results are consistent with the results described above on the effect of oxide grain size on the hydrogen flux through ANL-1a membranes, which showed that the hydrogen flux was higher for large-grained membranes due to higher proton conductivity for the bulk than for the grain boundaries.

Thicker ANL-1a membranes were tested in the range of 80-1160 μm. ANL-1a membranes contain a proton-conductor ($BaCe_{0.8}Y_{0.2}O_{3-a}$, i.e., BCY, purchased from Praxair) and an electron-conductor (Ni metal, purchased from Alfa Aesar). The metal phase boosts the

ambipolar conductivity of the membrane by increasing its electronic conductivity. Because atomic hydrogen diffusion through the Ni phase is also detectable under some conditions, the total hydrogen flux through ANL-1a membranes, J_{H_2}, is expressed as the sum of ambipolar and atomic diffusion:

$$J_{H_2} = -\{\frac{RT}{4F^2L}\int_{P_{H_2}^{sweep}}^{P_{H_2}^{feed}} \frac{\sigma_{OH_O^{\bullet}}\sigma_{e'}}{\sigma_{OH_O^{\bullet}}+\sigma_{e'}} d\ln P_{H_2} + \frac{P}{L}\nabla P_{H_2}^{1/2}\} \quad (12)$$

In this equation, i is the partial conductivity of conducting species (i = $OH_O^{\bullet}$, e), R is the gas constant, F is Faraday's constant, T is temperature, P is the hydrogen permeability of Ni, and it is assumed that oxygen potential gradients do not influence the hydrogen flux. The hydrogen flux through the Ni phase was calculated using permeability data in the literature with the known applied chemical potential gradients and the measured membrane thickness. The ambipolar flux was calculated by subtracting the flux through Ni from the measured total flux. Figure 49 shows the hydrogen flux attributed to each diffusion mechanism as a function of temperature for feed gas of 4% H_2/balance He with pH_2O of 0.03 atm. The flux due to ambipolar diffusion dominates over the entire temperature range investigated, but the flux through Ni increases with temperature due to the increase of hydrogen permeability.

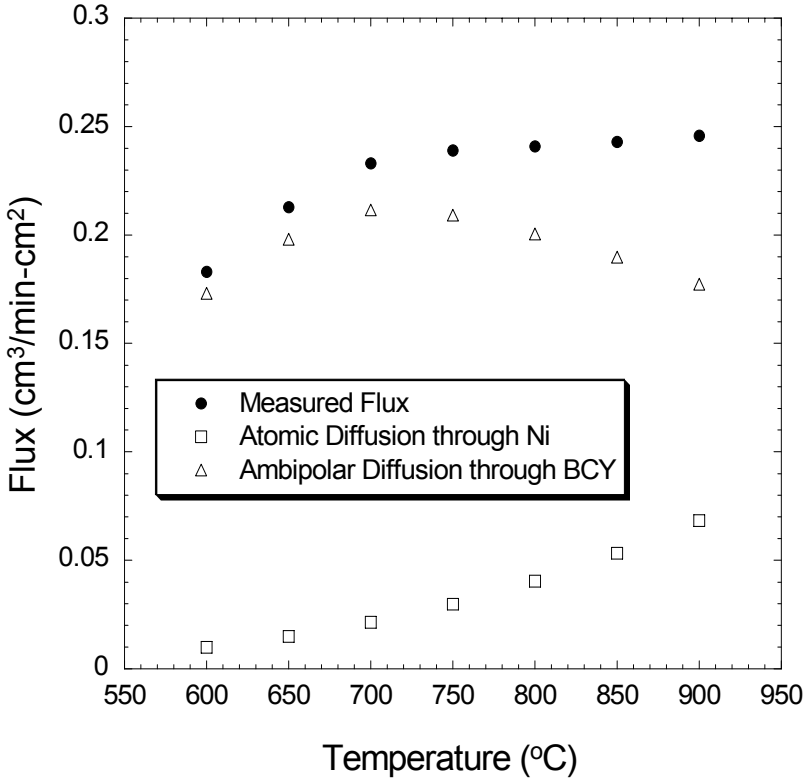

Figure 49. Measured hydrogen flux for 80- µm-thick ANL-1a membrane using feed gas of 4%H_2/balance He (pH_2O = 0.03 atm) with calculated contributions from ambipolar diffusion through BCY and atomic diffusion through Ni.

The total hydrogen flux is shown versus temperature (Figure 50a) for ANL-1a membranes with thickness of 80-1160 μm using feed gas of 4% H_2/balance He with pH_2O of 0.03 atm. The results show that the temperature dependence of hydrogen flux varies with the membrane thickness. For thicker (>640 μm) membranes, the flux decreases monotonically as temperature increases up to 900°C, but the flux for thinner (<200 μm) membranes increases as temperature increases up to ≈750°C and then is nearly constant at higher temperatures. Membranes with intermediate thickness show a transition between these two types of behavior.

Figure 50b shows the flux due to ambipolar diffusion as a function of temperature. The ambipolar flux for thicker membranes, like the total flux, decreases monotonically as temperature increases. For thinner membranes, the flux due to ambipolar diffusion increases up to a temperature of ≈700°C and then decreases as temperature increases further. This difference in the temperature dependence of flux might indicate that the kinetics of interfacial reactions dominate the properties of thin membranes at low temperature but are not dominant for thick membranes. In this case, the flux through thin membranes increases with temperature at low temperatures (<700°C) due to thermal activation of rate-controlling surface reactions. At higher temperatures, where bulk processes dominate, the flux through thin membranes decreases due to the decrease in proton conductivity that results from a decreasing proton concentration. The decrease in proton concentration is indicated by the decrease in water solubility for perovskite-type proton conductors above 500°C, and is expected because the proton incorporation reaction is exothermic. In contrast to thin

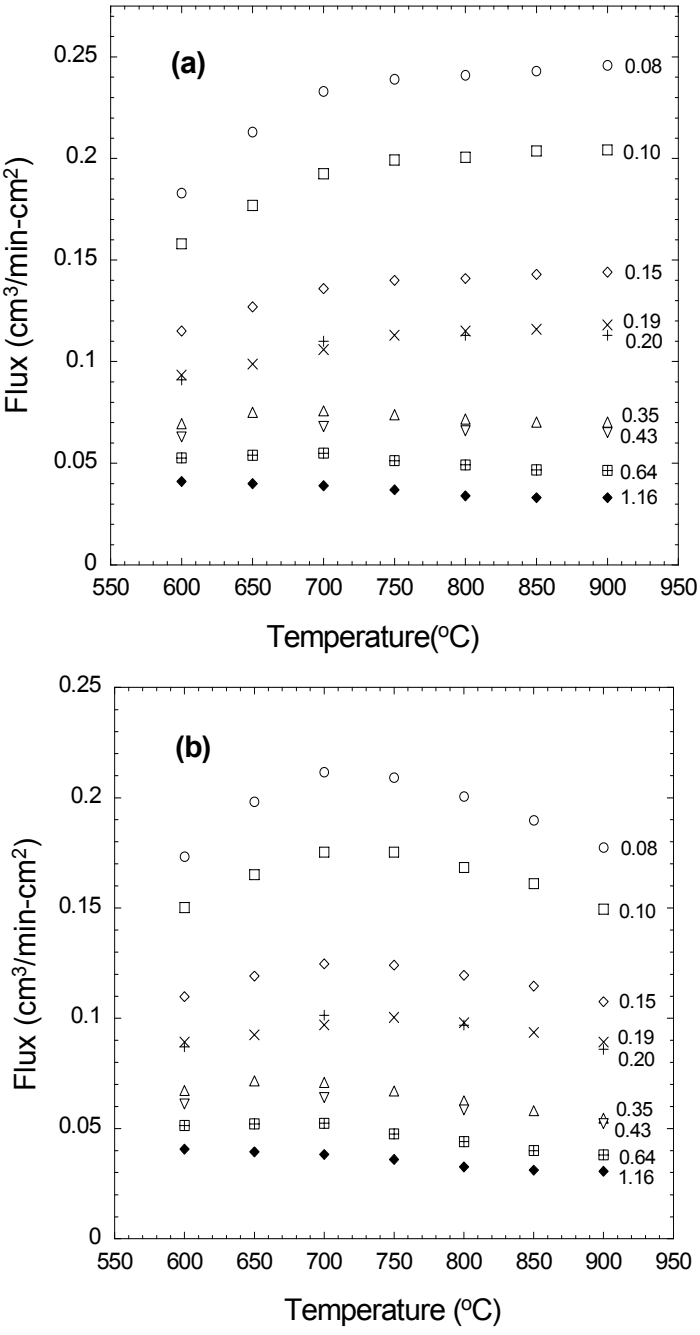

Figure 50. (a) Measured hydrogen flux, and (b) calculated flux due to ambipolar diffusion through BCY for ANL-1a membranes with various thickness (given in mm) using 4%H_2/balance He (pH_2O = 0.03 atm) feed gas.

membranes, thick membranes do not exhibit a low-temperature regime in which the flux increases as temperature increases, because bulk properties dominate their behavior. As a result, the flux of thick membranes monotonically decreases as temperature increases, because the decrease in proton concentration reduces the proton conductivity.

D. Cermets with H_2 Permeable Metal (Eltron, CoorsTek)

Although the metal phase used in the above samples has some hydrogen solubility and mobility, it is not considered a "hydrogen permeable metal." As an alternative to the above cermets, additional materials were prepared and tested with the general composition ABO_3/x%M where M represent a metal with high hydrogen permeability. Similar membranes are under development by others.[5,9] Figure 51 shows preliminary results for a ABO_3/57 wt.% metal cermet. In this case, the hydrogen transport mechanism is not necessarily ionic/electronic, so the data is presented in terms of transport rate rather than conductivity. For a 1-mm thick membrane, the transport rate increased from 0.3 mL/min/cm^2 at 700°C to 0.6 mL/min/cm^2 at 950°C. These rates were approximately two to ten times as high as the best results for the analogs containing a metal not permeable to hydrogen.

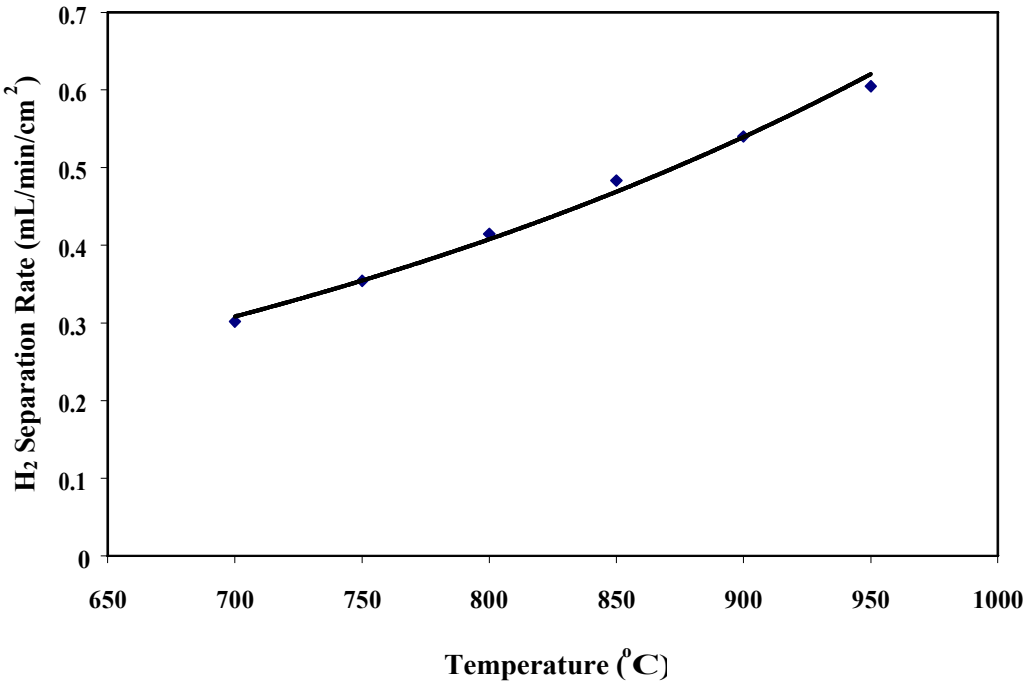

Figure 51. Plot showing hydrogen separation rate as a function of temperature for a cermet membrane containing a hydrogen-permeable metal. The membrane was ~1 mm thick, and the hydrogen was dry. The inlet hydrogen concentration was ~80 vol.% (bal. He), and argon was used as the sweep gas. Flow rates were 120 mL/min.

Figure 52 shows the H_2 permeation rate as a function of temperature for two membranes with different ceramic compositions. Both membranes were approximately 1 mm thick, and the permeation rates observed were several times higher than ceramic membranes without the metal phase. The sample with the ABO_3 ceramic had higher maximum H_2 permeability at 0.60 mL/min/cm^2, however, at lower temperatures permeability was higher using the $AB_{0.8}B^c_{0.2}O_{3-\delta}$ ceramic. The fact that the ceramic phase influenced permeability suggested that the permeation mechanism was not exclusively associated with the metal phase. Furthermore, the data in Figure 52 also demonstrated that humidity improved permeation, which is a quality associated with the ceramic phase.

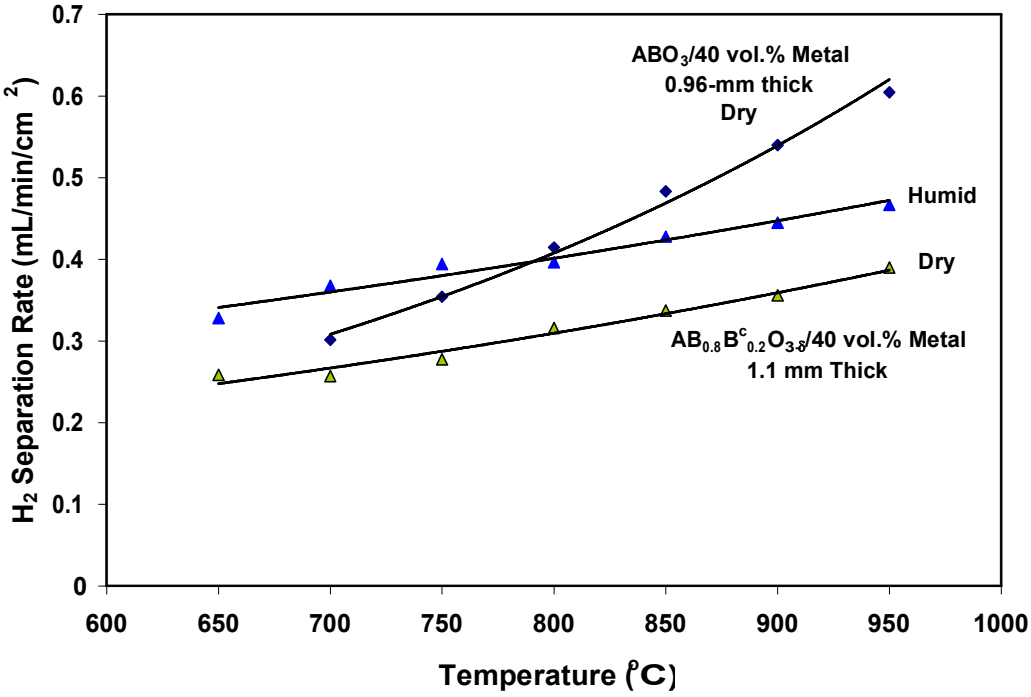

Figure 52. Plot showing H_2 permeation versus temperature for two cermet membranes containing a H_2-permeable metal. The inlet gas was 80 vol.% H_2 (bal. He) and the sweep gas was Ar.

Figure 53 shows H_2 permeation rates as a function of temperature for three membrane thicknesses. At 950°C, reducing membrane thickness from 1.1 to 0.43 mm increased permeation from 0.47 to 1.8 mL/min/cm^2, which significantly exceeded the inverse thickness dependence. Furthermore, the 0.43-mm thick membrane enabled H_2 permeation greater than 1 mL/min/cm^2 at only 650°C.

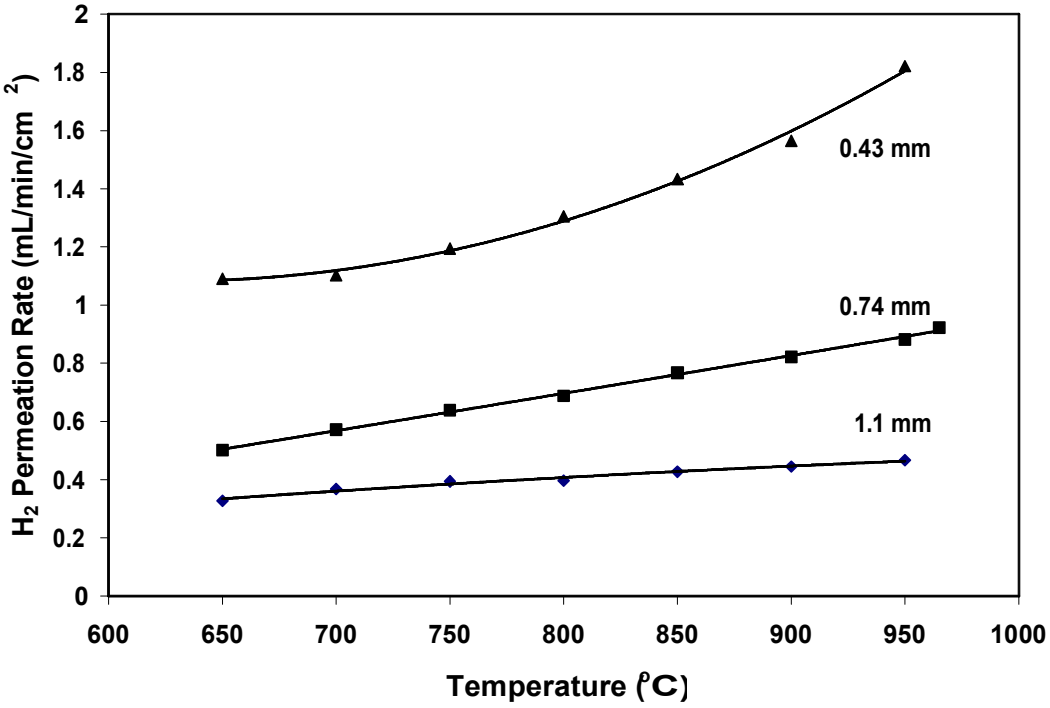

Figure 53. Permeation data for cermet membranes of different thicknesses containing a metal with high H_2 permeability. The inlet gas was 80 vol.% H_2 (bal. He) and the sweep gas was Ar.

In an effort to minimize the thickness of the H_2 permeable phase, graded cermet membranes were fabricated as diagramed in Figure 54 and shown in the cross-section SEM micrograph in Figure 55. The concentration of the metal phase in these structures increased from one side to the other, with a corresponding decrease in ceramic phase content. The metal phase was continuous through the structure; however, the change in phase distribution was most severe at the outer edges, where the membrane was mostly metal. The metal "layer" shown in the micrograph in Figure 55 was between 10 and 15 µm. The membrane was dense on the metal side, but the porosity of the mostly ceramic side has not yet been determined. It is anticipated that these structures will function similarly to supported thin film membranes, except that in this case the film is thoroughly integrated with the support surface and any discontinuity in the metal film is filled with dense ceramic. Preliminary results for this category of membranes are shown in Figure 56. The bottom two curves were for membrane samples prepared by sanding away both sides of the original structure. These samples did not contain the primarily metal layer, and were representative of

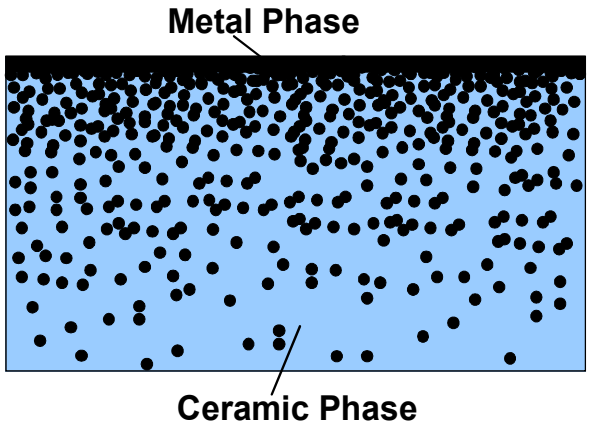

Figure 54. Diagram of a graded cermet cross section used for H_2 separation.

the membrane bulk. Permeation for these samples increased from approximately 1 to 3 mL/min/cm^2 at 800 to 900°C as the membrane thickness decreased from 0.16 to 0.08 mm. The top curve in Figure 56 was from a membrane prepared by sanding away only one side of the original structure so that the metal surface layer remained. Despite being a much thicker membrane (0.2 mm), this sample achieved a maximum H_2 permeation of nearly 4 mL/min/cm^2 at 950°C, and 2.6 mL/min/cm^2 at only 650°C. It should be noted that these results were not corrected for standard pressure, which would lower permeation rates by 10 to 20%.

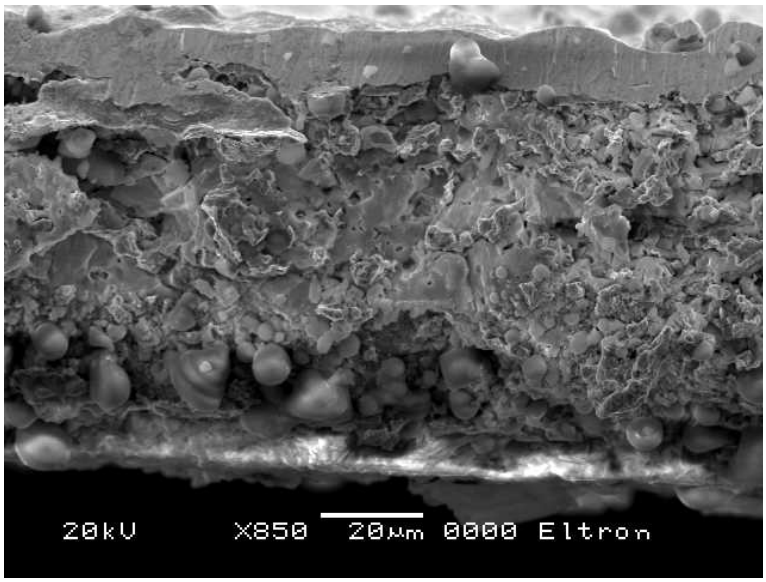

Figure 55. SEM micrograph of a cross section of a graded cermet membrane.

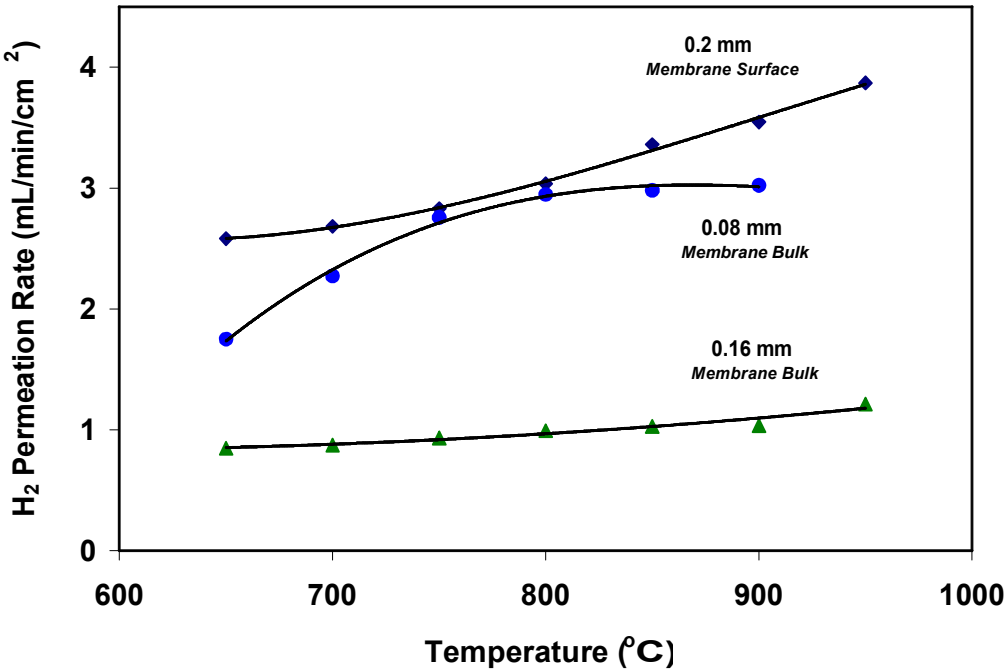

Figure 56. Plot showing H_2 permeation for graded cermet membranes containing a H_2-permeable metal. The lower two curves show results for membrane sections from the center (bulk) of the structure shown in Figure 55. The top curve is from a membrane section that included the mostly metal surface. The feedstream was humidified H_2 (bal. He) and the sweep gas was Ar. Flow rates were between 80 and 120 mL/min.

It was desirable to incorporate low-cost hydrogen permeable metals into cermets as an alternative to high cost palladium. The first attempts to produce cermet analogs resulted in structurally stable membranes; however, in addition to the ceramic and metal phases, undesired oxide and carbide phases also were present. Adjusting the sintering conditions and atmosphere improved the membrane compositions, and prevented undesired phase formation. Figure 57 contains H_2 permeation data as a function of time for a cermet represented as CER3/60 vol.% Metal-2, where CER3 is a ceramic with negligible proton conductivity or H_2 permeation and Metal-2 is a low-cost hydrogen permeable metal. The membrane was 0.83 mm thick and did not contain a catalyst to promote H_2 dissociation or protect the surface. Only results at high-temperature were obtained (750°C) and the data shows a substantial decrease in permeation from 0.37 to 0.21 mL/min/cm^2 over 193 minutes of testing. Post-run XRD analysis revealed dramatic changes to both the feed and sweep sides of the membrane, which explain the loss of permeation. Specifically, the sweep side demonstrated a reduction in the metal-to-ceramic ratio and a significant quantity of the oxide of the metal phase (likely from a leak in the system). The feed side also showed a reduction in the metal-to-ceramic ratio, as well as the presence of numerous unidentified peaks. These peaks did not appear to be associated with common hydrides or oxides of the metal phase. SEM analysis of the membrane before and after permeation measurements corroborated the XRD results and demonstrated major morphological changes, including an increase in surface roughness and extensive micro-cracks. These results highlight the reactivity of the metal phase and underscore the need for a protective/catalytic surface coating with this category of membrane. Also, it is likely that this test temperature was much too high for this category of materials.

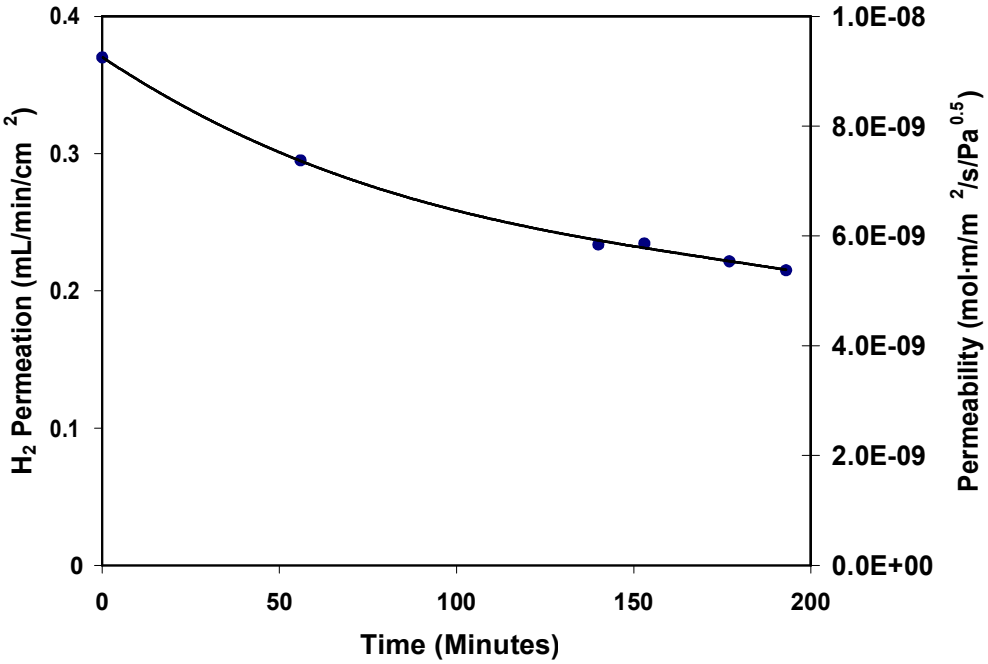

Figure 57. Hydrogen permeation as a function of time at 750°C for a 0.83-mm thick cermet represented as CER3/60 vol.% Metal-2. The membrane did not contain a catalyst. The feed gas was 80 mL/min 80/20 H_2/He and the sweep gas was ~110 mL/min Ar.

A second set of membranes were prepared with only 40 vol.% Metal-2, and the membranes were coated with a 0.1-µm thick Pd layer on each side. XRD analysis confirmed the presence of the ceramic and metal phases, in addition to a significant quantity of an undesired carbide. For this sample, testing was initiated at 700°C and permeation measurements were obtained as the membrane cooled at 1°C/min. The results are shown in Figure 58. A direct comparison to the above membrane was not possible since testing was performed at a lower temperature (*i.e.*, 700 instead of 750°C). However, the maximum permeation rate of 0.18 mL•min^{-1}•cm^{-2} was roughly two times lower than the analog with 60 vol.% metal. This permeation rate corresponded to an apparent diffusivity 2.8 x 10^{-8} m^2/s, a permeability of 4.1 x 10^{-9} mol·m^{-1}•s^{-1}•Pa-$^{0.5}$, and activation energy of 53 kJ/mol. Despite the Pd coating, post run XRD analysis indicated formation of oxides of the metal phase on both sides of the membrane, and a hydride of the metal phase on the H_2 feed side. Subsequent SEM/EDX analysis revealed that the 0.1-µm Pd film was not sufficient to cover the membrane surface.

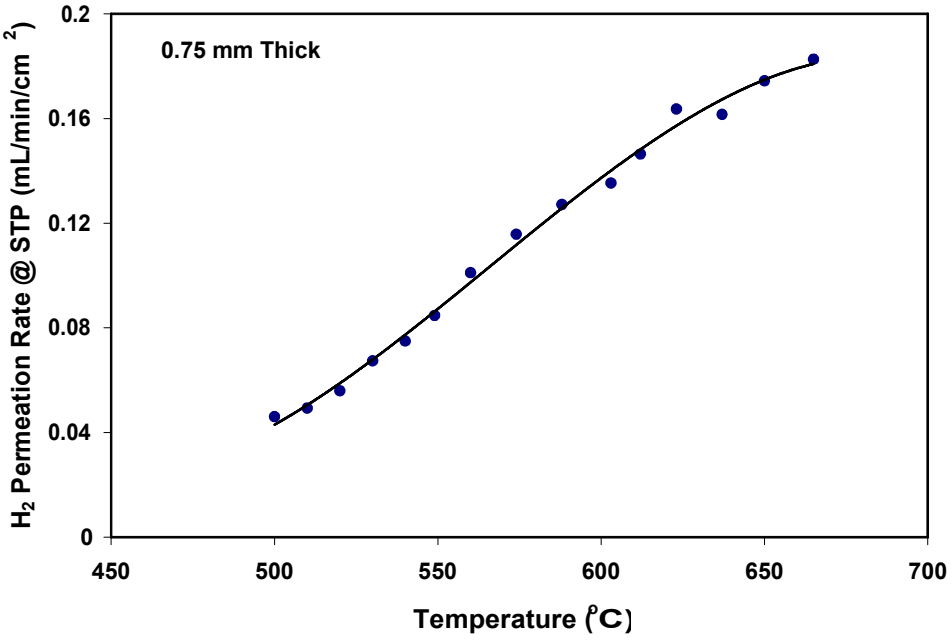

Figure 58. Hydrogen permeation rate as a function of temperature for a 0.75-mm thick membrane with the composition CER3/40 vol.% Metal2. The membrane contained a 0.1-µm thick Pd layer on side. The feed gas was 80/20 H_2/He at 80 mL/min and the sweep gas was Ar at ~111 mL/min. Permeation rates were corrected for standard temperature and pressure.

Incorporating the main metal components of the above layered composites into a ceramic matrix might improve ruggedness and versatility and simplify manufacturing. Figure 59 show permeation vs. hydrogen feed concentration for a cermet containing 60 vol.% of a relatively inexpensive H_2-permeable metal. A maximum permeation of 3.6 mL·min^{-1}·cm^{-2} was observed at 320°C. The ceramic phase had negligible H_2 permeation or proton conductivity, so permeation was exclusively through the metal phase. A thin layer of Pd was deposited onto the membrane surfaces to catalyze uptake of H_2 into the membrane.

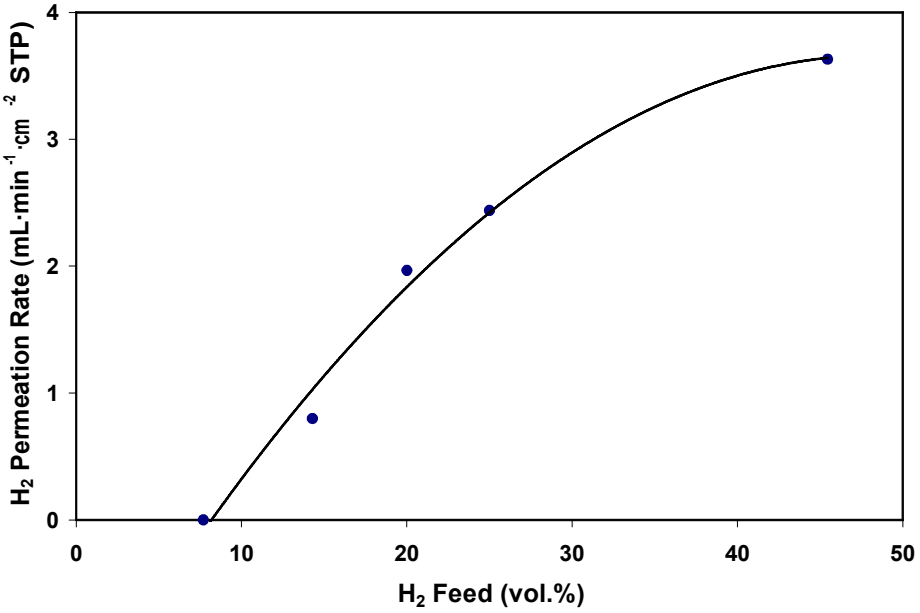

Figure 59. Hydrogen permeation rate as a function of feed concentration for a 0.8-mm thick cermet at 320°C.

Hydrogen separation performance of cermets would be significantly improved if the metal phase was a metal with a higher permeability than palladium. CoorsTek screened eleven different cermets containing high permeability metals. Variables under consideration include ceramic phase and particle size, weight percent metal phase, sintering temperature and time, and sintering atmosphere. The volume percent of ceramic phase in the prepared cermets ranged from 40 to 60 volume percent ($^{v}/_{0}$). Sintering trials were performed at a variety of temperatures in an effort to minimize porosity of the cermet. SEM analysis of the resulting cermets showed uniform composites with high densities and distinct phase separation, as shown in Figure 60.

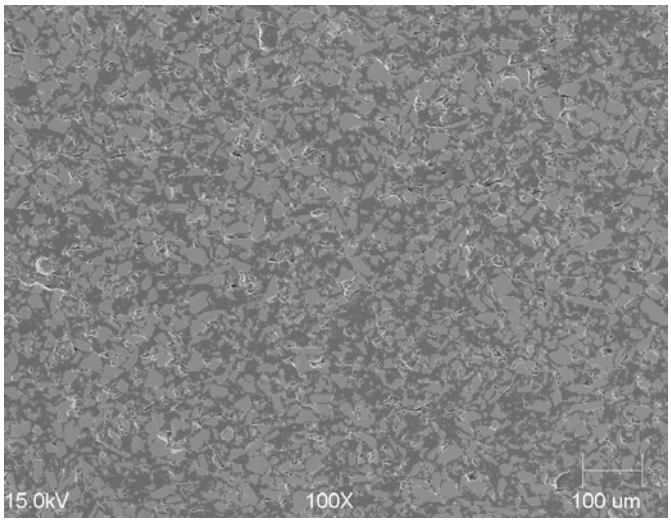

Figure 60. x100 SEM image of a 60 $^{v}/_{0}$ ceramic phase 40 $^{v}/_{0}$ high permeability metal phase cermet.

Following screening of several different composition, CoorsTek focused on developing the processing conditions necessary to sinter a single cermet composition referred to as EC101 containing a high permeability metal and a ceramic phase. Temperatures, ramp rates, and atmospheres were fine tuned to achieve planar membranes. Results showed that sintering under the appropriate conditions led to cermets with less than 1% open porosity and distinct metal and ceramic phases as characterized by X-ray diffraction. Effort was also focused on developing appropriate seals for hydrogen permeation testing of these materials. Several different sealing techniques were investigated. Key issues included ability to form a leak free seal while preventing contamination of the membrane surface. Two different types of brazed seals were leak tested at Eltron Research, Inc on membranes 13-15 mils thick.

The stability of the as prepared membrane surface was also characterized. The surface of one of the prepared cermet disks was characterized with X-ray diffraction before and after a wet-polish. No surface degradation or undesired oxide phases were observed. In addition, the sample was allowed to sit exposed to air for one month following the wet polish. After one month the disk was once again characterized with X-ray diffraction and no undesired phases were observed. These results are encouraging as they demonstrate that the surface of these cermets is stable to exposure to air and water.

CoorsTek finalized the processing conditions necessary to sinter a new cermet referred to as EC101 containing a high permeability metal and a ceramic phase. Final temperatures, ramp rates, and atmospheres resulted in a high density cermet with distinct cermet and metallic phases. Planar EC101 membranes were sealed for high temperature testing. Hydrogen permeability was determined at 350^{o}C and under five different hydrogen concentrations in the feed stream. Testing results showed the EC101 cermet had a higher permeability than other cermets tested in the reported literature.

E. Intermediate Temperature Composite Layered Membranes (Eltron)

The hydrogen separation performance of intermediate temperature composite layered membranes far exceeded the performance of any other membrane type. These membranes were evaluated using both ambient and high pressure reactors. Results for ambient pressure experiments are described here. Results for high pressure experiments are described under Task 3.

As described above, cermets containing H_2 permeable metals demonstrate significantly higher permeation rates than other analogs, and potentially operate at temperatures more compatible with gas cleanup technologies. Unfortunately, many of these metals and alloys are very expensive. Therefore membrane development was initiated to overcome these limitations by focusing on much less expensive metals and alloys. This type of membrane would consist of a graded structure where the metal phase primarily is restricted to a thin film on one surface. This arrangement is analogous to a supported thin metal film membrane, except that the metal film is very well integrated with the support and the membrane is prepared using conventional ceramic processing methods. Development of inexpensive membranes with H_2 permeable metals was initiated by first testing the permeation characteristics of the metal phase alone. Results are shown in Figure 61 for a 0.13-mm thick composite metal membrane (not a cermet) and were obtained using a room temperature mechanical seal. At 400^{o}C, this membrane permeated nearly 20 $mL \cdot min^{-1} \cdot cm^{-2}$ of H_2 (corrected for STP) with no leak. Permeation increased steadily to 24.6 mL/min/cm^2 at 470°C.

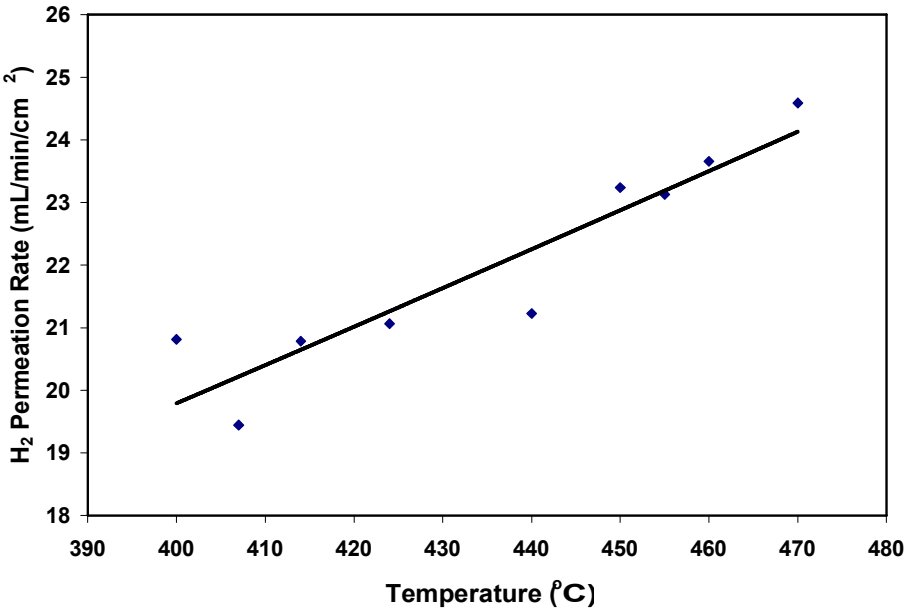

Figure 61. **Hydrogen permeation rate as a function of temperature for a composite layered metal membrane. The permeation rate was corrected for standard temperature and pressure. The feed gas was ~170 mL/min 80/20 H_2/He and the sweep gas was ~250 mL/min Ar.**

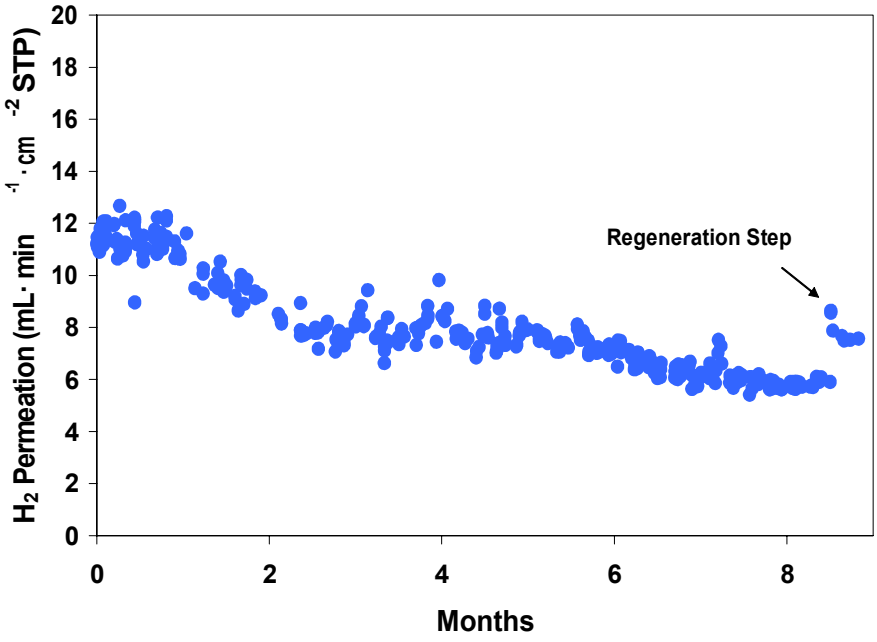

Figure 62. **Hydrogen permeation versus time at 320°C for a layered metal/ceramic composite membrane. The feed gas was 80 mL/min 80/20 H_2/He, and the sweep gas was 250 mL/min Ar.**

Figure 62 shows hydrogen permeation over nine months of continuous operation for a layered metal/ceramic composite membrane at 320°C. The total thickness of the membrane structure was approximately 2 mm, with only 0.13 mm from the permeable metal phase. Over the first 500 hours of operation, permeation remained steady at approximately 11.5 $mL \cdot min^{-1} \cdot cm^{-2}$. There was a slow loss of performance between 500 and 1700 hours, which stabilized at roughly 8 $mL \cdot min^{-1} \cdot cm^{-2}$ until 4000 hours. Over the remaining 2000 hours, permeation decreased steadily to approximately 6 $mL \cdot min^{-1} \cdot cm^{-2}$. An attempt was made to restore performance by applying an oxidation cycle using flowing air at 320°C for 24 hours. As evident in the figure, permeation increased to nearly 9 $mL \cdot min^{-1} \cdot cm^{-2}$ before stabilizing at approximately 8 $mL \cdot min^{-1} \cdot cm^{-2}$. This result suggested that at least some of the deactivation was from surface contamination, and that the membrane was sufficiently rugged to tolerate strongly oxidizing conditions.

F. Membrane Surface Catalysis (Süd Chemie Inc., Eltron)

Depending on the type of membrane utilized, the membrane itself may have catalytic activity or additional catalyst(s) may be added to the membrane surface. In either case, all hydrogen separation membranes require catalytic surfaces to promote hydrogen dissociation on the feed or retentate side of the membrane and hydrogen desorption on the sweep or permeate side of the membrane. During this project catalysts were developed simultaneously with membrane development. It should be noted that at the beginning of the project hydrogen separation membranes were thick and therefore bulk limited. In this case little to no effect was observed when testing different catalysts. As membrane performance increased and membrane thickness decreased, membranes became surface kinetics limited rather than bulk limited. In this case surface catalysts did affect membrane performance.

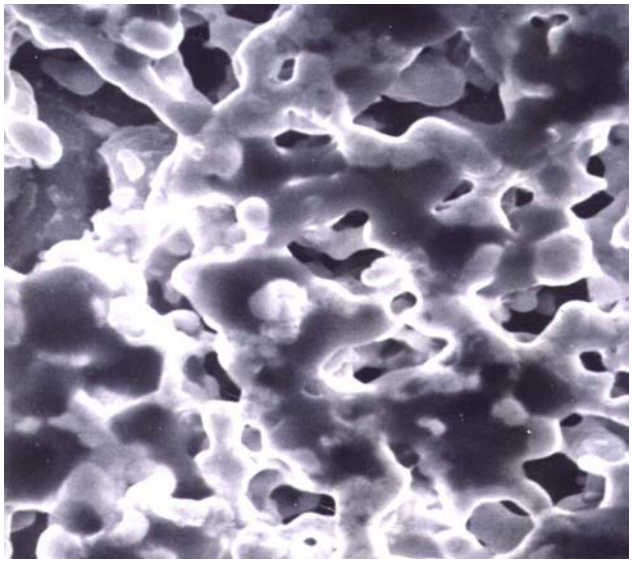

Figure 63. x3500 SEM image of the Pt catalyst screen printed onto a disk membrane.

Catalysts were initially tested in two different forms. The first consisted of a porous platinum film screen printed onto the membrane surface. An SEM image of this type of catalyst film is shown in Figure 63. The image demonstrates that the platinum was completely interconnected and highly porous. This catalyst adhered very firmly to the membrane surface and is well known to have among the highest activity for the target reactions. The problem is that this system is cost prohibitive, and not considered viable for the final product. The second catalyst system consisted of the membrane material powder impregnated with nickel metal. 5 wt.-% Ni catalyst was prepared by impregnating ceramic powder (same composition as the membrane) with nickel nitrate dissolved in acetone. After drying and reductive calcination the catalyst powder was mixed in toluene/ethanol with a binder and a plasticizer and then painted

onto the membrane. The performance of these two types of catalysts is shown in Figure 64. Both membrane samples in the figure were $AB_{0.9}B_{0.1}'O_{3-\delta}$, which was described above. Within experimental variance, both catalysts performed about the same, although Ni was slightly better at lower temperatures and Pt was slightly better at high temperatures.

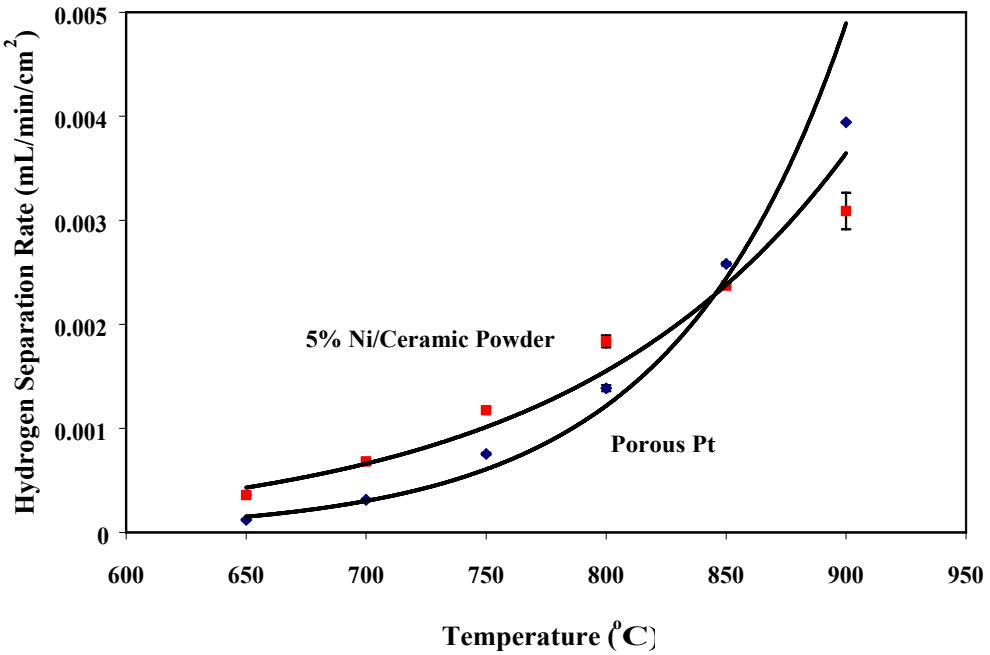

Figure 64. Plot showing hydrogen transport rate versus temperature for two $AB_{0.9}B_{0.1}'O_{3-\delta}$ membranes with different catalysts. The Pt catalyst was a continuous highly porous film applied to the membrane surface. The Ni catalyst was 5 wt.-% on a support powder applied to the membrane surface. Inlet and sweep gas flow rates were 60 mL/min.

In an effort to improve the catalyst layer several different catalysts and application techniques were tested. Ten disks of one composition were prepared for coating experiments. Five disks were polished and five were not. The catalytic metals of interest were Pt, Pd, and Ni. The target loadings were 1% Pt and Pd and 3% Ni.

The precursor compounds chosen were Platinum (II) Acetyl acetonate (Ac-Ac), Palladium (II) Acetylacetonate (Ac-Ac), and Nickel (II) ethyl hexanoate. The Pt and Pd compounds were dissolved in tetra-hydrofuran and the Ni compound was dissolved in n-hexane. The original technique to be employed was to apply (via a pipette) enough solution to completely coat the disks, dry at 60°C, and then calcine at 500°C. This technique was acceptable for the disks to be coated with Ni since the concentration of the solution was quite high (~5% Ni) and therefore high loading was possible with only 3 applications. The solubility of Pt and Pd Ac-Ac was very low causing a low Pt and Pd concentration in solution (<1% Pt or Pd) and made impregnation to high loading impractical.

A solution to this obstacle was found by slurrying the Pt and Pd Ac-Ac in acetone and then applying (via pipette) directly to the disks one side at a time. A thin, uniform, and

controllable coating was possible after drying and calcination at 750°C. There seemed to be no difference in coating the polished from the unpolished disks. However, the coatings were very thin and must be treated gently. The disks did not break upon calcining.

Membrane samples containing a catalyst consistently showed higher hydrogen flux than those without. However, no significant difference was observed as a function of catalyst compositions. As predicted in earlier reports, the reason for this observation likely is that the membranes tested so far have been thick enough (~0.5 to 1 mm) that hydrogen flux likely is mostly limited by transport through the membrane, rather than by surface kinetics. Although the presence of a catalyst did improve transport, the effect of catalyst composition on transport likely will not be apparent until membrane thicknesses are reduced below about 0.1 mm.

These same catalysts were also tested on cermet membranes. The membrane composition used for testing is represented as $AB_{0.8}B^{c}_{0.2}O_{3-\delta}$/44 wt.% metal, and all samples were sanded down and polished to a thickness of 0.78 ± 0.02 mm. Catalysts used for these tests were Pt, Pd, Ni/ceramic slurry, and a porous layer of the cermet material. The Pt catalyst was applied by sputter coating. Pd was applied by dropwise addition of a palladium acetate/acetone solution, followed by drying, and reducing under testing conditions. The Ni/ceramic slurry was prepared by wet impregnating an ABO_3 powder with an aqueous $Ni(NO_3)_2$ solution, followed by drying and reducing under H_2. An alcohol slurry was prepared from the resulting powder and painted onto the membrane surface, followed by drying and curing under testing conditions. The porous cermet catalyst was prepared as a slurry of the membrane powder in solvent with a binder added. The slurry was painted onto the membrane, dried, then cured under testing conditions.

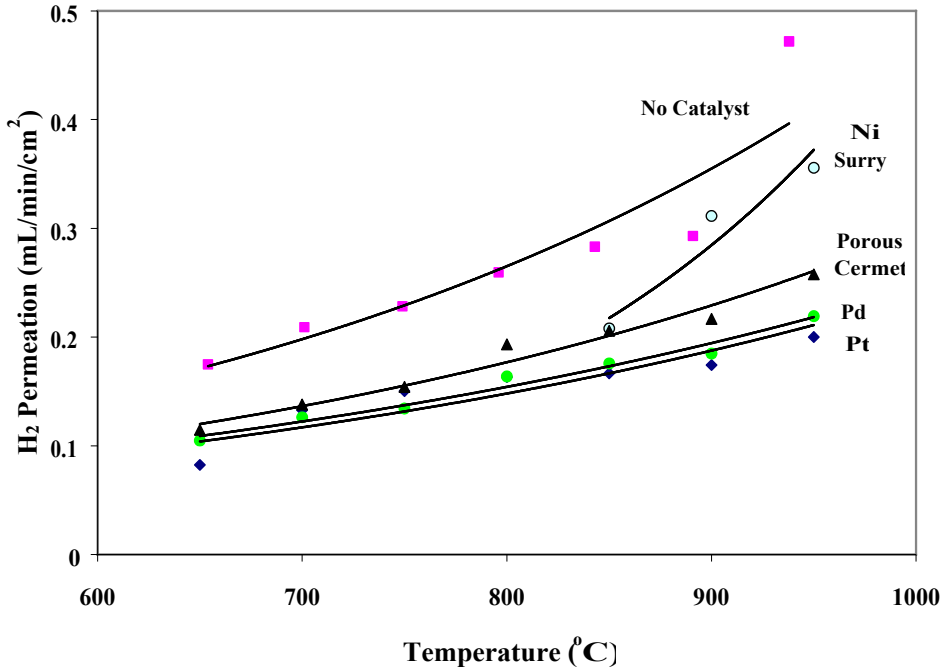

Figure 65. Plot showing H_2 permeation as a function of temperature for 0.8-mm thick cermet membranes with various catalyst coatings.

Results from catalyst testing are summarized in Figure 65. The Pt and Pd catalysts produced almost identical results, and the porous cermet catalyst was only slightly better. The

best results were obtained for the sample with no catalyst added, however, the metal phase of the cermet actually has high catalytic activity for H_2 dissociation. The Ni slurry catalyst performed well at higher temperatures, unfortunately the seal was lost as the temperature was decreased below 850°C. SEM images of the membrane surfaces are shown in Figure 66. The metal phase (dark region) is clearly seen in the image of the bare membrane, and the edges of the metal phase appeared raised slightly above the surface. The Ni/ceramic and porous cermet catalysts looked similar, but the latter appeared to have greater surface roughness. The Pd and Pt catalyst each consisted of discrete metal islands, but the Pt catalyst annealed into very large agglomerates. After testing, the catalyst films appeared the same on the inlet and sweep sides of the membrane, except for the Pt catalyst, which showed much less metal annealing on the sweep side than the H_2 side.

Overall, adding catalysts to the cermet membranes reduced H_2 permeation. For permeation to proceed, H_2 must be dissociated into protons and electrons at the membrane surface, and protons must be transferred into the membrane lattice. Therefore, for this application, catalytic activity anywhere but directly on the membrane surface is not expected to improve permeation. For the Pt catalyst, it is possible that any catalytic benefit at the surface was offset by Pt masking membrane lattice surface sites. Similarly, it is possible that adding a porous cermet layer actually increased the effective membrane thickness. However, this same effect would be expected for the Ni/ceramic catalyst as well. Furthermore, due to high mobility of H_2 in Pd, it was surprising that catalysts suppressed permeation so significantly. Ultimately the catalytic activity of the cermet metal phase intimately mixed with the ceramic produced the best results.

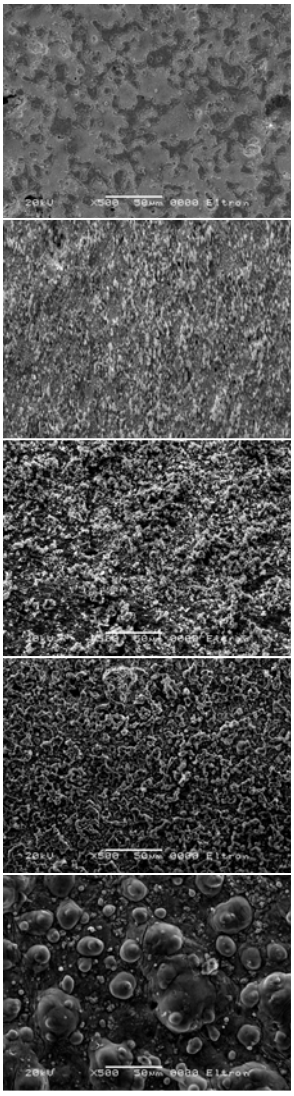

Figure 66. SEM images of catalysts deposited onto cermet membranes. From top to bottom, the images were of a bare cermet, Ni/ceramic, porous cermet, Pd, and Pt catalysts.

To further test catalysts on cermet membranes, SCI used a variety of methods and precursors to apply transition metal and noble metal catalysts, as summarized in Table 5.

Table 5.
Summary of Catalyst Metals Applied to Cermet Membranes by Süd Chemie.

Catalyst Metal	Membrane Wt. Before Catalyst Addition (g)	Membrane Wt. After Catalyst Addition (g)	Catalyst Precursor	Catalyst Loading (wt.%)
Co	0.5567	0.5625	Aqueous	1.03
Ni	0.6127	0.6268	Aqueous	2.25
Ni	0.7554	0.7745	Aqueous	2.47
Pt	0.6563	0.6640	Non-aqueous	1.16
Pt	0.5839	0.5946	Aqueous	1.80
Pd	0.6763	0.6799	Non-aqueous	0.53
Pd	0.5585	0.5636	Aqueous	0.90

SEM images of the membrane surfaces after catalyst application generally indicated that it was difficult to achieve good catalyst dispersion and adhesion on these samples. This result likely was due to the nonporous, high-density nature of these membranes. Observations from the SEM images are as follows:

- For Pd, the aqueous precursor resulted in poor dispersion and clusters of sintered metal about 20 μm in size.
- Both Pt disks yielded very high dispersion, but the sample from the non-aqueous precursor resulted in less sintering on the surface than the aqueous precursor.
- The samples impregnated with Ni showed very large Ni crystallites on the surface (40 μm) and appears to have sintered.

The best catalyst characteristics were achieved for Pt and Pd using non-aqueous precursor solutions, and H_2 transport measurements obtained for these samples are shown in Figure 67. As with previous tests, no significant effect of the catalysts was observed. Both the Pt and Pd coated samples achieved similar H_2 transport rates, and as also shown in the figure, these results were equivalent to a sample with no catalyst. The lack of catalyst influence on permeation likely was due to the use of thick membrane samples, and the fact that cermets already contain a catalytic metal.

In an effort to obtain quantitative data on catalyst performance without limitations due to membrane thickness, potential catalyst were evaluated by performing temperature-programmed reduction (TPR) measurements on catalyst-impregnated membrane precursor powders. Membrane materials in powder form were catalyzed with the same metals that were impregnated on the surfaces of previous membrane disks. TPR experiments exposed the powder to a stream of 5% H_2 in argon while the temperature was increased at a constant rate. A very sensitive thermal conductivity detector measured the changes brought about by this reduction and thereby provided a measurement of reduction or, in effect, hydrogen adsorption.

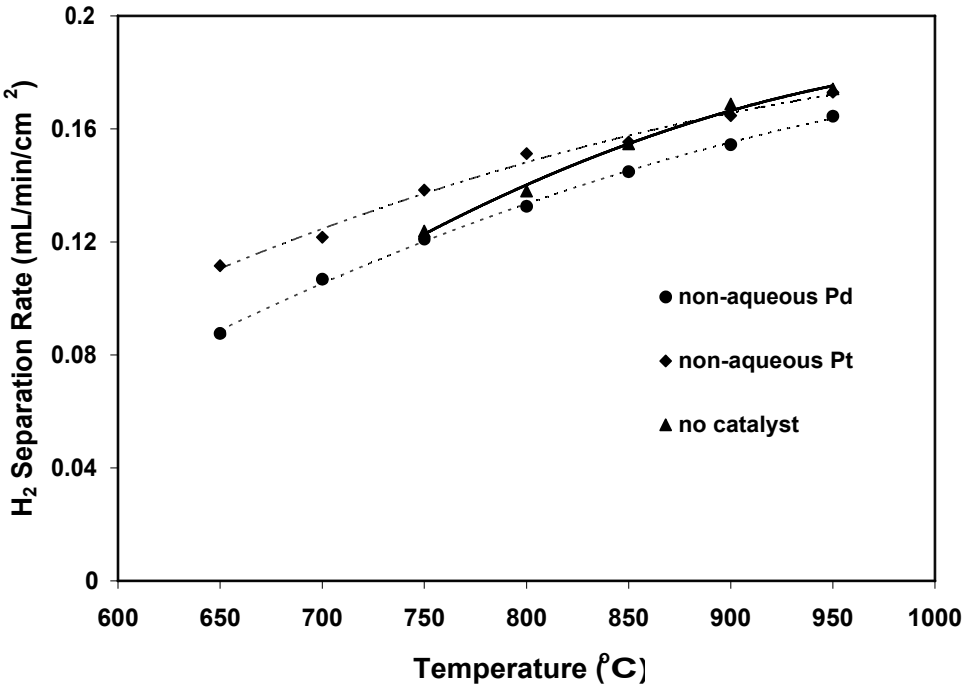

Figure 67. Plot showing H_2 permeation as a function of temperature for perovskite/metal cermet membranes with and without catalyst on the membrane surface. The feed gas was humidified 80/20 wt.% H_2/He and the sweep gas was Ar. The gas flow rates were between 80 and 120 mL/min.

Pt, Pd, and Pt/Pd greatly increased the adsorption of H_2 relative to the unmodified powder precursors. Both Ni and Cr increased H_2 adsorption, but not to the same extent as the precious metals. Test results from the actual membranes catalyzed with these metals will validate the use of TPR as a tool for measuring the effectiveness of metals added to increase the rate of H_2 adsorption. Figure 68 shows the TPR data for precursor powders of the ceramic $AB_{0.8}B^c_{0.2}O_{3-\delta}$ and the corresponding cermet $AB_{0.8}B^c_{0.2}O_{3-\delta}$/44 wt.% Metal-1 without any added catalyst. The effect of the metal phase was apparent by a dramatic increase in the H_2 uptake and a sharp peak centered at 212°C. Samples of these powders were impregnated with Pt, Pd, Cr, and Ni and the TPR results are summarized in Table 6.

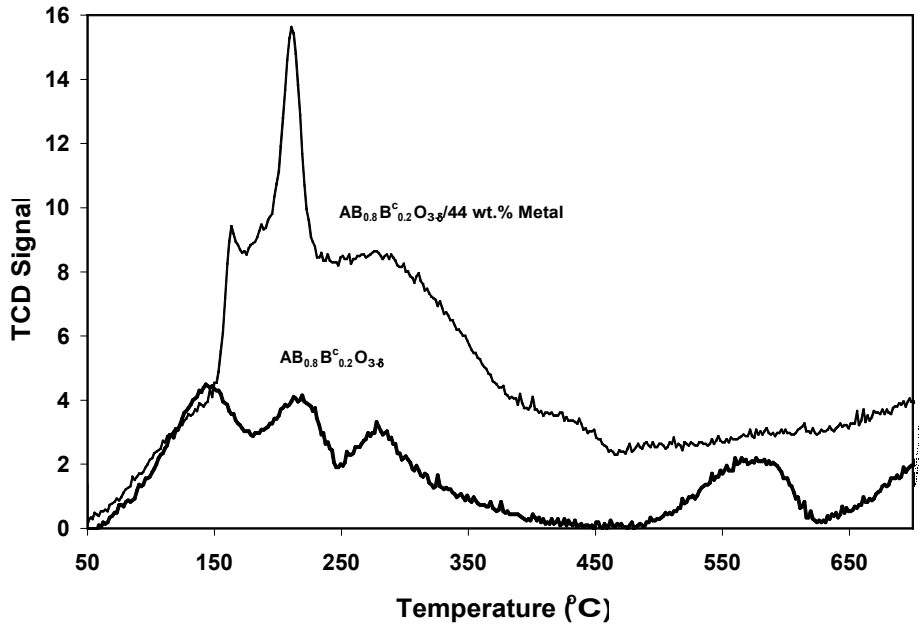

Figure 68. TPR results for ceramic and cermet membrane precursor powders without catalyst.

Table 6.
H_2 Uptake Calculations Based on TPR Results for Selected Membrane Materials and Catalysts.

Sample	Catalyst	H_2 Uptake (μmol/g)	Percent Change from Bare Material
$AB_{0.8}B^c_{0.2}O_{3-\delta}$	None	213.9	-
$AB_{0.8}B^c_{0.2}O_{3-\delta}$	0.25 wt. % Pt	200.7	-6.2
$AB_{0.8}B^c_{0.2}O_{3-\delta}$	0.25 wt. % Pd	254.3	18.9
$AB_{0.8}B^c_{0.2}O_{3-\delta}$	0.25 wt. % Cr	423.5	98
$AB_{0.8}B^c_{0.2}O_{3-\delta}$	0.25 wt. % Ni	573.2	168
$AB_{0.8}B^c_{0.2}O_{3-\delta}$	0.25 wt. % Pt (chloride precursor)	900.4	321
$AB_{0.8}B^c_{0.2}O_{3-\delta}$	0.25 wt. % Pd (chloride precursor)	2248	951
$AB_{0.8}B^c_{0.2}O_{3-\delta}$ / 44 $^w/_0$ Metal-1	None	538.8	-
$AB_{0.8}B^c_{0.2}O_{3-\delta}$ / 44 $^w/_0$ Metal-1	0.25 wt. % Pd	5070	841

Initially, addition of Pt had little effect on H_2 uptake relative to the catalyst-free powder, and Pd only increased uptake slightly. More significant gains were achieved using Cr and Ni catalysts, which increased uptake by 98 and 168%, respectively. However, when Cl-based precursors were used, H_2 uptake increased more than three-fold for Pt and nearly and order of magnitude for Pd. The sample impregnated with 0.25 wt.% Pd using the chloride precursor absorbed 2248 μmol of

H_2 per gram of catalysts, corresponding to a 951% increase relative to the catalyst-free powder. The catalyst-free cermet had a very high H_2 uptake of 538.8 µg/mol, which partly explains the relatively high H_2 flux with this material. Moreover, addition of 0.25 wt.% Pd to this sample resulted in the highest H_2 uptake of 5070 µmol/g.

These temperature programmed reduction experiments were carried out by increasing temperature while the catalyst is exposed to 5%H_2 in Ar at a set rate, and measuring the change in thermal conductivity of the resultant off gas. This sort of experiment is not possible if trying to study the behavior of the material at higher temperatures. Therefore, work was concentrated on conducting pulsed reduction experiments at high temperature since many of the membrane compositions under development operate near 800°C. An experimental procedure was devised so that the membrane material would be kept under an inert atmosphere (Ar) and heated to 800°C. When at temperature, 1 mL of 5% H_2 in Ar was pulsed over the powder. This process was repeated 30 times and the resulting signal change was monitored relative to an empty tube.

Three different powder samples were subjected to the pulse experiment and the results are shown in Figure 69. Results from the empty tube (null run) yielded an integrated peak area of approximately 9,000. The first sample was a proton conducting perovskite represented as $AB_{0.8}B_{0.2}{}^{c}O_{3-\delta}$ (Sample A). For the first 8 pulses, this material adsorbed hydrogen in decreasing quantities. After the sixth pulse the material began to adsorb increasing quantities of H_2. From the ninth pulse to the 22nd pulse, all hydrogen pulsed was adsorbed by the material yielding virtually no peak. Then from the 22nd pulse on, H_2 adsorption decreased. The trend indicates that further pulses will most probably result in decreasing adsorption until the peak area approaches that of a null tube (hydrogen saturation of the material).

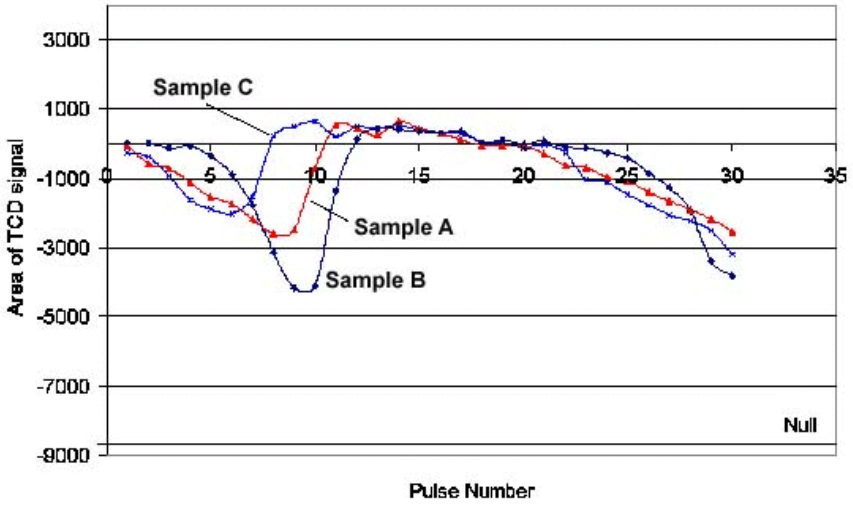

Figure 69. Pulsed H_2 adsorption results at 800°C for two batches of powdered $AB_{0.8}B_{0.2}{}^{c}O_{3-\delta}$ (Samples A and C) and Sample A with 25% Pd.

The experiment was repeated with the same material impregnated with 0.25% Pd (Sample B). The trends were identical but the amplitude of the initial "non-adsorption" was greater than that of the unimpregnated material. The experiment was conducted a third time on a newer batch of $AB_{0.8}B_{0.2}{}^{c}O_{3-\delta}$ (Sample C). The results mirrored those of the original sample except that the increase in adsorption occurred at pulse seven.

Although the mechanism for the H_2 adsorption dependence on pulse is unclear, both samples without Pd absorbed significant quantities of H_2 at 800°C and addition of Pd increased high-temperature H_2 adsorption.

A new experimental procedure was developed for testing catalysts materials with potential for hydrogen separation membranes. Catalyst activity was measured using a low-pressure environment (sub atmospheric pressures) in a closed chamber and partial pressures (and total pressure) changes over time were monitored using RGA and pressure gauges. The experimental apparatus is shown schematically in Figure 70. This set-up allowed testing potential hydrogen catalyst candidates by measuring the exchange between H_2 and deuterium. In this way, deuterium and hydrogen mixtures were used to monitor formation of D–H species. The apparatus consists of a flow reactor equipped with a turbo pump (Turbo pump (Edwards Model ETP 100) and a mechanical pump (Edwards Model E2V8). The flow rates of the gases are controlled using two mass flow controllers (Horiba STEC Model SEC 4400, Max. Flow rate = 100 sccm). The setup includes a substrate heater (GE HTR1001 Boron Nitride heater, max. temperature 900°C). The temperature of the catalyst sample is measured using a K-type thermocouple, capable of measuring temperature up to 980°C. The pressure inside the chamber is monitored and controlled using a pressure transducer (MKS Baratron Model 629, capable of measuring up to 1 mTorr) in conjunction with a pressure control valve. In addition, it is also equipped with a residual gas analyzer (RGA, Kurt Lesker Co.) capable of detecting the composition of the gases in the gas phase from pressures 10^{-6} Torr to as low as 10^{-11} Torr. The entire setup is enclosed in a chamber for cooling purposes and to test the samples at low temperatures. Thermal conductivity detectors (GOW-MAC Model 10-077 WX), capable of detecting up to 200 ppm of H_2 in deuterium, will be installed shortly in the setup for further testing of the performance of the catalyst.

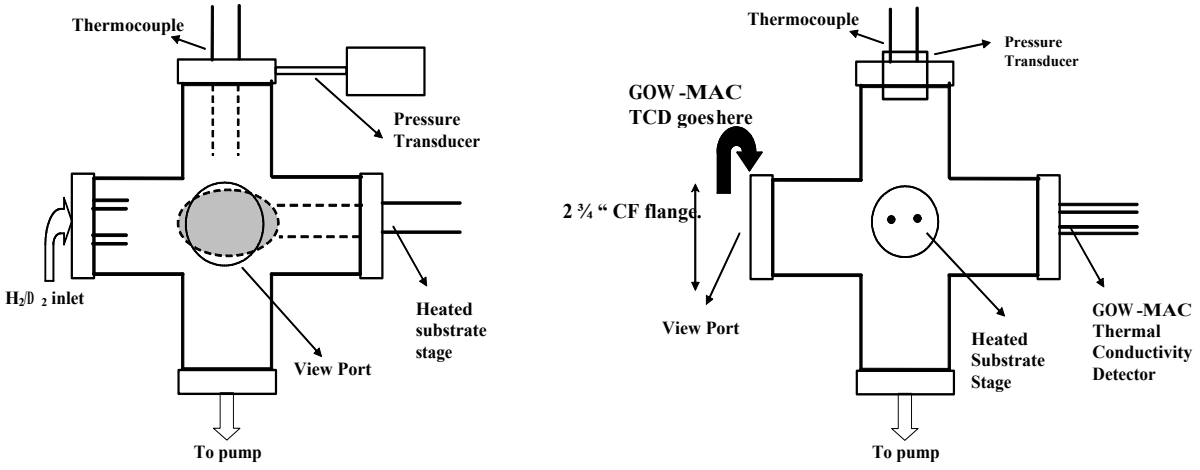

Figure 70. Schematic diagram of the apparatus used for catalyst evaluation. The figure on the left is a front view, and the figure on the right is a side view.

Four catalysts were tested in the setup described above. The catalyst samples were made by impregnating high surface area alumina with metal catalyst precursor solutions. The samples were placed on the substrate heater and heated to various temperatures while the gas phase

composition was monitored using the RGA. A feed gas consisting of 20 sccm of H_2 and 50 sccm of deuterium was used for the present experiments. The testing was performed at three different temperatures: 25°C, 140°C, and 240°C. The pressure in the reactor under these conditions was approximately 490 mTorr. All the samples were tested under identical conditions for the purpose of comparing their performance. The scans were repeated three times for each temperature and for each catalyst to verify the consistency of the results.

Preliminary data indicated that the RGA unit was capable of resolving HD from H_2 and D_2. Experiments were repeated three times for each temperature and for each catalyst to verify the consistency of the results. Though hydrogen inflow was only 20 sccm compared to 50 sccm deuterium, the output showed more hydrogen for all catalysts tested, indicating a preferential adsorption of deuterium. Adsorption of H_2 on copper catalyst decreased above 140°C. For the other catalysts tested hydrogen adsorption increased at higher temperatures. Binary catalysts were included in these tests. At both 25 and 140°C, a selected new catalyst composition produced greater H_2/D_2 exchange than the base-case Pd catalyst.

Up to this point in the project the same catalyst has been used on both sides of the membrane for rapid screening. However, two different types of catalysts are needed for hydrogen separation membranes. The catalyst on the membrane surface exposed to the feed stream functions as a hydrogen dissociation catalyst. It must be stable to sulfur, steam, and CO_2. On the permeate side of the membrane, the catalyst coating promotes hydrogen desorption. SCI therefore narrowed the focus of their catalyst development towards development of sulfur tolerant catalysts for the retentate side of the membrane. Palladium copper alloys have been discussed in the literature as sulfur tolerant alloys. Two Pd/Cu alloy samples were prepared using palladium nitrate and copper nitrate solutions. The preparation method involved two stages: (a) first the solution mixture was heated in air at 350°C for about two hours and (b) hydrogen treatment (reduction) of the resulting solid in a vacuum chamber at 500°C for about two hours. The resulting solid was analyzed for phase, composition and morphology using EDAX and SEM.

SEM images are shown in Figure 71. As shown in Figure 71a, the backscattered imaging does not show any difference between copper and palladium. This implies that there is an even mixture of both copper and palladium at the atomic level, which makes it difficult for the backscattering imaging to detect the difference between palladium and copper. This shows the formation of a Pd/Cu alloy. To confirm the presence of Cu/Pd after hydrogen treatment, EDAX analysis was performed on the same powder. As shown in Figure 72, there is a large presence of palladium along with copper.

Theoretical calculations were performed to determine the energy of sulfide formation on several potential metal catalyst surfaces under the expected temperature range of 320-440^{o}C. Calculations were performed for metals exposed to 10, 100, and 1000 ppm H_2S. Results showed that unalloyed iridium possessed the highest tolerance to sulfur without bulk sulfide formation. Calculations showed that the other unalloyed metals including Pd, Cu, Pt, Ru, Rh, and Ga all formed one or more stable bulk sulfides in the presence of H_2S in concentrations as low as 10 ppm. Several different catalysts were prepared and tested for sulfur resistance in hydrogen containing feed streams. Membranes were exposed to 5-30 ppm H_2S and the permeability compared to equivalent membranes not exposed to H_2S. Results showed that palladium copper alloy catalysts were more sulfur tolerant than pure palladium catalysts. Energy Dispersive X-ray Analysis, XPS, and X-ray diffraction were used to confirm the presence of sulfur on membrane surfaces following testing.

A

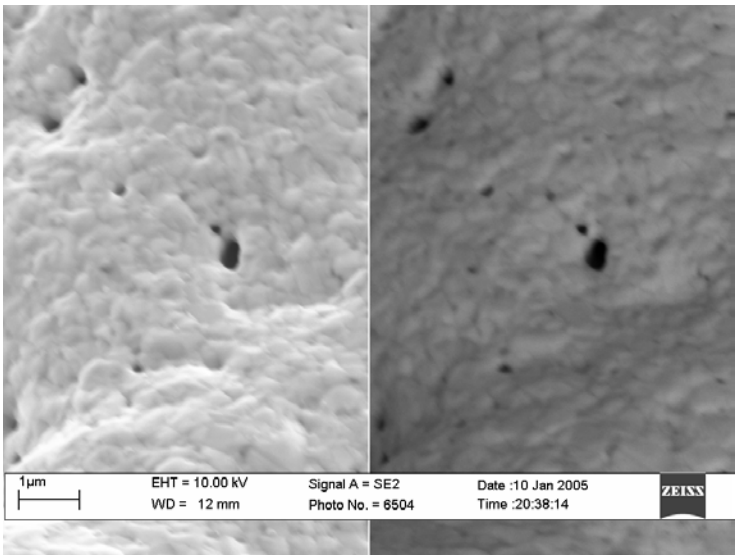

B

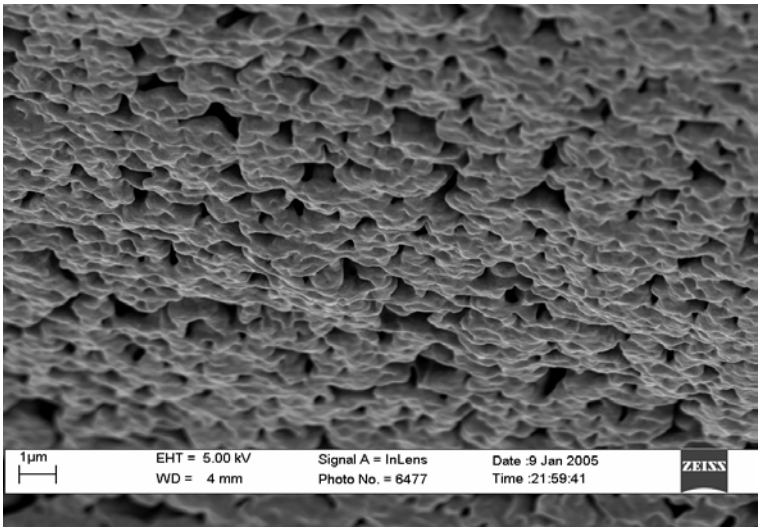

Figure 71. SEM images showing Pd/Cu alloy. Image (A) shows the secondary electron image on the left and the backscattered image on the right. This image shows an even mixture of copper and palladium Image (B) shows more palladium particles, along with the presence of copper.

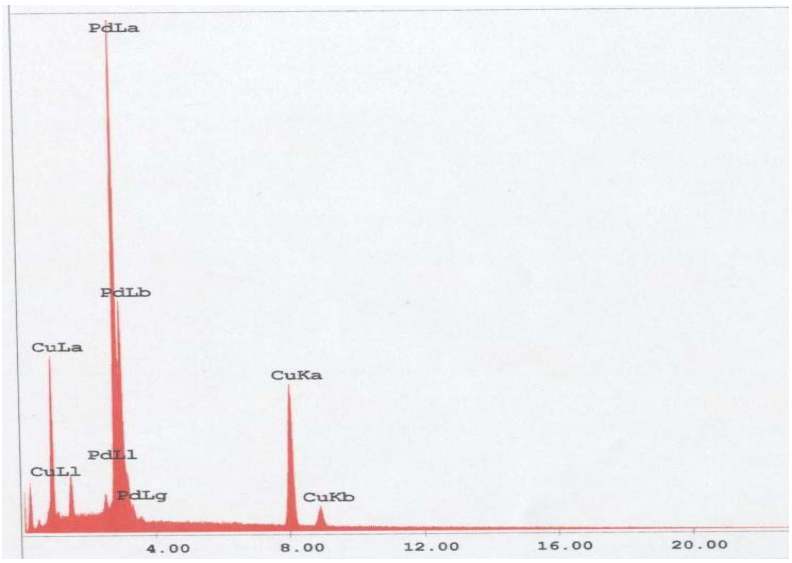

Figure 72. EDAX analysis of the resulting Pd/Cu alloy prepared from initial solution mixture containing Pd nitrate and Cu nitrate solutions.

G. Membrane Stability in Reactive Gases

1. Potential Contaminants (MTI)

Typically in coal gasification the primary products are H_2 and CO comprising roughly 70% of the syngas at actual amounts and a ratio that varies with the coal and the gasifier conditions. The balance is usually highest in water vapor and CO_2 with methane present in amounts that again depend upon the gasifier conditions. The syngas produced in coal-gasification can also be expected to contain varied amounts of a large number of minor constituents. The project team will have to identify the level of tolerance the hydrogen separation system has to each of these constituents in order to define process conditions for the reactor and any changes required for the process flow diagram. The two most obvious syngas components that could be of potential concern are particulate matter and sulfur. As mentioned above, typical gasification plants provide particulate removal and some level of sulfur control. The issue becomes how well the hydrogen separation system fits within these typical control schemes and any concerns related to the trace constituents that are typically present.

The particulate control systems for gasifiers are already being pushed toward operation as high in temperature as is feasible in order to maximize the overall process efficiency. There are many different technologies for >99.99% removal of particulate matter from flue gases. The one that seems to get the most attention for coal gasification is high temperature and pressure candle filter systems. These systems are targeting removal at temperatures up to about 850°C. Therefore, with these targets in mind it is reasonable to assume that particulate free syngas will be available to the membrane reactor at temperatures as high as 850°C without any additional processing. However, as mentioned above, most of the testing has been performed at lower temperatures to allow removal of the alkali and to reduce the severity of conditions seen by the particulate control equipment.

The next step is to determine if expected sulfur concentrations pose any concerns for the hydrogen separation system. The sulfur from the gasifier is primarily in the form of H_2S, with some COS and trace amounts of CS_2, thiophenes, and mercaptans (Understanding Coal Gasification, Alice Kristiansen, IEA Coal Research, March 1996). Calcium based sorbents can be used to remove 80 to 90% of the H_2S upstream of the particulate removal. The final sulfur concentration depends in large part on the coal being utilized and the performance of gasifier sulfur removal, but the syngas could be expected to contain a few hundred PPM of H_2S. Input is needed from testing to determine what sulfur levels are acceptable for the membrane.

If sulfur reduction to levels around 10's of PPM or lower are required, similar to the requirements of shift catalysts, then a final sulfur removal system will be required. Most of these are liquid absorbers that also remove CO_2 (Berkowitz, N., An Introduction to Coal Technology, Academic Press, Inc., New York, 1979). These systems typically operate at low temperatures in order to increase the H_2S solubility. For applications where polishing only small amounts of sulfur is required, a zinc oxide bed is a possibility, and they typically operate at around 400°C to optimize the capture of organic sulfur compounds and the bed capacity. If any of these systems were required, a reheat system would be needed upstream of the hydrogen separator. However, high efficiency hot desulfurization is in the early stages of commercialization, and may prove to be a match for implementing the hydrogen separation system in a Vision 21 power plant. Again the sulfur removal requirements, if any, need to be determined through evaluation of the hydrogen transport membranes.

Coal can vary greatly in the amount and composition of mineral matter. Selected coals presented in "Steam" contain between 5 and 69% ash on a dry basis (Steam, It's Generation and Use, 40th ed., Babcock & Wilcox, a McDermott Company, Stultz, S.C., and Kitto, J.B., 1992). The major components that are analyzed for in ash analyses are provided in Table 7 along with the ranges of values shown for ten U.S. coals.

Table 7.
Reported Ash Analysis Results for Ten U.S. Coals.

Species (as oxide)	Low Value (for Ten U.S. Coals)	High Value (for Ten U.S. Coals)
SiO_2	23.32	66.85
Al_2O_3	10.0	34.0
Fe_2O_3	1.18	19.0
TiO_2	0.4	1.57
CaO	0.6	22.0
Mgo	0.3	5.0
Na_2O	0.39	7.41
K_2O	0.27	2.65
P_2O_5	Unmeasured	0.99
SO_3	0.99	20.85

These values are reported as oxides and can be present in numerous forms in the utility system. Also, the reducing conditions in the gasifier and the downstream processes can impact the fate of these ash constituents. In addition to the presence of these components in the coal ash, furnace refractory is typically high in silica and alumina. As with the ash components,

depending on the conditions and the temperature and efficiency of downstream particulate control, various forms of these species can potentially reach the hydrogen separation reactor.

The alkali components of the coal can promote corrosion and act as fluxing agents at high temperatures. Removal of alkali is performed upstream of the gas turbine to eliminate these concerns. This is typically performed by absorbing the alkali components (especially sodium) at temperatures below 1400°F (760°C) and lower. Alkali species can be expected to be present in the gas fed to the separation membrane in concentrations that will vary with the coal, the syngas temperature, and upstream processing.

In addition to the major components found in coal ash there are numerous trace elements. Many of these have been evaluated in more detail lately in light of questions over the potential environmental impact of these trace elements from coal fired power plants. Trace elements evaluated by MTI included antimony, arsenic, barium, beryllium, cadmium, chromium, cobalt, lead, manganese, mercury, nickel, and selenium (Madden, D.A., Holmes, M. J., AECDP Data Library, McDermott Technology, Inc., http://www.mtiresearch.com/aecdp.html, 1998). Concentrations of these species are typically very low in coal. For one selected coal analyzed by MTI, all of these species were at concentrations less than 20 ppm in the coal. In addition, flue gas measurements showed that over 95% of flue gas concentrations were captured with the particulate for all of these constituents except for arsenic, selenium, and mercury. Removals in the particulate control devices was above 80% for arsenic, greater than 50% for selenium, and can be as low as single digit percentages of capture for mercury. These results are from a composite sample of an eastern bituminous coal and could be expected to vary greatly as a result of the coal and operating conditions of the firing system and of the particulate control device. Additional information can be gathered for any of these components that are determined to pose specific concerns for operation of the separation membrane.

Also present in higher concentrations are several acid gases. The most commonly measured of these are hydrogen chloride and hydrogen fluoride. The concentrations of chlorides and fluorides were measured for the same coal as described above in reference to trace elements. The results indicated a chloride concentration slightly above 1000 ppm and a fluoride concentration of about 35 ppm. These components also vary widely with the coal. Western coals are typically much lower in chloride and eastern coals can be either higher or lower in chloride than the coal selected. The fate of all of these components will depend on both the gasifier operation and the coal composition. Compared to a combustion system a gasifier will typically capture more of the inorganics within the firing system, but if particulate control is performed at higher flue gas temperatures less of the species with higher volatilities may be removed.

2. Sulfur Membrane Testing – Eltron

Candidate ceramic membrane compositions were placed in a cell under flowing H_2S (1000 ppmv/bal. N_2) at 950°C for 72 hours, and XRD patterns before and after exposure were used to determine the extent of reaction. All compositions tested clearly demonstrated reaction with H_2S, although the original perovskite diffraction pattern remained as well. Compositions of the form $AB_{0.8}B'_{0.2}O_{3-\delta}$, where B′ is one of seven transitions metals, generally showed formation of the sulfide of the A-site cation, AS, and the B-site oxide, BO_2. Oxides of the B′ dopant also were observed in some cases, $B'O_x$, or oxides of the form $AB'O_3$. Two different compositions of the form $AB_{1-x}B'_xO_{3-\delta}$, where $0.05 \leq x \leq 0.8$, also were tested with similar results. Finally,

cermets of the form $AB_{0.8}B^{c}_{0.2}O_{3-\delta}$/44 wt.% metal also were tested. The effects of H_2S were not as obvious, however, peaks associated with sulfides of the A-site cation and the metal phase were clearly present.

Intermediate temperature composite layered membranes were also tested for tolerance to sulfur. Layered composite membranes containing the baseline catalyst were tested in four different ambient pressure reactors. The average permeation measured at 420°C was 21(2) $mL \bullet min^{-1} \bullet cm^{-2}$. Sulfur tolerance of the baseline catalyst was determined by introducing hydrogen sulfide into the feed stream. A sample membrane was heated to 420°C and exposed to a hydrogen / helium feedstream. Three to four data points were taken at three hour intervals to establish an initial permeation. Hydrogen sulfide was then introduced into the feed stream to produce a H_2S concentration of 8 ppm. Permeation data was collected at 10 minute intervals for one hour to measure the rate of degradation. Additional data points were then taken at three hour intervals. Results showed that layered composite membranes containing the baseline catalyst degraded rapidly in the presence of 8 ppm H_2S. Within 20 minutes of exposure to H_2S, permeation decreased 30–40%, and after two hours permeation had dropped to 50% of each membrane's original permeation value.

3. Carbon Monoxide Membrane Testing - Eltron

Candidate membrane compositions for these tests had the general compositions $AB_{0.9}B^{a}_{0.1}O_{3-\delta}$, $AB_{0.8}B^{b}_{0.2}O_{3-\delta}$, and $AB_{0.8}B^{c}_{0.2}O_{3-\delta}$/44 wt.% metal. Sintered membrane pellet samples were placed in a cell and heated to 950°C under flowing Ar. Once this test temperature was reached, the Ar flow was replaced with UHP CO (99.999%) for 48 hours. Upon completion of the test, the gas flow was switched back to Ar, and the cell was cooled to room temperature. After testing, the $AB_{0.9}B^{a}_{0.1}O_{3-\delta}$ and $AB_{0.8}B^{b}_{0.2}O_{3-\delta}$ membranes showed a slight discoloration, and the $AB_{0.8}B^{b}_{0.2}O_{3-\delta}$ membrane also cracked around the edges. XRD patterns of these two membrane surfaces after CO exposure indicated some ACO_3 formation, but the predominant pattern remained the ABO_3 perovskite. The $AB_{0.8}B^{c}_{0.2}O_{3-\delta}$/44 wt.% metal membrane showed no evidence of carbonate formation; however, a thick layer of graphitic carbon was formed on the surface. This effect likely was due to the metal phase, and should be minimized under less extreme conditions using a humidified gas stream.

4. Carbon Dioxide Membrane Testing - ORNL

Hydrogen separation membranes in Vision 21 energy plants will be continuously exposed to several vol.% CO_2 under normal operating conditions. It is well known that perovskite materials can react with CO_2, thus it is important to identify the conditions where this reactivity becomes problematic, and determine if stability can be improved by relatively minor adjustments in membrane composition.

A range of perovskite ceramic powders with the general composition $A_xB_{0.8}B'_{0.2}O_{3-\delta}$, $0.90 \leq x \leq 1.0$ were prepared to test the dependence of A-site deficiency on perovskite stability in CO_2. The powders were placed in a high-temperature XRD instrument, sealed, and raised to 1200°C in air or helium. XRD patterns confirmed a single-phase perovskite structure for the powders, then the gas flow was switched to 1 atm CO_2. XRD patterns then were obtained every 5 minutes after lowering the temperature in 50°C increments. Peaks associated with the A-site carbonate, *i.e.*, ACO_3, were observed for $AB_{0.8}B'_{0.2}O_{3-\delta}$ (no A-site deficiency) once the

temperature was lowered to approximately 1120°C. However, the A-site deficient compositions resisted carbonate formation until ≤ 1060°C. This measurable difference, though modest, indicated that a A-site deficiency could be accommodated and improved the stability of the phase. The stability of $A_{0.98}B_{0.8}B'_{0.2}O_{3-\delta}$ against CO_2 was further improved by selectively doping the B-site. This modified composition remained a single-phase perovskite at temperatures ≥ 900°C.

The above stability tests were performed under a "worst-case-scenario": high surface area powder was subjected to pure, flowing CO_2. In actual application, the material is a dense body subjected to conditions with a much lower partial pressure of CO_2. Further stability studies will be done under more representative conditions, including behavior in moisture-containing gas.

H. Membrane Corrosion Testing - CoorsTek

Resistance to corrosion from water was measured for selected ceramic and cermet compositions by boiling samples in deionized water for two hours and measuring the sample weight loss. This simple test represents a worst-case evaluation of resistance to degradation from moisture. Furthermore, hydroxide formation of constituents in these materials loosely parallels carbonate formation, so this test provides a quick and general evaluation of overall membrane stability. Results are summarized in Table 8.

Table 8.
Weight Loss for Selected Membrane Samples after Boiling in Water for 2 Hours.

Composition	Initial Weight (g)	Final Weight (g)	Weight Loss (%)
$AB_{0.8}B^{c}_{0.2}O_{3-\delta}$	1.8357	0.5316	71.0
$AB_{0.8}B^{c}_{0.2}O_{3-\delta}$ / 44 wt.% Metal-1	1.9188	1.6116	16.0
$AB_{0.8}B^{d}_{0.2}O_{3-\delta}$ / 44 wt.% Metal-1	1.9032	1.5759	17.2
$AB_{0.8}B^{c}_{0.2}O_{3-\delta}$ / CER1	1.8962	1.8917	0.27
$AB_{0.8}B^{c}_{0.2}O_{3-\delta}$ / CER2	1.8977	1.8977	0.00

The sample with the worst corrosion resistance was the pure ceramic $AB_{0.8}B^{c}_{0.2}O_{3-\delta}$. The cermet analogs also showed substantial corrosion, however, the weight loss was not as has high as expected based on corrosion for the ceramic. This result indicated that the metal phase had a slight stabilizing effect on the ceramic. The $AB_{0.8}B^{c}_{0.2}O_{3-\delta}$/CER1 sample was very stable and demonstrated only a 0.24-% weight loss, and the $AB_{0.8}B^{c}_{0.2}O_{3-\delta}$/CER2 demonstrated no weight loss. Based on these results, addition of a stabilizing ceramic phase appears to be a viable approach for improving the performance of H_2 permeable materials using proton-conducting ceramics.

I. Mechanical Testing – ORNL, CoorsTek

At ORNL a range of candidate proton conducting ceramics were tested for mechanical properties. Strength was measured using biaxial flexure (ball-on-ring or ring-on-ring configurations) since this method accommodated the sintered disk specimens generated in the processing trials. Strength was measured as a function of temperature and stressing rate in an air

environment. Samples demonstrated an average strength of 136 MPa and a Weibull modulus of 8.5. Dry machining of the sample surface reduced strength to 64 MPa, but increased the Weibull modulus to 14.3. This result suggested that the machining process could be used to improve device reliability with only a minor compromise in material strength. Sample failure typically was due to processing induced voids or hard agglomerates.

At CoorsTek mechanical tests were performed on model proton-conducting ceramics and cermets to establish a baseline for mechanical properties and assess the effect of adding a metal phase on material strength. Table 9 presents a summary of four-point bend flexural strength and Weibull modulus measurements for the ceramic $AB_{0.8}B^{c}_{0.2}O_{3-\delta}$ and the corresponding cermet $AB_{0.8}B^{c}_{0.2}O_{3-\delta}$/40 wt.% Metal-1.

Table 9.
Summary of Mechanical Testing of Model Ceramic and Cermet Materials.

Test	Composition	Microbars (2 mm x 1.5 mm)	Minibars (4 mm x 3 mm)
4-Pt. Bend Flexural Strength (MPa)	$AB_{0.8}B^{c}_{0.2}O_{3-\delta}$	72.4	67.7
4-Pt. Bend Flexural Strength (MPa)	$AB_{0.8}B^{c}_{0.2}O_{3-\delta}$ / Metal-1	153	149
Weibull Modulus	$AB_{0.8}B^{c}_{0.2}O_{3-\delta}$	14.0	N/A*
Weibull Modulus	$AB_{0.8}B^{c}_{0.2}O_{3-\delta}$ / Metal-1	20.4	15

* Not calculated due to small number of samples.
For the ceramic, eight microbars and four minibars were tested. For the cermet, 20 microbars and 10 minibars were tested.

These results indicated that addition of the metal phase significantly increased material strength and improved the Weibull Modulus (a measurement of the flaw distribution within the material). Considering the much higher H_2 permeation of cermets relative to ceramics, these results were very encouraging.

II. Task 3 High-Pressure Hydrogen Separation

Contributors: Eltron

Two high pressure hydrogen separation units were constructed for membrane evaluation. A schematic diagram of the design is shown in Figure 73 and a photograph is shown in Figure 74. Support hardware consists of devices for gas supply and mixing, plus analytical instruments to monitor products. The nitrogen supply system performs four functions. First, nitrogen is used to pressurize the separation vessel and dilute the syngas feedstream. Second, the space between the vessel liner and the vessel wall is purged with nitrogen to prevent interaction of carbon monoxide with Haynes 230 alloy at elevated temperatures. Third, nitrogen is used as the sweep gas to remove hydrogen transported through the ceramic membrane. Fourth, nitrogen is used to load the back pressure regulator. The supply manifold for nitrogen consists of two or more 6000-psig tanks, CGAs fitted with flow restrictors, check valves, shutoff valves, and a vent valve. From the manifold, the gas flows through a filter to a regulator where the pressure is

reduced to near operational pressure. A 450-psig relief valve protects the down stream equipment, and a gas line to the second gas separator vessel exits at this point. After the check valve, a line from the nitrogen system exits to the back pressure regulator control. The nitrogen line then divides into high- and low-pressure supplies. The high-pressure nitrogen supply is filtered and has a regulator to adjust the operational pressure. The high-pressure line splits again into a gas feed for inside the vessel, and for the purge gas between the liner and the vessel wall. Both lines have mass flow controllers to set flow rates. Check valves and shutoff valves finish the nitrogen feed system. Similarly, the low-pressure line has a mass flow controller to set sweep gas rates, and runs directly to the sweep gas port at the base of the pressure vessel.

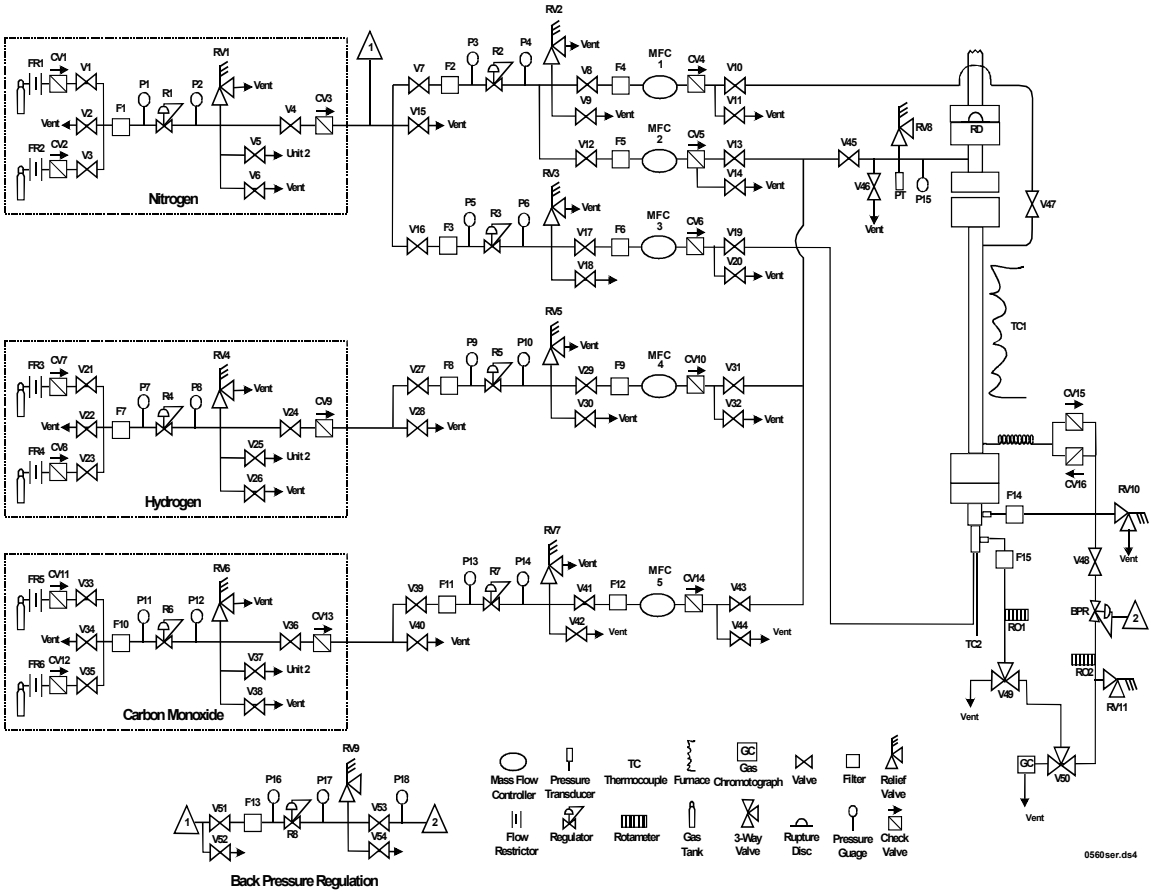

Figure 73. Schematic diagram of the apparatus for evaluation of hydrogen separation membranes at high pressure.

Figure 74. Photograph of the apparatus for evaluation of hydrogen separation membranes at high pressure.

The hydrogen and carbon dioxide systems are similar to the nitrogen systems but have a single feed line per gas separator. Regulators set pressure at the manifold and feed line. Mass flow controllers set flow rates. Check valves prevent back flow, and are available to isolate sections of the system. Filters are used to prevent clogging of the regulators and mass flow controllers. Nitrogen for the vessel gas feed joins with hydrogen and carbon dioxide in a single line to the separator vessel. A vent valve and relief valve are close to the vessel to protect the vessel from over pressure. A pressure transducer and a pressure gauge are used to monitor vessel pressure.

There are three exit gas lines from the separator vessel; the feed gas out, the purge gas out, and the sweep gas out. The sweep gas passes through a filter and a rotameter before routing to a gas chromatograph for analysis. The purge gas out passes through a filter and a coil with a double check-valve setup before connecting to the feed gas out. The coil and check-valves allow the pressure to equilibrate on both sides of the liner without excess back-flow of feed gas into the purge system. The feed gas out passes through a filter and join the purge gas prior to being reduced in pressure at a back pressure regulator. The gas then passes through a rotameter and to the gas chromatograph for analysis. The back pressure regulator control panel consists of a nitrogen pressure line and a regulator to set the dome load on the back pressure regulator. The line is filtered and protected with a relief valve and vents.

A schematic diagram of the high-pressure hydrogen separation vessel is shown in Figure 75. The central tube of the vessel (#12) is constructed from oxidation resistant Haynes 230 alloy, and the majority of the other components are made from 316 stainless steel. A bolted rupture disc holder (#1 and #2) with a 1" scored Inconel rupture disc (#3) is located at the top of the vessel. The holder connects to a flange (#8) with a 1-inch I.D. tube entry line for the feed gas (#6 and #7). An alumina liner (#27) is held in the flange with double Viton O-rings (#10). The flange (#8) is bolted to a partner flange (#9) with a spiral wound gasket (#29) between the two. This second flange is welded to the 1-inch I.D. Haynes 230 central tube which has entry (#11) and exit (#13) lines for purge gas. The bottom of the Haynes tube is welded to a third flange (#14) that is bolted to a fourth flange (#15). O-rings (#10) are located in the fourth flange, and secure the bottom of the alumina liner. The feed gas out adapter (#16) is threaded into the fourth flange and provides an exit for the feed gas. A sweep gas in/out adapter (#19) is threaded into the feed gas out adapter. The sweep gas entry tube (#22) passes through the adapter and extends into the ceramic membrane (#26). The exit tube for the sweep gas (#21) is located at the side of the adapter. The ceramic membrane holder tube (#23) is threaded into the sweep gas adapter. The ceramic membrane is coupled to the holder tube using a cup (#24) and a ceramic seal (#25).

Over the course of the project these high pressure reactors were upgraded several times. Upgrades included larger diameter tubing for high flowrates, new pressure relief valves and regulators for high pressure operation up to 500 psi, and an alternative mechanical sealing mechanism for room temperature sealing of planar intermediate temperature layered composite membranes.

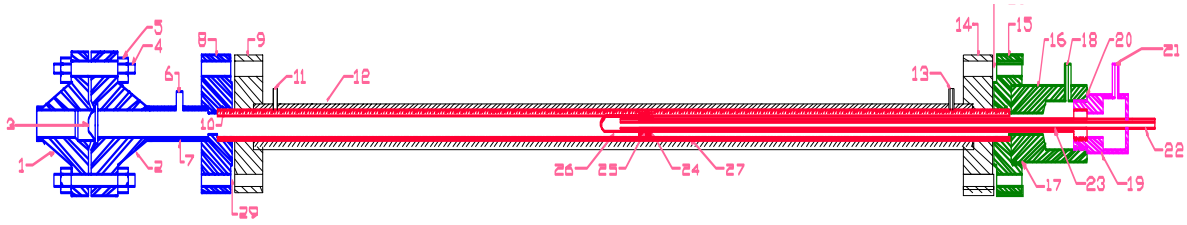

Figure 75. Diagram for the high-pressure hydrogen separation vessel.

A. Ceramic and Cermet Membranes

Operation of dense ceramic and cermet hydrogen separation membranes at high temperatures and pressures requires a chemically resistant seal with similar mechanical and expansion characteristics as the membrane material. Seal materials are being developed and tested using a closed-one-end tube configuration. Seal formation was achieved by ramping the cell assembly up to 1000°C in 10% H_2/90% N_2 and holding for a period of time. The assembly then was cooled to 800°C, for seal evaluation. High-pressure seals developed for ceramic membranes maintained at a differential pressure of ~250 psi for 2000 hours before termination of the test. A seal was also developed for cermet membranes. Multiple tests were performed using the $AB_{0.8}B^{c}_{0.2}O_{3-\delta}$/44 wt.% Metal-1 cermet composition and seals were routinely maintained at pressures in excess of 200 psi, with a maximum of 250 psi during a 72-hour test.

B. Intermediate Temperature Composite Layered Membranes

Layered composite membranes operating at intermediate temperatures were sealed using a room temperature mechanical seal. This type of seal allowed for rapid testing of membranes at high pressures. As described below, initially feed stream pressures up 250 psig were tested. As membrane performance increased high pressure reactor designs were upgraded to allow testing up to 500 psig and 1000 psig.

Based on ambient pressure results, a variety of alloy compositions were tested at higher pressures to evaluate both flux and membrane stability. Figure 76 shows H_2 permeation versus temperature for a 0.9-mm thick membrane at a differential pressure of 250 psi (ΔP_{total}). Under the flow conditions indicated in the figure, permeation increased to a maximum near 16 $mL \cdot min^{-1} \cdot cm^{-2}$ at approximately 400°C (permeability of 1×10^{-7} $mol \cdot m \cdot m^{-2} \cdot s^{-1} \cdot Pa^{-0.5}$). Permeation stabilized beyond 400°C, and this trend generally was observed for most of the compositions tested. Permeation increased linearly with temperature between 130 and 380°C, yielding an apparent activation energy for hydrogen diffusion of 13 kJ/mol. Permeation also increased linearly according to Sieverts' Law (*i.e.*, $p_f^{1/2} - p_s^{1/2}$) and peaked at over 20 $mL \cdot min^{-1} \cdot cm^{-2}$ at 360°C with the feed at 250 psi of 100% H_2. The most significant result was that this sample did not suffer from hydrogen embrittlement until well below 100°C, which indicated an improvement in stability relative to other compositions tested previously.

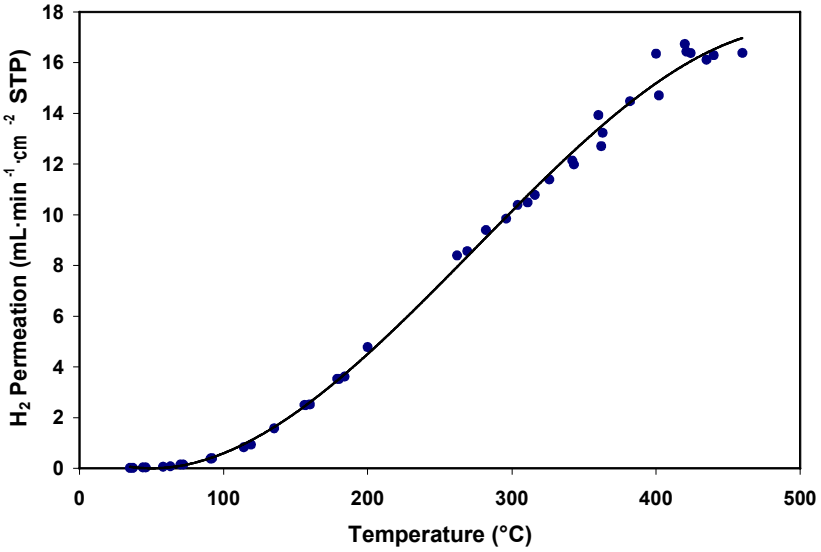

Figure 76. H_2 permeation versus temperature for a 0.9-mm thick membrane at a differential pressure of 250 psi. The feed gas was 500 mL/min of 40H_2/10He (bal N_2) and a the sweep gas was 450 mL/min N_2.

Figure 77 shows results for three membranes that varied only in the relative concentrations of the two major alloy constituents (*i.e.*, 90%/10%, 85%/15%, and 80%/20%). The membranes became more brittle as the minor constituent increased and the maximum total differential pressured achieved decreased from 450 to 126 psi. As a result, the highest flux for this series (78 $mL \cdot min^{-1} \cdot cm^{-2}$) was obtained for the 90/10 analog. Three different potential alloys were tested under similar high pressure hydrogen separation conditions. It was found that the

alloying element(s) and concentration significantly affect H_2 separation. Figure 78 shows H_2 permeation for three different alloys tested under similar conditions. All three alloys were annealed prior to testing. During permeation testing, H_2 flow rates varied between 1 and 2 L/min. In addition the sweep flow rate was 1 to 2 L/min. Figure 78 shows that the permeation varied significantly depending on the alloy. For Alloy A a maximum permeation of 75 mL•min^{-1}•cm^{-2} was measured. In addition, Alloy A could only be tested up to pressure differential of 75 psig. The maximum permeation for Alloy B was 76 mL•min^{-1}•cm^{-2}. This was very similar to the maximum permeation measured for Alloy A, except at a much higher partial pressure difference, as shown in Figure 78. Finally, Alloy C had a maximum permeation of 33 mL•min^{-1}•cm^{-2} at a total pressure differential of 433 psig.

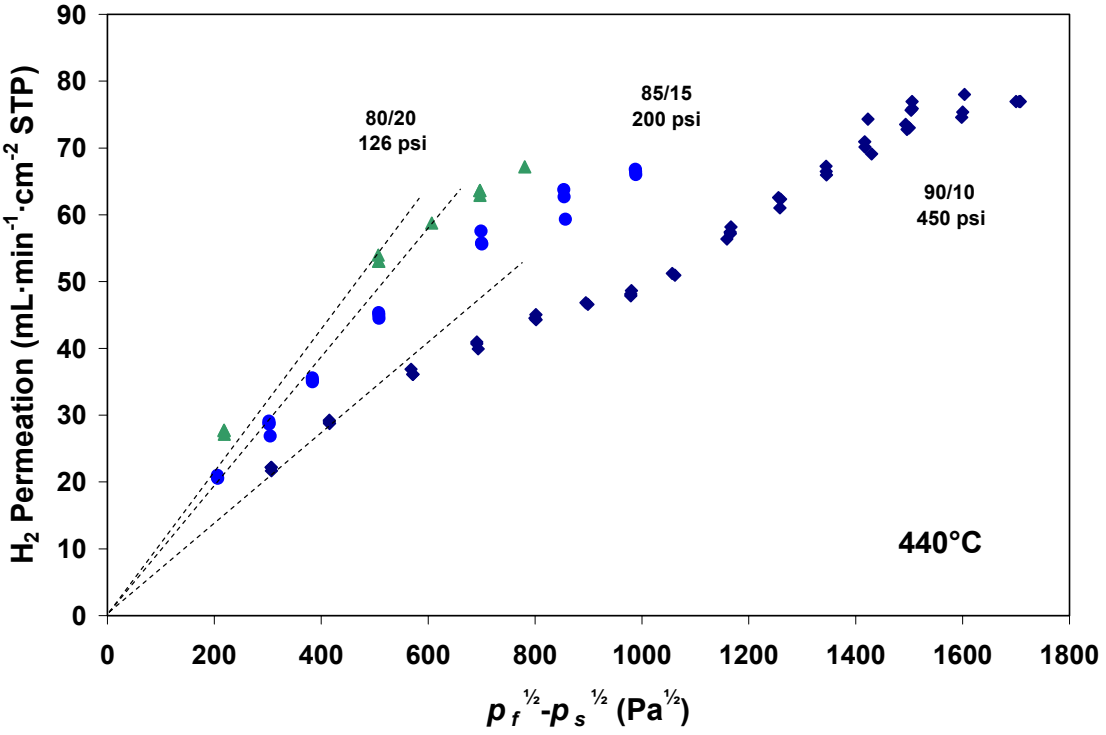

Figure 77. **H_2 permeation at 440°C versus the H_2 partial pressure difference across the membrane. The feed gas was ~80/20 H_2/He and the sweep gas was Ar. The feed and sweep flow rates were between 1 and 1.5 L/min. The straight dashed lines represent the flux predicted based on Sieverts' Law.**

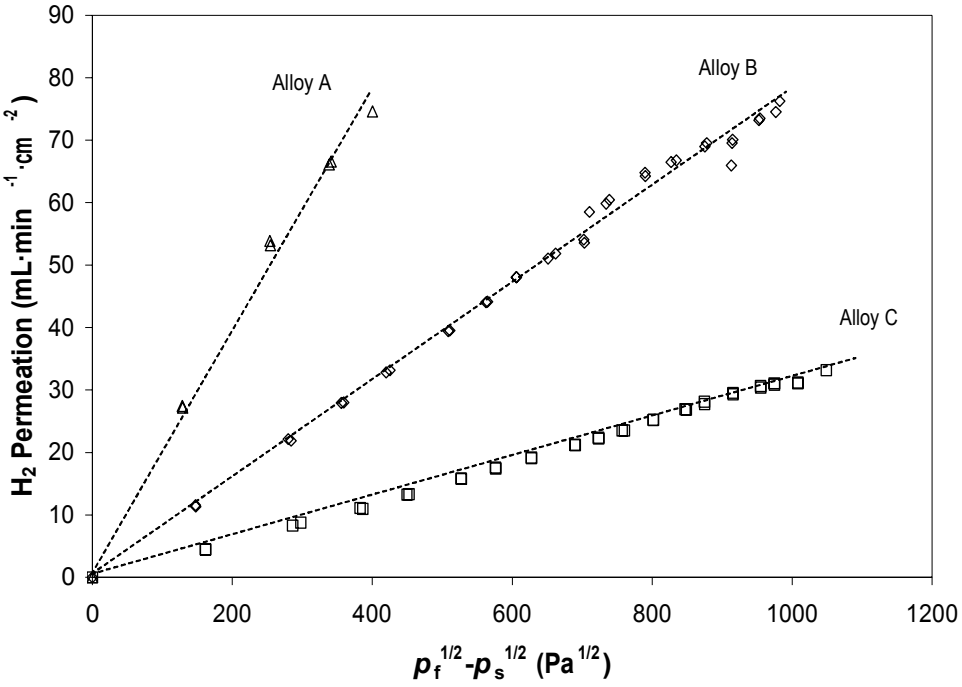

Figure 78. H_2 permeation at 440°C versus the hydrogen partial pressure difference across the membrane for three different alloys. The dashed lines represent the flux for each membrane based on Sieverts' Law.

Once an appropriate alloy composition was determined, flow rates were used to demonstrate that flux could be maximized by eliminating surface mass transfer limitations. Figure 79 shows H_2 permeation data collected for two equivalent membranes. Both membranes were tested at 440°C using a feed stream containing 40% H_2. For the first membrane (open triangles) the H_2 feed rate was held constant at 1 L/min. Under this flow rate, permeation began to deviate from Sieverts' Law at approximately 330 $Pa^{1/2}$ differential hydrogen pressure. For the second membrane (filled squares) the H_2 feed rate was increased to 2 L/min. Under this increased flow rate permeation did not begin to deviate from Sieverts' Law until 460 $Pa^{1/2}$ differential hydrogen pressure. Increases in the hydrogen flow rate allow Sieverts' Law to be maintained up to higher differential hydrogen pressures.

Figure 80 shows permeation results for a different membrane analog using even higher flow rates. Permeation reached a maximum of almost 250 $mL \cdot min^{-1} \cdot cm^{-2}$. Higher permeation likely was due to the much lower membrane thickness coupled with a sweep rate of 4 L/min. Deviation from Sieverts' Law occurred above a H_2 partial pressure differential of 700 $Pa^{½}$ suggesting that the membrane performance was still surface limited.

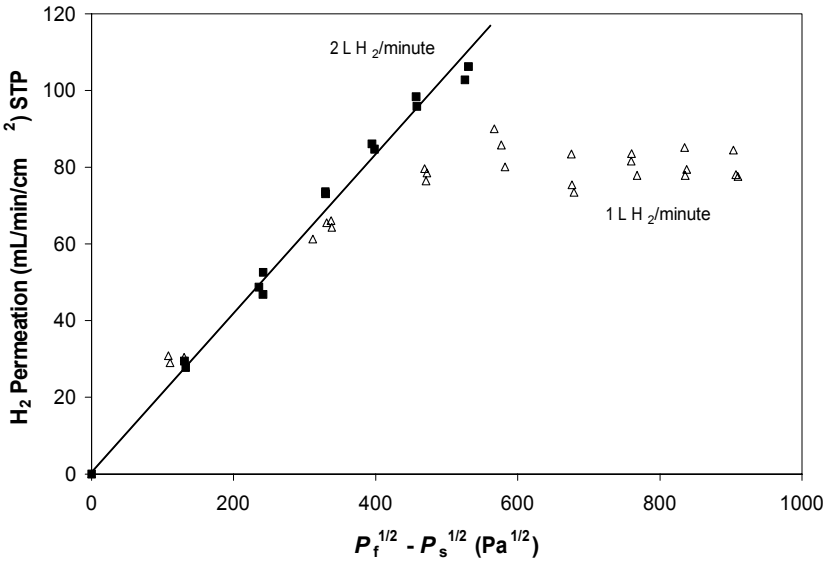

Figure 79. **H_2 permeation at 440°C versus the H_2 partial pressure difference across the membrane. Data was collected for two equivalent membranes with a feed gas stream of 40/60 H_2/He and the sweep gas was Ar. For the membrane represented by open triangles the H_2 flow rate was 1 L/min. For the membrane represented by filled squares the H_2 flow rate was 2 L/min. The straight dashed line represents the flux predicted based on Sieverts' Law.**

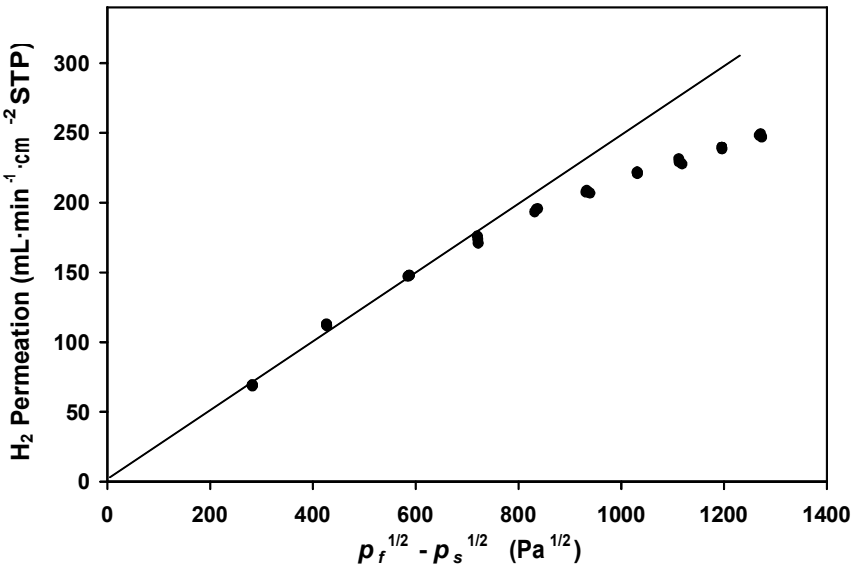

Figure 80. **Hydrogen permeation as a function of the differential hydrogen partial pressure across the membrane. The membrane was 0.12 mm thick and testing was performed at 440°C with a feed hydrogen concentration of 60 vol.%. The feed and sweep gas flow rates were 8 and 4 L/min, respectively. The total differential pressure across the membrane was at a maximum of 470 psi.**

Increasing the hydrogen concentration in the feed stream increases the hydrogen differential pressure across the membrane and therefore increases hydrogen permeation. Figure 81 shows permeation of a composite layered membrane as a function of H_2 feed concentration at 360°C and a differential pressure of 250 psi. Permeation increased from approximately 9 to 22 mL·min^{-1}·cm^{-2} as the H_2 feed concentration increased from 10 to 40 vol.%. In this case flow rates were not optimized. Figure 82 shows the hydrogen permeation for a composite layered membrane under a feed stream containing 40% H_2 / 60% He. A permeation of 225 mL·min^{-1}·cm^{-2} was measured. The dashed straight line represents flux predicted by Sieverts' Law. Figure 82 shows that Sieverts' Law is maintained up to 450 psi differential hydrogen pressure with only 40% hydrogen in the feed stream. Increasing the concentration of hydrogen in the feed stream to 80% increased the hydrogen permeation to 350 mL·min^{-1}·cm^{-2}.

The highest hydrogen permeation recorded at Eltron Research, Inc. during this project was 423 mL·min^{-1}·cm^{-2} at a pressure differential of 475 psig. Figure 83 shows hydrogen permeation vs. the difference in hydrogen partial pressure for a composite layered membrane tested at 440°C. A permeation rate of 423 mL•min^{-1}•cm^{-2} was achieved in Figure 83 under a feed flow rate between 2.5 and 2.8 L/min. The concentration of H_2 in the feed stream was varied between 40 and 100%. Figure 83 shows that permeation data fit well with the permeation predicted by Sieverts' Law.

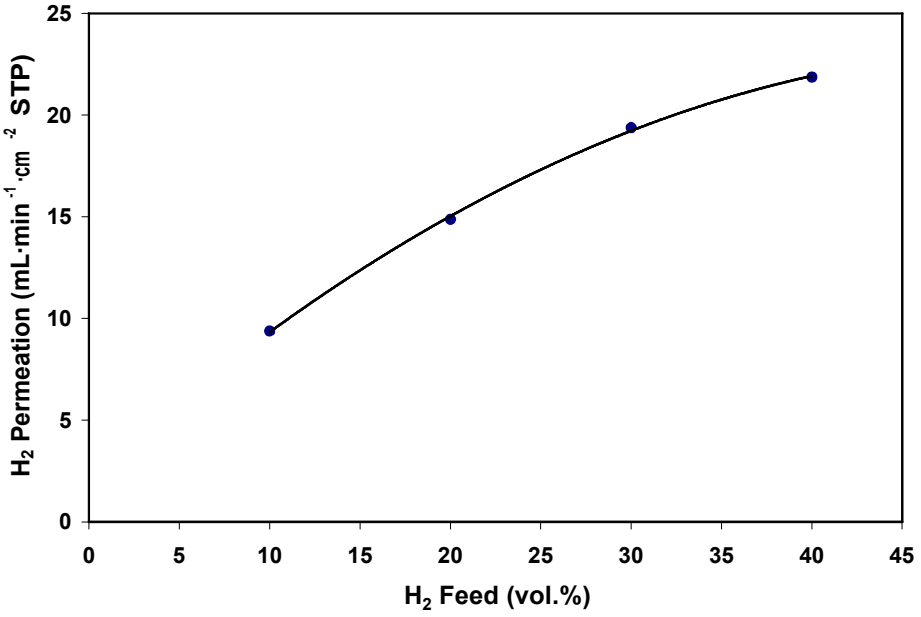

Figure 81. Hydrogen permeation of a layered composite membrane as a function of feed concentration at 360°C and a differential pressure of 250 psi.

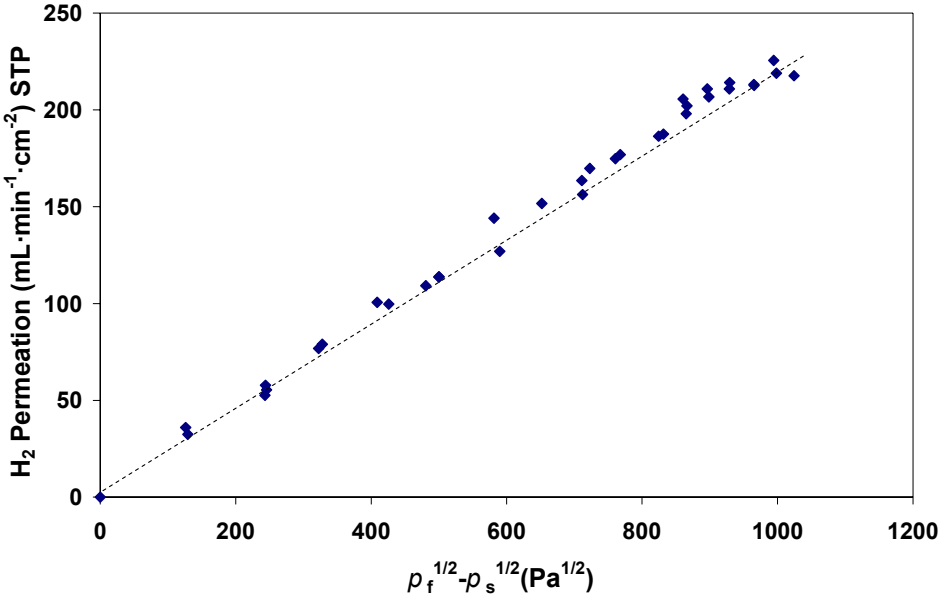

Figure 82. **H_2 permeation at 440°C versus the H_2 partial pressure differential across the membrane. The feed gas stream was 40/60 H_2/He and the sweep gas was Ar. The feed and sweep flow rates were between 2.5 and 6.25 L/min. The straight dashed line represents the flux predicted based on Sieverts' Law.**

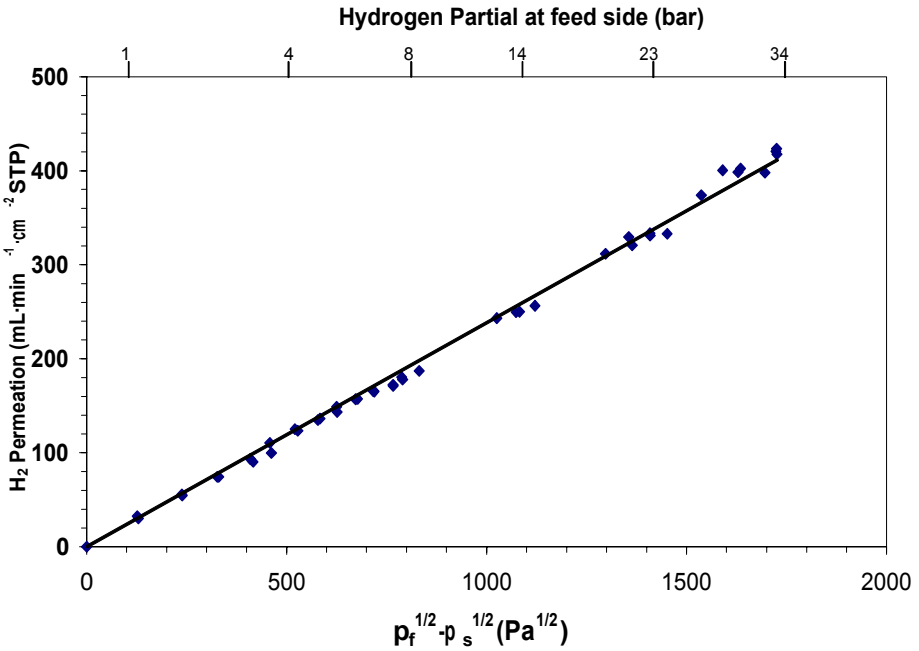

Figure 83. **H_2 permeation at 440°C versus the hydrogen partial pressure difference across the membrane. The feed flow rate was less than 3 L/min. The sweep flow rate was greater than 7 L/min, and the total pressure differential was 475 psi. The straight line represents the flux predicted based on Sieverts' Law.**

Composite layered membranes were tested as high as 1000 psig on the feed side of the membrane. These high pressure experiments were designed to demonstrate the ability to operate Eltron's composite layered membranes under DOE's expected IGCC operating conditions. Figure 84 shows a plot of hydrogen permeation versus the partial pressure difference across the membrane. A hydrogen permeation of 101 $mL \cdot min^{-1} \cdot cm^{-2}$ was measured at 1010 psig. Flow rates and temperature were not optimized for this demonstration test. It is expected that under appropriate operating conditions higher permeation values can be obtained.

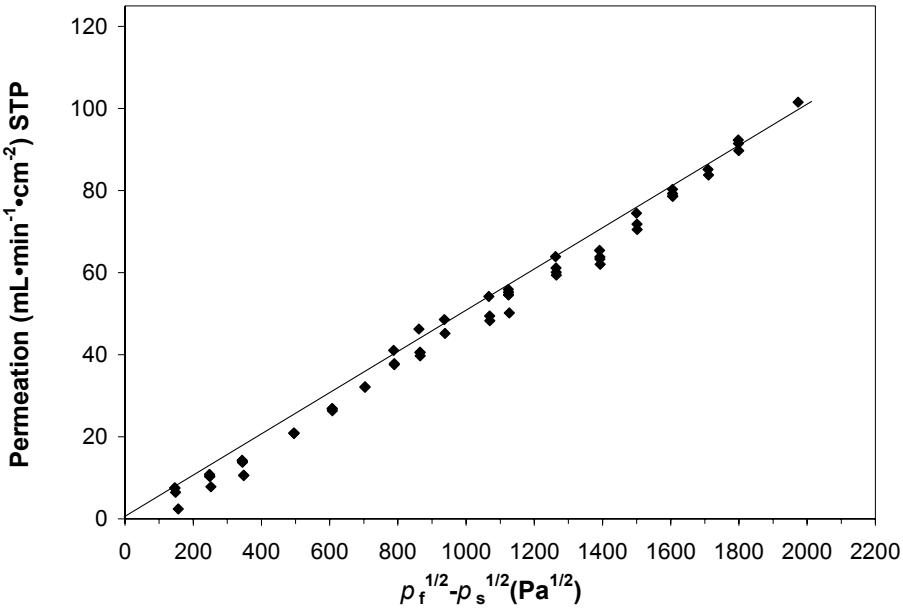

Figure 84. H_2 permeation at 420°C versus the partial pressure difference across the membrane. The total pressure differential was 1010 psi. The straight line represents the flux predicted based on Sieverts' Law.

One of the key requirements for the eventual implementation of hydrogen separation membranes in coal gasification power plants is membrane stability when a pure hydrogen atmosphere exists on the permeate side of the membrane. Eltron tested several different layered composite membrane thicknesses under a 100% hydrogen permeate stream conditions. Figure 85 shows that at 435°C and a 300 psig feed stream the membrane permeation was stable for all three thicknesses. After three hours the experiments were voluntarily terminated for post reactor analysis.

As described above, most permeation testing involved single day tests designed to maximize permeation by varying feed and sweep flow rates, pressure, temperature, and gas composition. As the project progressed, intermediate temperature composite layered membranes were tested for increasing longer times to demonstrate membrane stability. Figure 86 shows a plot of permeation vs. time for two membranes tested for 80 hours at 400°C, 300 psig feed stream pressure (40% H_2), and a 100% hydrogen permeation stream. For both membranes a slight decrease in permeation was observed during the first ten hours of the experiment. This initial loss of permeation has been observed at Eltron and in the literature and is attributed to the initial equilibration of hydrogen within the lattice vacancies of the composite membrane. Following this initial equilibration membrane permeation was very stable. The first membrane

had a permeation of greater than 120 mL·min^{-1}·cm^{-2} after 80 hours of testing, and the second membrane had a permeation of greater than 80 mL·min^{-1}·cm^{-2}. After 80 hours the membranes were characterized with X-ray diffraction. Results showed no surface contamination or undesired phase formation.

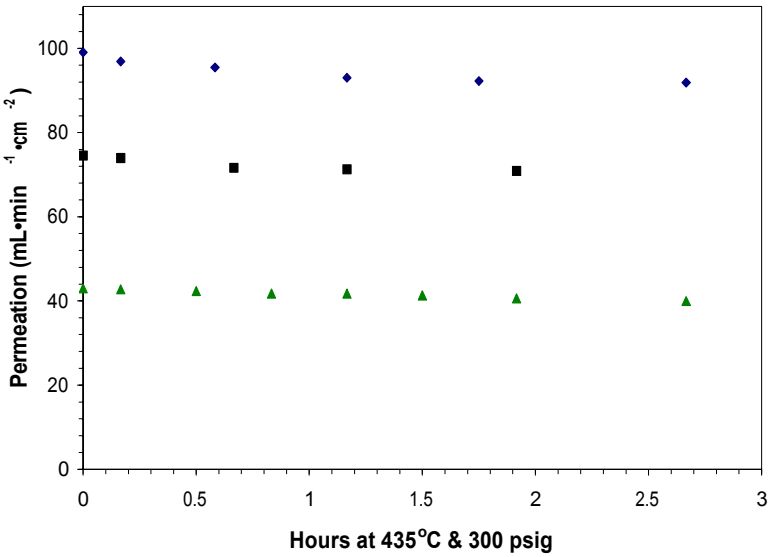

Figure 85. Hydrogen permeation for membranes with three different thicknesses tested at 435°C, 300 psig feed pressure, and a 100% hydrogen permeate stream.

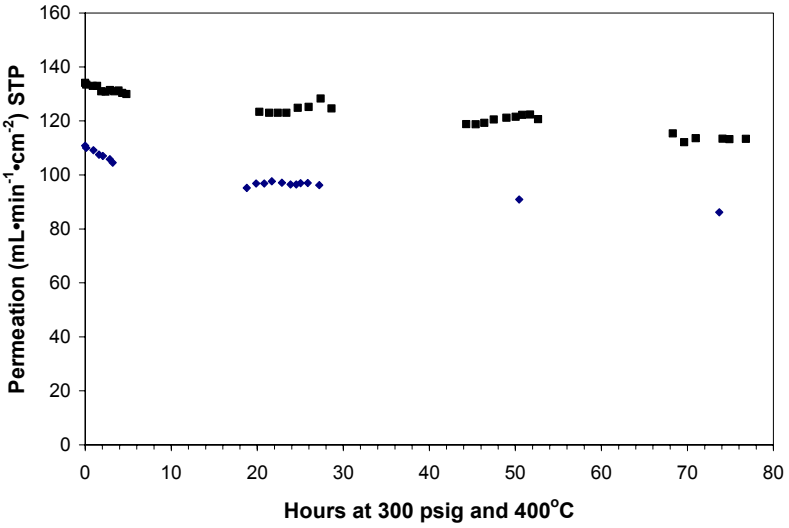

Figure 86. Graph of permeation vs. time for two composite layered membranes held at 400°C and 300 psig for 80 hours.

Additional membranes were tested for longer periods of time. Figure 87 shows a plot of permeation vs. time for a membrane tested at 400°C with a 300 psig 40% H_2 feed stream and an ambient pressure 100% H_2 permeate stream for 240 continuous hours. Permeation initially was 135 mL•min^{-1}•cm^{-2}, and after 240 hours the permeation was still greater than 80 mL•min^{-1}•cm^{-2}. After 240 hours the membrane was brought back to ambient conditions and examined with X-ray diffraction (XRD) and Scanning Electron Microscopy (SEM). XRD and SEM showed that the membrane was intact and no undesired phase formation was present. A second membrane was run under equivalent conditions for over 400 hours. After 400 hours the permeation was greater than 50 mL•min^{-1}•cm^{-2}.

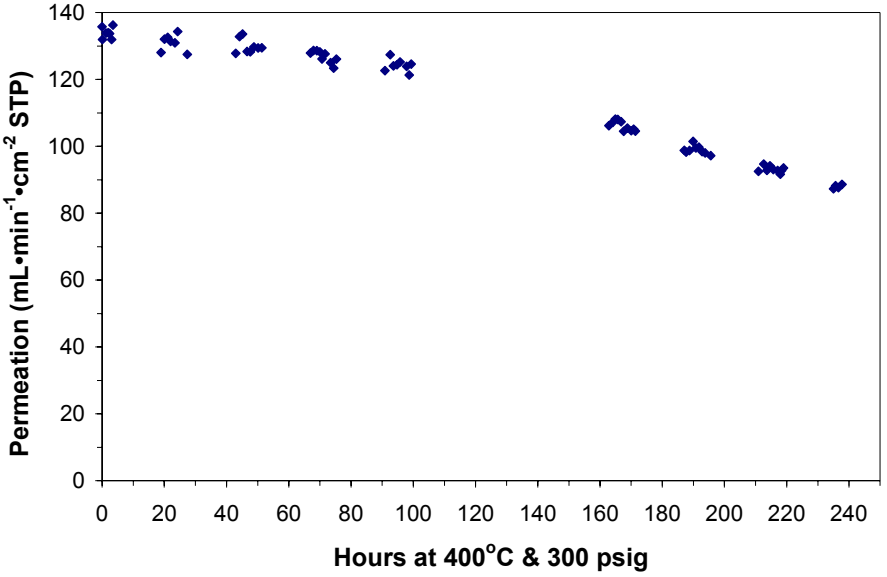

Figure 87. Composite layered membrane tested at 400°C and 300 psig for 240 continuous hours.

III. Task 4 Thin-Film Hydrogen Separation Membranes

Contributors: CoorsTek, Eltron

The advantage of thin films is a higher permeation rate. The disadvantage of thin films is that they must be supported to be able to withstand the pressures required and the processing methods must be precise to avoid pin holes or other defects in the thin film. Other factors that must be considered include shrinkage of the porous support and thin film during sintering, porosity of the porous support, and the ability to form an adequate seal to the thin film. During this project several different types of hydrogen separation membranes and two different configurations were tested for thin film hydrogen separation membranes applied to porous supports.

A. Planar Thin Film Hydrogen Separation Ceramic

Initially, tape casting and spin coating were used to prepare thin films of perovskite hydrogen separation ceramics with the general formula $AB_{0.8}B^{b}_{0.2}O_{3-d}$. Dense films between 10 and 100 μm were prepared. An example is shown in Figure 88 demonstrating a ~100 μm thin film membrane on a porous support of the same composition. The tape casting slurry recipe was optimized to achieve a defect-free membrane absent of "pin holes". However, the shrinkage rate for this composition was much different than the support, which compromised adherence of the membrane, and made H_2 separation evaluation difficult. Despite this limitation, a relatively *thick* membrane (0.5 mm) prepared by the thin film tape casting technique demonstrated H_2 separation in excess of 0.01 $mL \bullet min^{-1} \bullet cm^{-2}$ and an ambipolar conductivity of $\sim 10^{-4}$ S/cm. Although these values were well below the best results for thick ceramic membranes and cermets described above, it is encouraging that this procedure generated test-worthy samples. Spin coated samples also demonstrated the same shrinkage problem described above, and efforts to overcome this limitation resulted in highly porous films.

Figure 88. SEM image of a dense thin ceramic film (bottom) on a porous support of the same composition (top). The white bar represents 100 μm, which is also about the thickness of the film.

The shrinkage of the thin film can be controlled by varying the surface area of the powder prior to sintering, whereas shrinkage of the support is controlled primarily by the degree of porosity or the content of pore forming additive included in the powder prior to sintering. Figure 89 shows the variation in disk shrinkage for a porous support and a porous support with a thin film. The composition of the support and thin film is represented as $AB_{0.8}B^{b}_{0.2}O_{3-\delta}$. There was very little difference between the samples, and both had a clear maximum in shrinkage at a pore formation additive content of 41.2 wt.%. The inset in the figure shows the shrinkage of the thin film without the support as a function of the surface area of the powder prior to sintering. Based on the shrinkage data in Figure 89, appropriate combinations of porous supports and thin film precursors were prepared, and supported thin film samples were fabricated without cracks or delamination. Permeation rates roughly equivalent to thick membranes (~0.1 to 0.2 $mL \bullet min^{-1} \bullet cm^{-2}$) were measured.

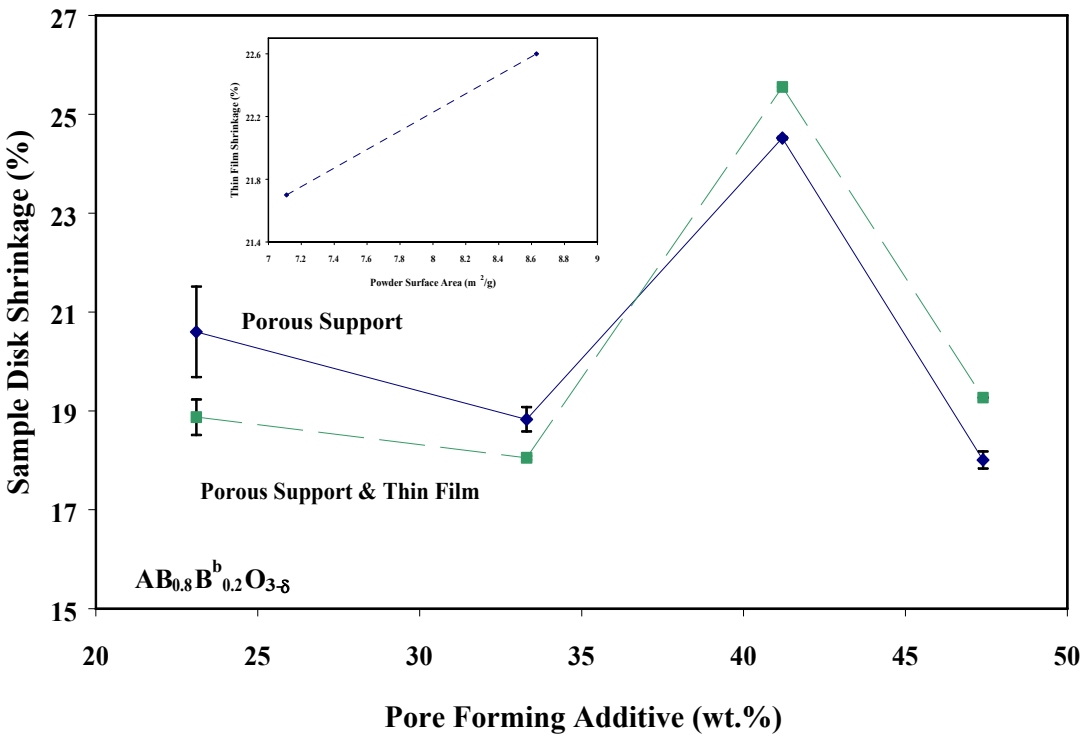

Figure 89. Plot showing the percent shrinkage versus wt.% of pore formation additive included in the porous support powder prior to sintering. The inset shows shrinkage of the thin film alone (without the support) as a function of powder surface area prior to sintering.

B. Planar Thin Film Hydrogen Separation Cermet

Thin film cermets of the composition $AB_{0.8}B^{b}_{0.2}O_{3-\delta}$ / 44 wt.% metal were prepared using tape casting. Metal powder particle size was varied to optimize sinterability, and ceramic particle size was reduced to maintain a constant ratio between the metal and ceramic particle sizes. Agglomeration of metal particles in thin film slurries was minimized by employing a two-part dispersant system and varying the dispersant content. Binder burn out and sintering conditions were tested at CoorsTek. Membranes were fabricated with two and three thin film layers tape cast on porous supports; however, only the three-layer samples were sufficiently dense to achieve acceptable seals for testing. Figure 90 shows results for a 1.9-mm thick sample with a 0.1-mm thick membrane. Although this thickness was within the range routinely achieved by grinding standard membrane samples, the H_2 permeation rate was about three times lower than the best results for this composition. This decreased performance might be the result of resistance through the porous support.

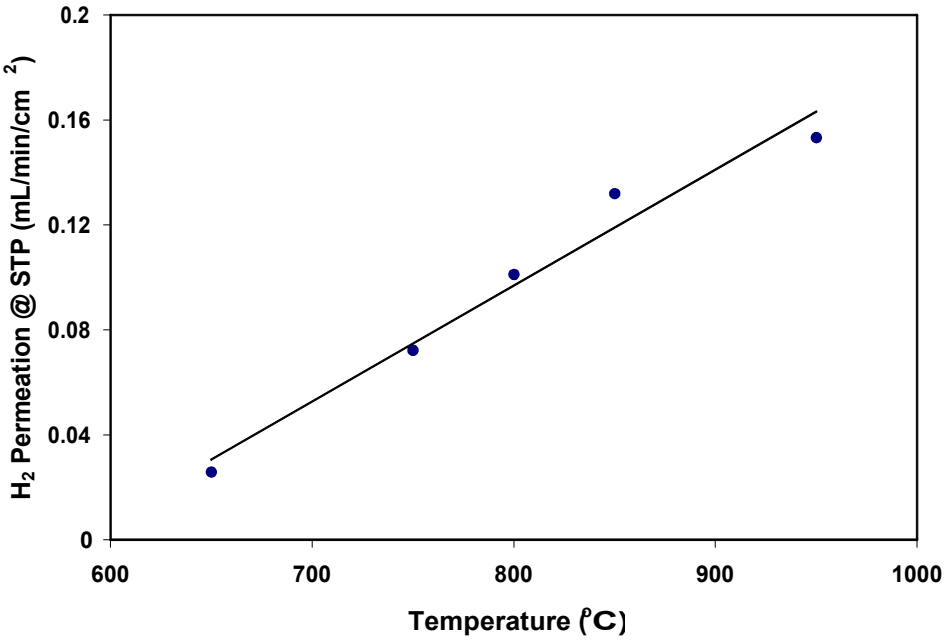

Figure 90. H_2 permeation as a function of temperature for a 0.1-mm thick three-layer tape cast membrane on a porous support. The membrane composition was $AB_{0.8}B^c_{0.2}O_{3-\delta}$/44 wt.% Metal-1. The feed gas was 80/20 H_2/He and the sweep gas was Ar. Gas flow rates were between 80 and 110 mL/min.

C. Tubular Thin Film Hydrogen Separation Cermet

Tubular supported thin films were tested as an alternative to planar thin film hydrogen separation membranes. In this case a slurry was used to coat the inside of a green body tube rather than using tape casting or spin coating. The three processes that will be considered for manufacturing these supports are: i) isopressed closed one end (COE) tubes, ii) extruded OBE tubes, and iii) extruded COE tubes. A variety of different green BCY/Ni tubes were isopressed at Eltron and provided to CoorsTek for development of the appropriate coating and sintering procedures.

The optimal bisque firing temperature appeared to be 1100°C. The corresponding shrinkage was 13% out of a total shrinkage of ~20%. The bisque tube in this condition appears to have the minimum amount of strength required for handling. The fired tubes have excellent strength and no binder burnout issues, however, they have no shrinkage left to match that of the membrane and may result in stresses or even cracking of the membrane.

Two dispersion systems were used to suspend the membrane slurry. The system based on a slower drying solvent yielded better results than the faster drying system on bisque-state tubes. The viscosity and solids loading of the membrane will need to be optimized to minimize the membrane thickness. A digital Brookfield computer interface rheometer was used to characterize the slip viscosity. Optimizing the dispersion system is necessary to control membrane thickness and uniformity in a defect-free state.

Bisque fired tubular supports were tested first with the thin film deposition. The resulting membranes deposited on the 1100°C bisque fired tubes did not coat uniformly. This result was attributed to excessive porosity of the bisque fired tubes. SEM measurements indicated that the membrane thickness was 70 μm. CoorsTek will work with Eltron to modify the isopressing formulation with a decreased amount of pore former to reduce the porosity and increase the strength of the bisque fired support. CoorsTek will then optimize the viscosity and percent solids to further reduce the thickness of this membrane.

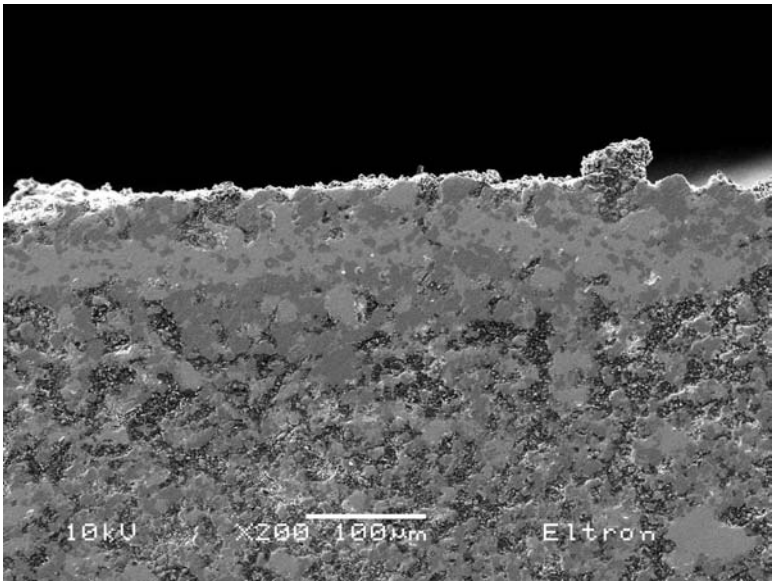

Figure 91. x200 SEM image of a thick dense BCY/Ni film applied to the inside diameter of a porous closed-one end tube.

Initial green tube supports were fired at 1390°C in forming gas and the metal phase migrated to the surface and formed beads. The firing temperature was reduced to 1360°C and the beading was mostly eliminated. Once the firing temperature had been optimized, twelve green BCY/Ni isopressed closed one-end (COE) tubes were prepared at Eltron Research Inc. Thin film slurry was deposited on the inside diameter of the tubes by CoorsTek. Coated tubes were sintered at 1360°C for 4 hours in a forming gas atmosphere. A SEM image of a cross-section of a sintered tube is shown in Figure 91. A dense coating was found with a highly variable thickness of 99(23) μm. Further development of the thin film slurry allowed deposition of a thinner dense layer as shown in Figure 92. Figure L clearly shows the inner curvature of the thin film tube. The average thickness of the dense thin film in was 15(3) μm. The inside diameter of sintered tubes will be ground to 0.24" for sealing to a 0.250" outer diameter alumina tube. A precious metal seal has been developed for sealing the BCY/Ni COE tube to alumina tubing to allow leak-free permeation testing at Eltron Research Inc. Once sintered, tubes were brazed onto alumina tubing as shown in Figure 93.

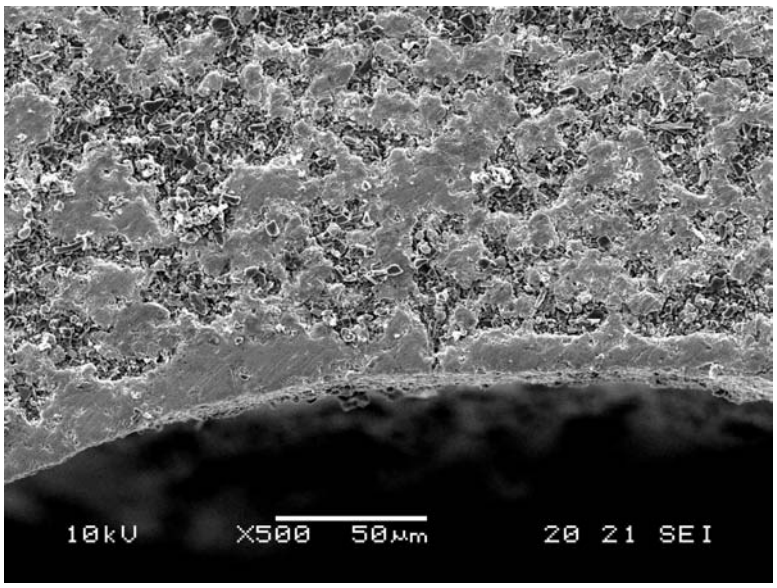

Figure 92. x500 SEM image of a thin BCY/Ni dense film applied to a porous closed-one-end tube.

Dense thin film tubes were tested for permeation between 700 and 850°C and at ambient pressure with an 80% hydrogen feed stream. Permeation results for one of the tubes are shown in Figure 94. The data shows that permeation decreased as the temperature decreased from 850°C to 800°C as expected, however, lowering the temperature to 700°C did not affect the permeation. This trend is consistent with ANL data which also showed a constant flux between 850 and 750°C. In addition to temperature the feed stream flow rates were varied, however, no effect on permeation was observed. SEM analysis showed that the thin film was 20 µm thick. The measured permeation data of the thin film tubes was 0.012 mL/min/cm^2 which was lower than expected for a thin dense film of BCY / Ni. The low permeation data was attributed to a small leak which may have affected the data. SEM analysis following permeation testing indicated that the leak was not occurring through the thin film and was likely due to poor adhesion of the braze. Based on this low permeation data, testing of thin film BCY / Ni tubes was not continued.

Figure 93. Dense BCY/Ni thin film tube brazed onto a 1/4" alumina tube.

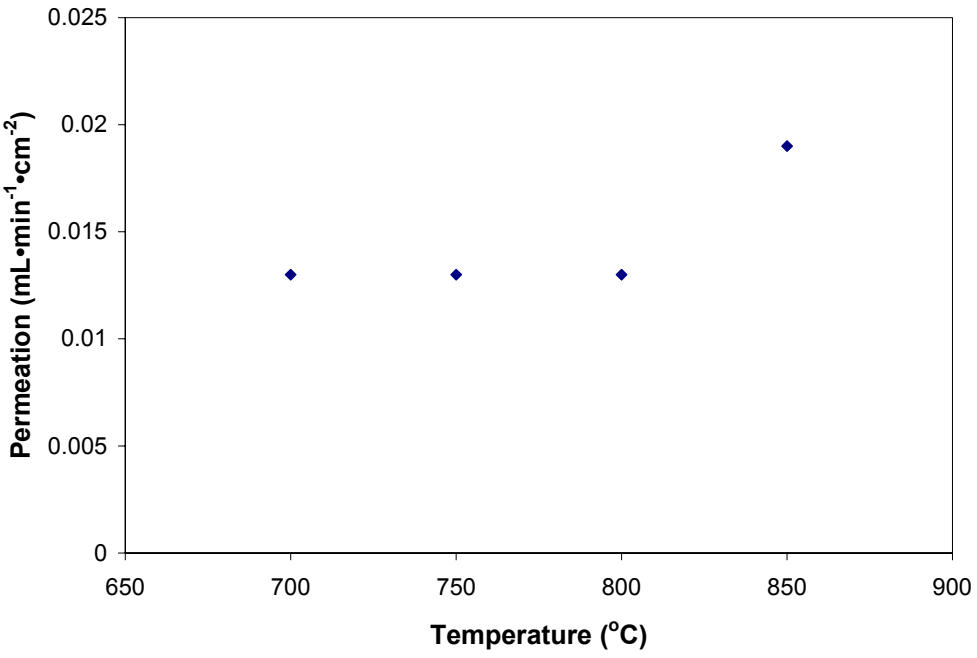

Figure 94. Permeation as a function of temperature for a thin BCY/Ni film on a tubular porous support.

IV. Task 5 Construction and Evaluation of Prototype Hydrogen Separation Unit

Contributors: NORAM

The original goal of Task 5 was design and construction of a scale-up hydrogen separation unit based on ceramic tubular membranes. As the project progressed towards layered composite membranes due to their superior performance, Task 9 was added to scale up those types of membranes. The goal of Task 5 was therefore shifted to prepare the necessary engineering documentation for incorporation of a hydrogen separation unit based on Eltron's technology into a large IGCC power plant.

NORAM produced five different engineering documents. A brief description of each document is included below. The full documents can be found in the Appendices as listed below.

1. Process Report: Criteria for Incorporating Eltron's Hydrogen Separation Membranes into Vision 21 IGCC Systems and FutureGen Plants Rev B (31 Dec 2004)

Appendix A

This report describes criteria for incorporating hydrogen separators based on Eltron's membranes into an IGCC flowsheet given their specific temperature requirements, tolerance to poisons, etc. Process simulations were prepared which determine a range of process conditions, which the membranes would likely encounter based on a review of the latest information on warm gas cleaning, gasification, and other relevant technologies. A spreadsheet-based model of a separator was created to evaluate membrane area requirements given the changing conditions through the separator for different gas compositions, pressures, hydrogen separation requirements, and sweep gas usage rates.

2. Mechanical Report: Study of Design Criteria and Manufacturing Concepts for Pilot-Scale and Full-Scale Hydrogen Separators (26 Sep 2005)

Appendix B

This report reviews the mechanical considerations related to the design and fabrication of large, high-pressure hydrogen separators using Eltron's membranes. Several conceptual separators designs were prepared ranging in size from pilot to full scale. This report discusses the design criteria, design basis and details of each separator design. Preliminary cost estimates for the separators were also prepared for this report.

3. Eltron Membrane Evaluation Matrix

Appendix C

An evaluation matrix was prepared which ranks each of Eltron's different membrane types as well as competing technologies, based on cost (unit and system), process advantages, mechanical considerations, development time and risk.

4. Conceptual Process and Control Description and Diagram

Appendix D

A conceptual process and control description was prepared for a hydrogen separation system utilizing multiple separator units based on Eltron's intermediate temperature composite membranes. The system described includes multiple units operating in parallel, along with the required ancillary services, such as the preheat / purge gas system, permeate cooling, recompression, etc. A Process and Instrumentation Diagram was prepared as part of this document, which illustrates the equipment, piping and instrumentation discussed in the description.

5. Hydrogen Separation System Cost Estimate and 3-D Layout Drawings

Appendix E

A cost estimate was prepared for a complete, installed hydrogen separation system including cost estimates for the separator units, other major equipment required, valves and piping as well as an estimate of the total installed system cost. For information, cost estimates were also prepared for the other separator designs including the pilot and mid-sized separators and low-pressure full-scale separator. Included in the cost estimate document are three conceptual equipment layout drawings prepared using a 3-D AutoCad model. Because a 3-D model has been prepared, any number of views can be easily selected.

V. Task 6 Membrane-Promoted Conversion of Alkanes to Olefins

Contributors: Eltron

Several different reactor configurations, catalysts, and membrane types were tested for hydrogen membrane promoted dehydrogenation of propane to propylene. In the first reactor configuration oxygen was supplied to the permeate side of the membrane to react with separated H_2 to form H_2O and therefore provide a driving force for hydrogen separation. In this case dehydrogenation proceeded according to,

feed side: $CH_3CH_2CH_3 \rightleftharpoons CH_2{=}CHCH_3 + H_2$

H_2 permeate side: $H_2 + \frac{1}{2}O_2 \rightleftharpoons H_2O$

net: $CH_3CH_2CH_3 + \frac{1}{2}O_2 \rightleftharpoons CH_3CH{=}CH_2 + H_2O$

Thus, although the net reaction is an oxidative dehydrogenation, the O_2 and propane remain separated by the membrane. Propane dehydrogenation typically is less than 50% selective, and previous testing at Eltron indicated significant quantities of ethylene, ethane, and methane also are produced.[10] Percent conversion (%C) and percent selectivity (%S) were calculated according to:

$$\%C = \frac{[\text{Propylene}]}{[\text{Propane}]}(100) \tag{13}$$

$$\%S = \frac{[\text{Propylene}]}{[\text{Propylene}] + \frac{2}{3}[\text{Ethylene}] + \frac{2}{3}[\text{Ethane}] + \frac{1}{3}[\text{Methane}]}(100) \tag{14}$$

Initially, cermet membranes with the composition $AB_{0.8}B^{c}_{0.2}O_{3-\delta}$/60 vol.% Metal-2 were tested. 3.75 wt.%Pt/1.25 wt.%Sn/MgO was the alkane dehydrogenation catalyst on the propane feed side of the membrane and $La_{0.8}Sr_{0.2}CoO_3$ (LSC) was the oxygen dissociation catalyst on the H_2 permeate side of the membrane. Catalysts were applied to the membrane surfaces using a slurry deposition method. The feed side contained 10/23/66 vol.% propane/He/Ar mixture at a total flow rate of 90 mL/min. The propane source also contained small quantities of methane, ethylene, ethane, iso-butane, and butane. The sweep side contained 120 mL/min Ar. Membranes were tested between 650 and 800°C. GC measurements showed that after passing through the membrane cell, the quantity of propane, iso-butane, and butane were reduced dramatically, and quantities of all the other species increased along with H_2 and a very large amount of propylene. Figure 95 shows the ratio of propylene to propane after passing through the cell as the temperature increased; however, only a fraction of the H_2 formed passed through the membrane. The maximum permeation rate measured at 800°C was approximately 0.009 mL/min/cm^2.

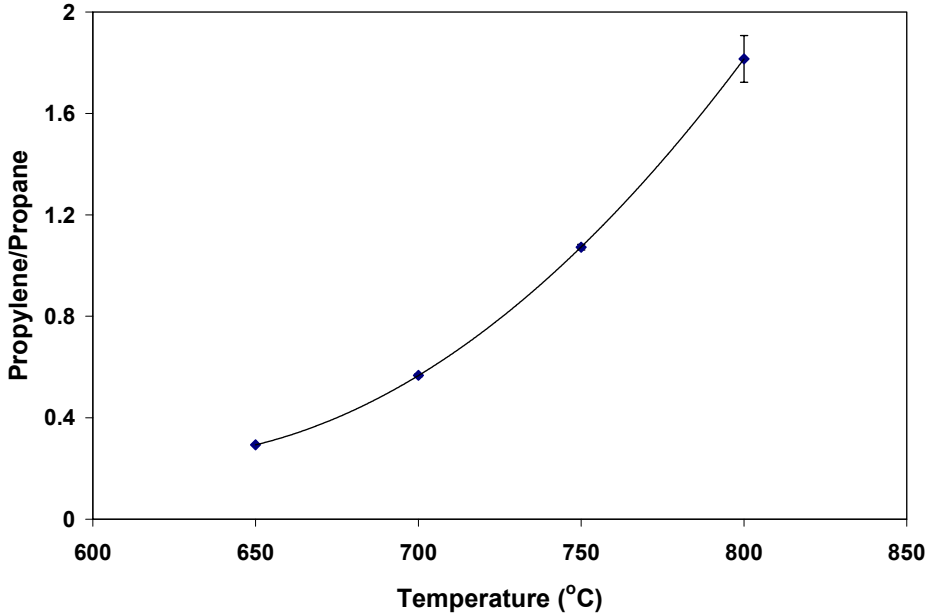

Figure 95. Plot of the propylene to propane ratio as the temperature was increased in a catalytic membrane reactor for alkane dehydrogenation.

In an effort to promote both dehydrogenation and hydrogen permeation, platinum was deposited onto both surface of a 0.21 mm thick cermet membrane. The feed gas was 80 mL/min of 10% propane (bal. Ar) and 15 mL/min He. Using 120 mL/min Ar on the membrane permeate side, conversion of propane was only 18.5% and the propylene yield was only 4.4%. H_2 permeation through the membrane resulting from propane dehydrogenation was approximately 0.014 mL/min/cm^2. Although these results were not compelling, hydrogen from the dehydrogenation of propane did permeate through the membrane and increasing the driving force did affect propylene yield.

A Pt-coated 0.13-mm thick metal-based membrane was instead of a cermet to determine the effect on percent conversion. The feed gas was humidified 80 mL/min of 10% propane (bal. Ar) and 15 mL/min He. The sweep gas was 80 mL/min air and 40 mL/min Ar. The maximum temperature tested was only 550°C, and as a result the maximum propane conversion and propylene yield were only about 8% and 3%, respectively (compared to 18% and 4% at 650°). However, despite the lower extent of dehydrogenation, hydrogen permeation through the membrane was about the same at 0.01 mL/min/cm^2. Also, very little coke formation was apparent on the membrane surface, likely due to addition of humidity in the feedstream.

The dehydrogenation catalyst was switched to a Pt/Sn catalyst supported on mullite grains. Tests were performed at temperatures between 500 and 600°C using a composite metal alloy membrane. The feed gas comprised 60 mL/min of humidified 10 vol.% propane (bal. Ar) and 10 mL/min He for leak detection. The sweep gas was 120 mL/min Ar. Results are presented in Figure 96 for propane to propene conversion, selectivity for propene formation, and percentage of hydrogen permeating the membrane at 500, 560, and 600°C. Propane yield increased from approximately 10 to 17% with increasing temperature, but still fell far short of the theoretical equilibrium value (~ 30%). Moreover, less than 1 mL/min of H_2 was generated during the dehydrogenation, and only a few percent were transported across the membrane surface. With these low values it is difficult to resolve any effect of the membrane on the target reaction. Selectivity showed a slight maximum at 560°C, but H_2 permeation decreased from 7.5% to only 2% over the test range. The decrease in permeation despite the increase in conversion likely is due to carbon formation on the membrane surface.

It was thought that the surface area of the catalyst was limiting both dehydrogenation and hydrogen permeation. Pt/Sn catalyst was deposited onto mullite saddles and three equivalent experiments were performed with an increasing amount of Pt/Sn dehydrogenation catalyst present in the feed stream of the reactor. The first experiment used 20 mullite saddles, 40 saddles were used in the second experiment, and 80 saddles used in the third experiment. Each experiment was performed at 500°C with a 70 mL/min flow rate of a 10% propane / balance Ar mixture fed to the reactor. A small amount of helium was included in the feed stream for leak detection. Propane conversion was calculated by measuring the amount of propane flowing into the reactor and the amounts of propane and propene exiting the reactor in the retentate stream. Figure 97 shows that the percent propane conversion and percent selectivity. Propane conversion varied between 1 and 2% and was not dependent on the surface area of the catalyst. The percent selectivity of propane to propene conversion was calculated to be 65% for each experiment and was also not dependant on the surface area of the catalyst. No hydrogen was detected by GC on the permeate side of the membrane. This suggests that the rate of hydrogen production from alkane dehydrogenation was not fast enough to provide the hydrogen partial pressure driving force necessary to effectively separate the hydrogen produced. A catalyst with a

higher rate of propane conversion would be necessary to quantify the advantages of membrane promoted alkane conversion.

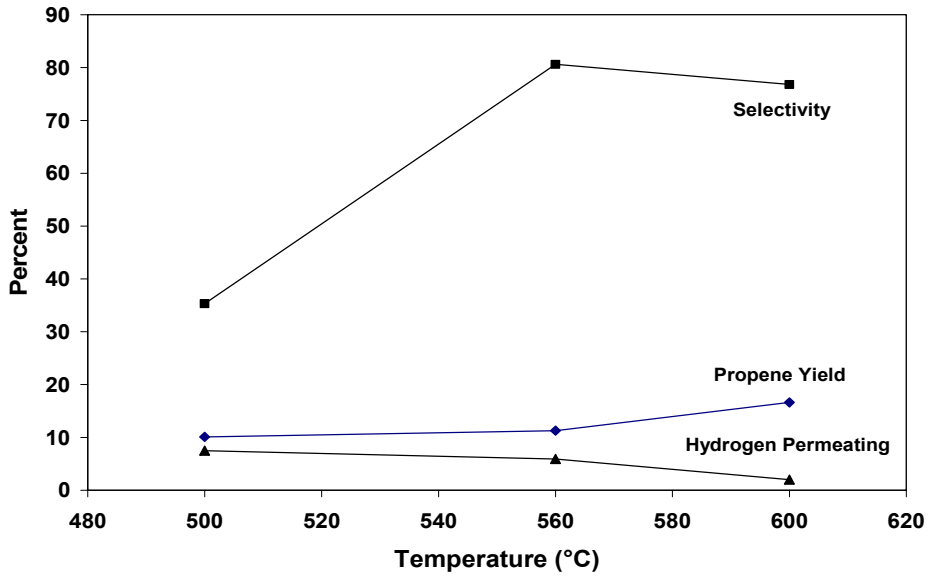

Figure 96. Plot showing percent selectivity for propane formation (squares), propene yield (diamonds), and percent hydrogen transported across the membrane (triangles).

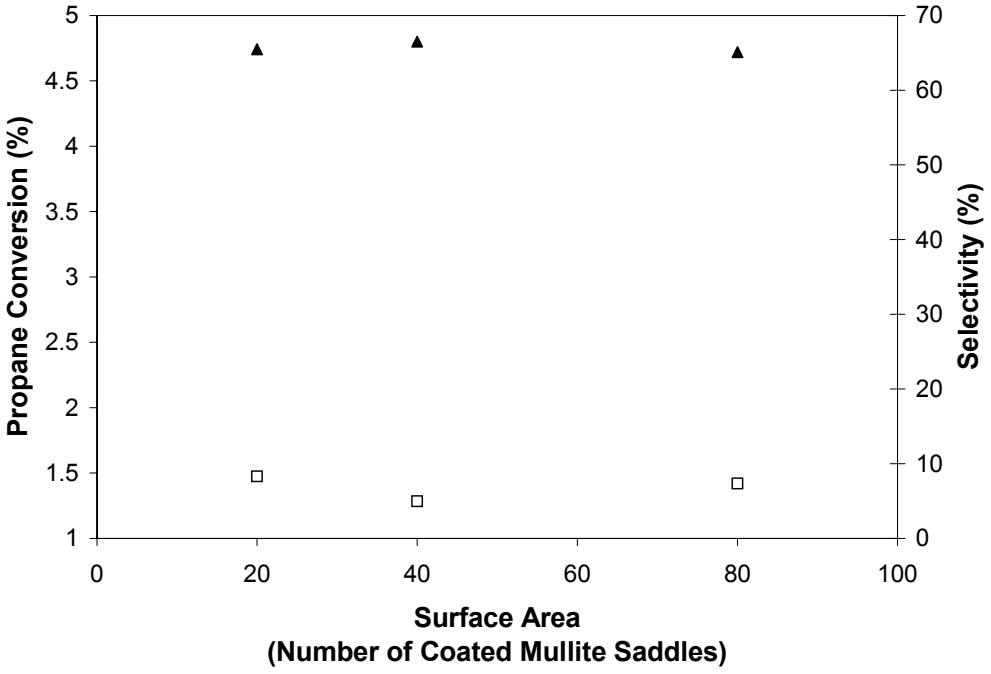

Figure 97. Propane conversion (open squares) and selectivity (filled triangles) of a Pt/Sn dehydrogenation catalyst used with a layered composite hydrogen separation membrane as a function of catalyst surface area.

In conclusion, several different hydrogen separation membranes were tested under a variety of different conditions for membrane promoted alkane to olefin conversion. While some conversion of alkanes to olefins was observed, the membranes did not appear to promote this process under the test conditions. It is expected that under the correct pressures, flow rates, and in the presence of an appropriate catalyst, these membranes would promote alkane conversion.

VI. Task 7 Candidate Membrane Compositions for Scale Up

Three basic categories of membranes were developed in this project: i) ceramic or ceramic/ceramic composites ii) high-temperature ceramic/metal composites (cermets), and iii) intermediate-temperature layered composite membranes. A comparison of these types of membranes was presented in Table 1. The ceramic/ceramic composites demonstrated the lowest hydrogen permeation rates, with a maximum of approximately 0.1 mL/min/cm^2 for 0.5-mm thick membranes at 800 to 950°C. Under equivalent conditions, cermets achieved a hydrogen permeation rate near 1 mL/min/cm^2, and the metal phase also improved structural stability and surface catalysis for hydrogen dissociation. Furthermore, if metals with high hydrogen permeability were used in cermets, permeation rates near 4 mL/min/cm^2 were achievable with relatively thick membranes. Intermediate-temperature composites demonstrated the highest permeation rates at the lowest temperature.

In order to address the appropriate membranes for scale up, NORAM completed an evaluation matrix for comparing Eltron's different membrane types and competing hydrogen separation technologies such as porous stainless steel membranes and pressure swing adsorption. The evaluation matrix and accompanying analysis is included in Appendix C.

A. Compilation of Relevant Data and Selection of Candidate Membrane Compositions

Collection of permeation and relevant data for candidate membrane compositions is described in detail under Tasks 1-4. Table 1 summarized the key performance data for each type of membrane investigated.

B. Raw Material Specifications and Suppliers

See Appendix C.

C. Key Conditions and Control Parameters

Key conditions and control parameters for processing of ceramic, cermet, and intermediate temperature composite hydrogen separation membranes include starting material purity, processing temperature, processing time, and processing atmosphere for both calcining and sintering steps. In addition, appropriate catalyst selection and deposition method is also critical.

Several ceramics and cermets were evaluated by CoorsTek with respect to manufacturing issues. CoorsTek initiated cost effective manufacturing development using $BaCeO_3$ as a representative perovskite-based hydrogen separation material. The process for fabricating

$BaCeO_3$ was transferred from Eltron to CoorsTek and optimized at CoorsTek to yield maximum fired density. This fired density was 5.93 g/cm^3 and the material was determined to be single phase $BaCeO_3$. In powder form for the purpose of checking powder true specific gravity, the density was observed to decrease in flowing He indicating that a gas species desorbs from the $BaCeO_3$ over time. This change in density was not observed on fired parts. However, additional tests are being run to determine the nature of this species and to determine if this will affect the properties of the fired parts. Mobility measurements performed at Eltron are used to confirm that equivalent performance was achieved. CoorsTek will fabricate additional batches of this formulation to verify reproducibility of the process.

The second family of materials transferred from Eltron to CoorsTek was a transition metal-substituted perovskite. Two formulations were transferred to CoorsTek, generalized in this text as $AB_{0.7}B^a_{0.3}O_{3-\delta}$ and $AB_{0.2}B^a_{0.8}O_{3-\delta}$. It became evident during processing that the $AB_{0.2}B^a_{0.8}O_{3-\delta}$ formulation resulted in multiple complex phases with no ABO_3 phase present, so further development of this formulation was discontinued. High densities were obtained with the $AB_{0.7}B^a_{0.3}O_{3-\delta}$ formulation. Initial x-ray diffraction measurements indicated that this material sinters with two phases present, a B^a-rich phase having an elongated grain structure and a B^a-deficient phase, as the continuous matrix phase. Further elemental analysis of B^a, A and B cation distribution within the complex microstructure is being pursued. This offers the interesting possibility that the mobility of this material can be altered significantly by varying the relative volume percent of the two phases if one phase, in fact, exhibits higher ionic conduction. This composition in calcined or sintered powder form also exhibited the decrease in density with time, similar to the phenomenon exhibited by $BaCeO_3$ indicating that a gas species is desorbing.

Eltron selected two cermet formulations for transfer to CoorsTek - a $AB_{0.7}B^a_{0.3}O_{3-\delta}$ / 44 wt.% metal formulation and a $AB_{0.8}B^c_{0.2}O_{3-\delta}$ / 44 wt.% metal formulation. Processing has been initiated on the B^c-modified formulation first to be followed by the B^a-modified formulation.

In an effort to develop processes for these formulations that conform to typical ceramic manufacturing processing methods for high volume cost effective processing, aqueous processing was evaluated. Eltron has developed all of its formulations based on a non-aqueous process, utilizing isopropanol for batch milling and acetone for binder addition. Typical conventional processing of ceramic materials is carried out using aqueous based systems prior to spray drying of powders for part fabrication. Although it is usually more cost effective to use aqueous processing, non-aqueous systems are also used in cases where that is not possible. Tape casting of ceramic substrates is an example of a high volume manufacturing process that is based on non-aqueous processing. In the first series of tests using an aqueous system for the $BaCeO_3$ formulation, it was determined that the calcined powders could not be dispersed effectively for milling in water. The suspensions flocculated even when using dispersants. When the formulation was milled without dispersants, it exhibited a pH greater than 13. Milling at low solids content was pursued and traditional polyglycol binders were added; however, processed powders would not compact very well and sintered poorly with many defects such as cracks. Also XRD patterns of the calcined powders milled in water showed the presence of additional phases including $BaCO_3$, $Ba(OH)_2 \cdot H_2O$ and $Ba(OH)_2 \cdot 3H_2O$, which explain the poor powder processing and sintering characteristics. At this point, it appears that an alcohol based process, currently being used for a lab-scale process, will need to be developed for larger-scale applications.

Sintering of cermet compositions is performed under reductive conditions (*i.e.,* H_2) to avoid oxidation of the metal phase. To improve the safety and economics of this manufacturing step, it was desirable to maintain the H_2 concentration as low as possible. Accordingly, the effect of the sintering atmosphere on cermet membrane characteristics was determined at CoorsTek by sintering a selected composition using nitroneal gas (25% H_2/bal. N_2) and forming gas (3% H_2/bal. Ar).

The membrane composition used for these tests is represented as $AB_{0.8}B^c_{0.2}O_{3-\delta}$/44 wt.% metal. XRD analyses of each sample revealed both the ceramic and metal phases. However, the XRD pattern of the ceramic phase for the sample sintered under forming gas was identical to the parent ABO_3 ceramic, whereas the sample sintered under nitroneal demonstrated peak broadening and shifting. These results indicated a greater degree of crystallographic distortion from cubic symmetry for the sample produced under more reductive conditions, which is consistent with a greater degree of oxygen vacancies.

SEM images (not shown) of samples sintered under both gases clearly demonstrated distinct regions of metal phase several microns in diameter surrounded by the ceramic phase. Although continuity of the metal phase was not apparent in the two-dimensional SEM images, continuity was confirmed using ohmmeter measurements across the membrane surface. The perimeter of each region of metal phase contained a boundary layer roughly 1 μm in thickness. EDX measurements of the boundary layer indicated diffusion of the metal phase into the ceramic phase. The extent of metal diffusion was nearly equivalent for both samples, but possibly a little greater for the sample sintered under nitroneal. Additionally, the sample sintered under nitroneal had a slightly smaller grain size, and demonstrated intergranular fracture on SEM fracture cross section analysis.

The $AB_{0.8}B^c_{0.2}O_{3-\delta}$/44 wt.% metal samples prepared by CoorsTek were tested at Eltron for H_2 permeation, and the results are presented in Figures 98 and 99. For comparison, results for the same composition prepared at Eltron and sintered under 10 vol.% H_2(bal. Ar) also were included. As indicated in the figures, the sample sintered under forming gas had considerably higher H_2 permeation and corresponding mixed proton/electron (apparent) conductivity than the sample sintered under nitroneal. Furthermore, results from the Eltron sample supported the apparent relationship between H_2 concentration during sintering and resulting H_2 permeation (of course, differences between the Eltron and CoorsTek samples might reflect other subtle variations in membrane preparation). These results were consistent with the characterization data, and it is concluded that the higher H_2 concentration during sintering creates more oxygen vacancies that distort the ABO_3 lattice and lead to inhibited grain growth and weaker grain boundaries. These factors lead to asymmetry, which likely decreases H_2 permeation by creating unequal lattice sites along the proton conduction pathway.

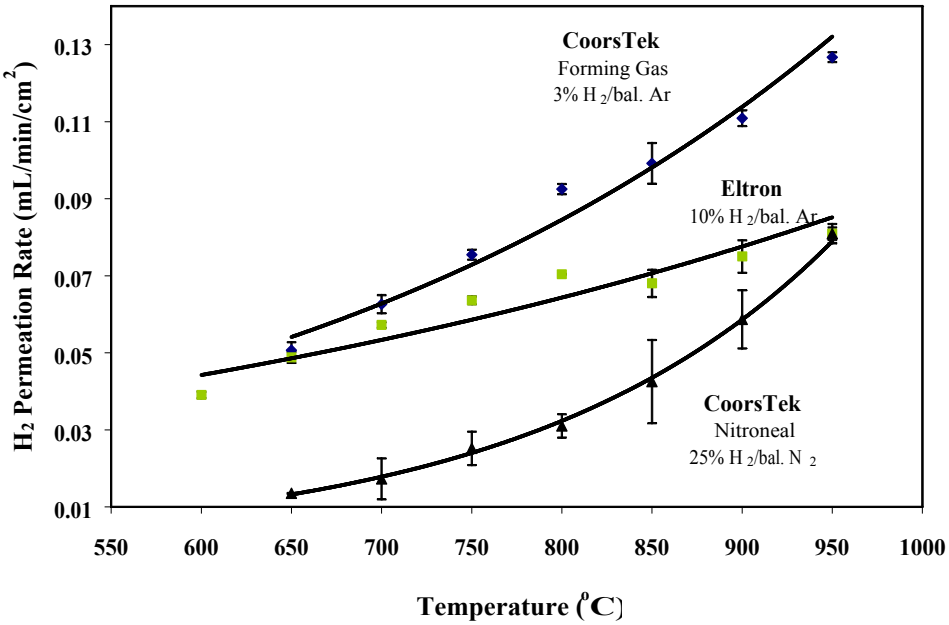

Figure 98. **Plot showing H_2 transport versus temperature for samples sintered under different H_2 concentrations (vol.%). Testing was performed with humid 80 vol.% H_2 (bal. He) on the inlet, and a sweep of Ar on the outlet. Membrane thicknesses were > 1 mm.**

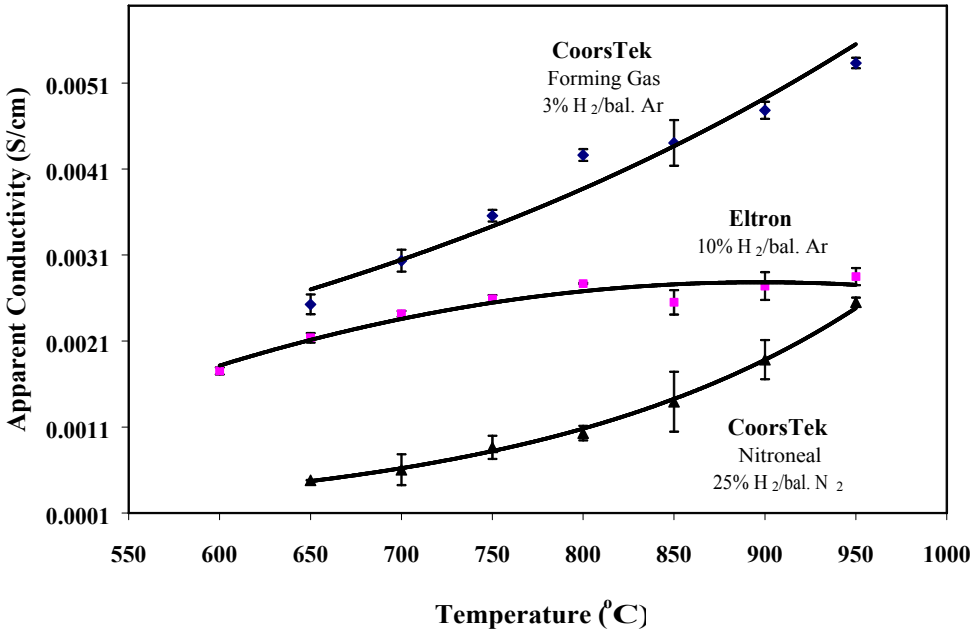

Figure 99. **Plot showing mixed proton/electron (apparent) conductivity versus temperature for samples sintered under different H_2 concentrations (vol.%). Testing was performed with humid 80 vol.% H_2 (bal. He) on the inlet, and a sweep of Ar on the outlet. Membrane thicknesses were > 1 mm.**

Ceramic and cermet materials evaluated in terms of manufacturing are summarized below.

1. B^a-Substituted ABO_3

a. Ceramic: $AB_{0.2}B^a_{0.8}O_{3-\delta}$

Fabrication. The optimum firing condition determined for this formulation was ~1475°C. The density of this formulation was ~ 6.0 g/cc. A decision to stop further development work on this formulation was made due lack of a hydrogen ion conducting phase and chemical instability of secondary phases.

b. Ceramic: $AB_{0.7}B^a_{0.3}O_{3-\delta}$

Fabrication. The optimum firing condition determined for this formulation was ~1475°C. The fired density of this formulation was ~6.2 g/cc. Fired parts exhibited a ABO_3 phase and at least one additional unidentified phase. This material demonstrated good separation and transport properties. Since there are applications that contain significant quantities of S in the feedstream, Eltron recommended that we revisit ceramic materials with better S tolerance than the metal phase of the cermets. Ceramic materials such as this one will be evaluated in parallel with the cermet materials.

c. Cermet: $AB_{0.7}B^a_{0.3}O_{3-\delta}$/44 wt.% Metal

Fabrication. This formulation was sintered in forming gas (3% H_2/ 97% Ar) at 1100°C/4hrs. The fired density was ~7.05 g/cc. Cracking was observed on parts made with this formulation when they were fired at higher temperatures.

Microstructure. SEM/EDS analyses revealed a fine grain structure. The metal phase showed solubility in the ceramic phase. An ICP analysis of metal beads showed the presence of major B^a with a trace of A and B.

Stability. Delayed cracking was observed on these samples. This effect was directly attributed to the environmental conditions for sample are storage. Delayed cracking was observed on samples stored under ambient conditions at Eltron and at CoorsTek. Cracking was not observed on samples stored in a desiccator at Eltron and at CoorsTek for several weeks, but after 6 weeks, some cracks were apparent. XRD measurements on the surface of parts before and after cracking exhibited the same metal and ABO_3 phases.

Manufacturing. The process was repeated with 4% H_2 certified forming gas. It yielded good reproducibility with respect to fired density and XRD.

Performance Testing. Conductivity and H_2 permeation tests were conducted on these samples. The results were fair as shown in Table 10.

Table 10.
Summary of Performance Evaluation for Selected Membranes Manufactured by CoorsTek.

Composition	Sintering Conditions	Max. Ambipolar Conductivity (S/cm)	Max. H_2 Permeability* ($mL \cdot min^{-1} \cdot cm^{-2}$)
$AB_{0.8}B^c_{0.2}O_{3-\delta}$ / 44 wt.% Metal	Forming Gas 1415°C	0.0053	0.13
$AB_{0.8}B^c_{0.2}O_{3-\delta}$ / 44 wt.% Metal	Nitroneal Gas 1425°C	0.0026	0.08
$AB_{0.9}B^a_{0.1}O_{3-\delta}$ / 44 wt.% Metal	Forming Gas 1375°C	0.0013	0.06
$AB_{0.7}B^a_{0.3}O_{3-\delta}$ / 44 wt.% Metal	Forming Gas 1100°C	0.0012	0.04
$AB_{0.7}B^a_{0.3}O_{3-\delta}$ / 44 wt.% Metal	Forming Gas 1100°C	0.0009	0.03
$AB_{0.9}B^a_{0.1}O_{3-\delta}$ / 44 wt.% Metal	Forming Gas 1375°C	0.0006	0.02

* Relatively thick membranes – approximately 1 mm. Test performed at 850 - 950°C.

d. Ceramic: $AB_{0.9}B^a_{0.1}O_{3-\delta}$

Fabrication. This composition was evaluated at various calcining temperature conditions to improve the subsequent grinding of the composition for making the corresponding cermet composition. The ceramic formulation was sintered to determine its microstructure. Parts were sintered at 1350°C/2 hrs, 1325°C/2 hrs and at 1300°C/2 hrs. The parts sintered in forming gas at 1300°C/2 hrs yielded a fired density of 5.98 g/cc and the parts sintered in air at 1300°C/2 hrs yielded a fired density of 6.26 g/cc. This difference in density might reflect some lack of stability of the B^a-modified perovskite processed in forming gas.

Microstructure. The samples fired in forming gas displayed the same layered, laminated structure as the cermet based on this material. The samples fired in air did not exhibit the layered, laminated structure but did show a small amount of a second phase and some porosity.

Stability. The samples fired in forming gas hydrolyzed rapidly and disintegrated on polishing. It appears that firing B^a-doped parts in hydrogen is not a good process.

e. Cermet: $AB_{0.9}B^a_{0.1}O_{3-\delta}$/44 wt.% Metal

Fabrication. These parts were sintered at 1425°C/4hrs. A single metal bead was formed on the top surface of each of the parts. Lower sintering temperatures were tested on this series. At 1400°C/4hrs, the beads were still present. At 1375°C/4hrs, the beads were generally eliminated. These conditions resulted in a fired density of 7.07 gm/cc. Parts, however, will be sintered at temperatures below 1375°C to determine if the layered laminate structure can be eliminated and if the B^a can be stabilized in the perovskite phase and not in the metal phase where it appears to be migrating.

Microstructure. SEM images were conducted on the first batch fired without metal beads. The microstructure was not uniform with the ABO_3 phase distributed as both a normal appearing phase and as a layered, laminated structure with neither phase showing the presence of any B^a in an EDS analysis. XRD analyses indicated that ABO_3 and metal phases were the only phases present. EDS also showed a minor amount of B^a in the metal phase. Although only one phase was detected, the microstructure was not uniform and could prove to be a problem with respect to reproducibility. Lower firing temperatures will be evaluated in order to eliminate this problem.

Stability. No delayed cracking was observed on samples made with this formulation, however, the effect may occur over longer periods of time.

Manufacturing. If Eltron decides to proceed with this formulation, the working range will need to be determined and reproducibility will need to be established. The working range is the sintering temperature range over which acceptable performance is achieved on the final parts or components. A wide working range is desirable from a manufacturing perspective. Samples fired at the lowest temperature that still yield a uniform microstructure with few voids and no metal beads then should be measured for H_2 permeability to determine the optimum processing conditions.

Performance testing. H_2 permeation tests were conducted on these samples as shown in Table 10. The results are similar to the $AB_{0.7}B^a_{0.3}O_{3-\delta}$/44 wt.% metal cermet composition, and also were not as good as the B^c-substituted series. The two $AB_{0.9}B^a_{0.1}O_{3-\delta}$/44 wt.% metal cermet samples did not reproduce well, possibly because the low concentration of B^a was difficult to disperse evenly throughout the structure.

2. B^c-substituted ABO_3

a. Ceramic: $AB_{0.8}B^c_{0.2}O_{3-\delta}$

Fabrication. Samples were fired in both nitroneal (25% H_2) and forming gas (3% H_2) atmospheres to determine a baseline for comparison to the cermet composites when metal is added to these compositions. Samples fired in dry nitroneal (25% H_2 / 75% N_2) exhibited one major ABO_3 phase with peak shifting and line broadening. Samples fired in forming gas (3% H_2 / 97% Ar) also exhibited one major ABO_3 phase, however, peak shifting and line broadening were not present.

Manufacturing. A new batch was prepared and the sintered density reproduced well. The fired density of the $AB_{0.8}B^c_{0.2}O_{3-\delta}$ formulation was 6.07 g/cc.

b. Cermet: $AB_{0.8}B^c_{0.2}O_{3-\delta}$/44 wt.% Metal

Fabrication.

Atmosphere. This formulation was sintered in a refractory metal furnace using dry nitroneal gas (25% H_2 / 75% N_2) at 1425°C/4hrs. The fired density of this formulation was in the range 6.90-6.94 g/cc. Parts also were fired at 1425°C/4hrs in certified forming gas. Samples fired in nitroneal revealed two major phases. The first phase was metal. The second phase, as

with the ceramic sample, was ABO_3 with some peak shifting and line broadening. Samples fired in forming gas also revealed two major phases. The first phase was metal. Again, as with the ceramic sample, the second phase was ABO_3 with no peak shifting or line broadening. A decision will be made as to which firing atmosphere to use based on the results of H_2 permeation tests on samples fired in both atmospheres. Comparative analyses are underway to study elemental distribution between nitroneal and forming gas atmosphere firing cycles.

Metal Beads. Several test firings have produced parts with multiple metal beads on the surface in parts fired at 1425°C. Lowering the firing temperature to 1415°C/4 hrs eliminated severe metal bead formation. The microstructure near the metal beads was determined to be more porous than the microstructure when metal beads were not present. The metal leaves voids when it forms beads at the surface and leaves some residual metal present in the structure.

Whiskers. In the part fired in forming gas, fresh fractured surfaces revealed a very unusual phenomenon, the presence of whiskers. EDS of the whiskers revealed that they contained A, B, B^c, and O, but no metal. Attempts to reproduce whisker formation were unsuccessful. However, SEM images revealed, needle-like grains. An EDS analysis revealed that the needle-like grains contained the same constituents as the whiskers, except the metal. The needle-like structure might be formed by recrystallization of the ceramic phase.

Microstructure. The microstructure of parts fired at 1425°C/4 hrs in certified forming gas exhibited discontinuous grain growth and beads of metal. The microstructure of parts fired at 1415°C/4 hrs were more uniform and finer grained, however, an elongated structure that appeared to look like remnants of whiskers (needle-like grains) appeared present in all the microstructures. This effect will be investigated further. SEM images show that the ceramic phase contains a small amount of metal. However, the metal is clearly diffusing into the ceramic and very little or no ceramic elements diffused into the metal.

Manufacturing. The process was repeated on new batches fired at 1425°C/4 hrs and at lower temperatures. XRD and SEM data reproduced well. Parts fired at 1415°C/4 hrs and at 1410°C/4 hrs in certified forming gas addressed the metal bead formation problem favorably in providing a working range of the formulation. Even lower firing temperatures will be tested to determine the working range that yields a uniform microstructure. New samples fired in forming gas at 1415°C/4 hrs representing a change in firing temperature to eliminate the metal beads were sent to Eltron to measure H_2 permeation.

Performance Testing. These results were significantly better than the performance measurements for $AB_{0.7}B^a_{0.3}O_{3-\delta}$/44 wt.% metal. The sample sintered in forming gas at 1415°C yielded properties that were approximately twice as good as the sample sintered in nitroneal at 1425°C. The two variables need to be isolated in order to determine if the atmosphere or sintering temperature had the most significant effect.

c. Ceramic/Ceramic: $AB_{0.8}B^c_{0.2}O_{3-\delta}$/CER1

Fabrication. Two paths are being pursued in parallel to develop this material. CoorsTek is fabricating the individual perovskite proton-conducting and electron-conducting (CER1)

phases separately, then sintering them together. Eltron is fabricating the two-phase material using a single formulation, followed by sintering. Initial attempts to prepare this material resulted in undesirable reaction with the setter powder. An alternative setter powder was identified and preliminary batches of this composition were prepared.

A composition containing 60% $AB_{0.8}B^c_{0.2}O_{3-\delta}$ and 40% CER1 was formulated and sintered at 1375°C/4hrs and at 1390°C/4hrs in air. The sintered densities were 5.73 g/cc and 5.77 g/cc, respectively. Parts sintered at 1410°C/4hrs in air yielded slightly higher sintered densities of 5.83 g/cc. SEM/EDS analyses revealed the presence of two phases, but some of the B^c diffused into the CER1 phase. Furthermore, these samples were brittle.

In an attempt to offset loss of proton conductivity from B^c diffusion, a formulation having a 75/25 ratio has been processed. Eltron estimated the maximum ratio to be 80/20 in order to maintain continuity in the electronically conducting phase. Parts sintered at 1410°C/4hrs in air also yielded sintered densities of 5.83 g/cc. SEMs revealed a microstructure similar to the 60/40 samples. XRD analyses showed the presence of an ABO_3 phase and an unidentified second phase. EDS analyses indicated that some diffusion of constituent cations. Also, XRD patterns indicated that the CER1 component was a mixture of brownmillerite and perovskite phases. This result was not desired since the differences in the crystal structures might compromise structural stability.

3. B^b-substituted ABO_3

a. Ceramic: $AB_{0.8}B^b_{0.2}O_{3-\delta}$

Fabrication. The initial formulation was prepared with by calcining at 1250°C/4 hrs. This condition resulted in hard agglomerates. Calcining at 1200°C/4 hrs resulted in the same very hard agglomerates still being formed indicating that some melting occurred. Test sintering cycles conducted at 1120°C/4 hrs and 1100°C/4 hrs in air resulted in porous parts. Tests carried out at 1150°C/4 hrs and 1175°C/4 hrs appeared to have solved the porosity problem. These samples were sent to Eltron.

Microstructure. Powders calcined at 1250°C/4 hrs consisted of the primary ABO_3 phase and some unidentified secondary peaks. The peaks appeared at 31 $^o2\theta$. Eltron identified a $AB^bO_{2.6}$ phase at 26° 2θ, which was observed in one of the samples. So, it is possible that the peak at 31° 2θ is indicative of a different AB^bO_x phase. SEM images of samples fired at 1150°C/4 hrs revealed the presence of the primary BaCeO3 phase and most, but not all of the secondary peaks observed in the calcined powders. Parts sintered at 1175°C/4 hrs exhibited the same phases as the parts sintered at 1150°C/4 hrs. On the 1150°C/4 hrs sintered composition, EDS showed the lighter phase to contain A, B with no B^b. The darker phase revealed A, B^b and no B. On the 1175°C/4 hrs parts, EDS showed similar phases to that observed in the 1150°C/4 hrs samples. It appeared that the B^b addition was not substituting in the perovskite structure, but rather segregated as an unidentified BO-B^bO phase. A sample fabricated by Eltron that was sintered at 1190°C/2 hrs showed the same XRD pattern with two small peaks at 31°2θ. It was confirmed by EDS that the darker phase contains B^b and the lighter phase does not. This effect is desirable since the darker B^b-containing second phase is likely to be electronically conducting resulting in a ceramic/ceramic composite.

b. Cermet: $AB_{0.8}B^{b}_{0.2}O_{3-\delta}$/44 wt.% Metal

This cermet composition has been discussed with Eltron, but has not been prepared yet. Eltron will provide direction regarding current interest in this composition. The low required sintering temperature for this composition and the formation of the B^b-containing minor phase are difficulties that need to be overcome in addressing the formulation of a cermet.

4. B^d-substituted ABO_3

a. Ceramic: $AB_{0.8}B^{d}_{0.2}O_{3-\delta}$

This formulation was calcined at 1250°C/2hrs. XRD analysis confirmed that the material a single-phase perovskite. Parts made from this calcine will be sintered later if necessary, but the higher priority initially is to make the metal cermet for a comparison to the $AB_{0.8}B^{c}_{0.2}O_{3-\delta}$/metal analogs.

b. Cermet: $AB_{0.8}B^{d}_{0.2}O_{3-\delta}$/44 wt.% Metal

This formulation was sintered at 1380°C/4hrs in forming gas. The parts appeared dense and did not show evidence of setter reaction. Three samples having fired densities of 7.11 g/cc, 7.12 g/cc and 7.12 g/cc, respectively were sent to Eltron for performance measurements and comparison to the $AB_{0.8}B^{c}_{0.2}O_{3-\delta}$/metal analog (see above). This composition had a tendency to form metal beads at sintering temperature >1400°C in a manner similar to the $AB_{0.8}B^{c}_{0.2}O_{3-\delta}$/metal cermet. The maximum sintering temperature that could be used to process these parts without forming metal beads was determined to be 1400°C. The microstructure was similar to the $AB_{0.8}B^{c}_{0.2}O_{3-\delta}$/metal analog and contained a similar needle-like structure likely indicative of recrystallization. Additionally, a higher-density layer of the same composition as the bulk formed over the part.

VII. Task 8 Manufacturing Processes for Demonstration-Scale Hydrogen Separation Membranes

Two different manufacturing processes were examined in Task 8 for production of hydrogen separation membranes on a large scale.

A. Dense Tubular Ceramic Membranes

Extrusion was examined for preparation of dense thick tubular membranes. Formulations and procedures were developed. Due to the higher performance of thin films, work in Task 8 focused mainly on processes for deposition of thin film cermets on porous supports as described below.

B. Manufacturing Processes for Supported Membranes

Development of hydrogen separation membranes consisting of dense thin films of BCY/Ni cermet adhered to porous BCY/Ni porous tubular supports was discussed in detail in Task 4c. CoorsTek developed a thin film deposition procedure for the application of BCY / Ni thin films ranging from 10 to 100 μm onto the inner surface of a tubular support. An example of a sintered porous tube with a dense thin film of BCY/Ni on the inner surface is shown in Figure 100. Variables optimized in this procedure included slurry composition and application technique, sintering temperature, time, and atmosphere. This procedure is easily adaptable to manufacturing scale; however, the permeability of BCY / Ni materials will limit its commercial potential. New cermets based on high permeability metals also have potential; however, these cermets are in an early stage of development. The developed procedures for BCY/Ni thin film deposition will easily be adaptable to the new class of cermets.

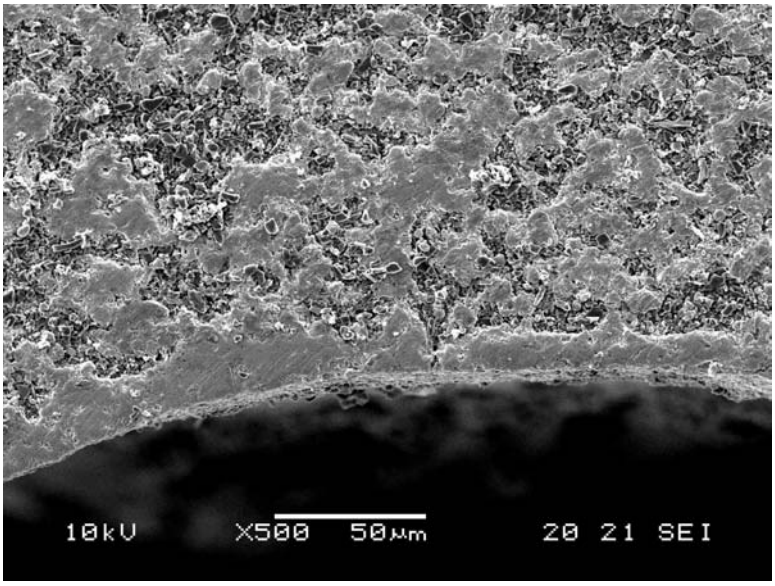

Figure 100. x500 SEM image of a thin BCY/Ni dense film applied to a porous closed-one-end tube.

Both of the manufacturing processes described above were developed with the long term intension of being able to substitute new cermet compositions based on high permeability metals into an optimized processes. New sintering temperatures, times, and atmospheres would have to be adjusted for new hydrogen membrane compositions, however, the basic process will already have been developed.

VIII. Task 9 Fabrication and Evaluation of Demonstration-Scale Hydrogen Separation Unit

A ten fold scale up was originally proposed for a demonstration scale hydrogen separation unit. At the time ceramic tubes were expected to be the best performing membrane material. Three ceramic tubes would be manifolded together to demonstrate scale up. Over the course of the project it was determined that planar composite layered membranes performed much better than ceramics. Therefore, in Task 9, scale-up was demonstrated on planar composite layered membranes rather than ceramic tubular membranes.

Permeation testing was performed on scaled-up composite layered membrane with a surface area of 31.7 cm^2. This represents a fifteen fold scale-up compared to Eltron's standard two cm^2 membrane size. A reactor was constructed including appropriate furnace elements, plumbing, and analysis to accommodate this size membrane. Permeation testing was performed at 420^oC and at feed pressures up to 150 psig. A hydrogen helium feed stream up to 12.5 L/min

was fed to the retentate side of the membrane and argon was used on the permeate side of the membrane to facilitate GC analysis. Permeation results are shown in Figure 101. Results showed a maximum permeation up to 51 mL•min^{-1}•cm^{-2} which can be extrapolated to a hydrogen separation rate of 0.46 lbs H_2 / day. Figure 101 shows that the membrane was limited by gas phase diffusion. It is expected that fluid dynamic calculations and improved hardware design will lead to improved performance.

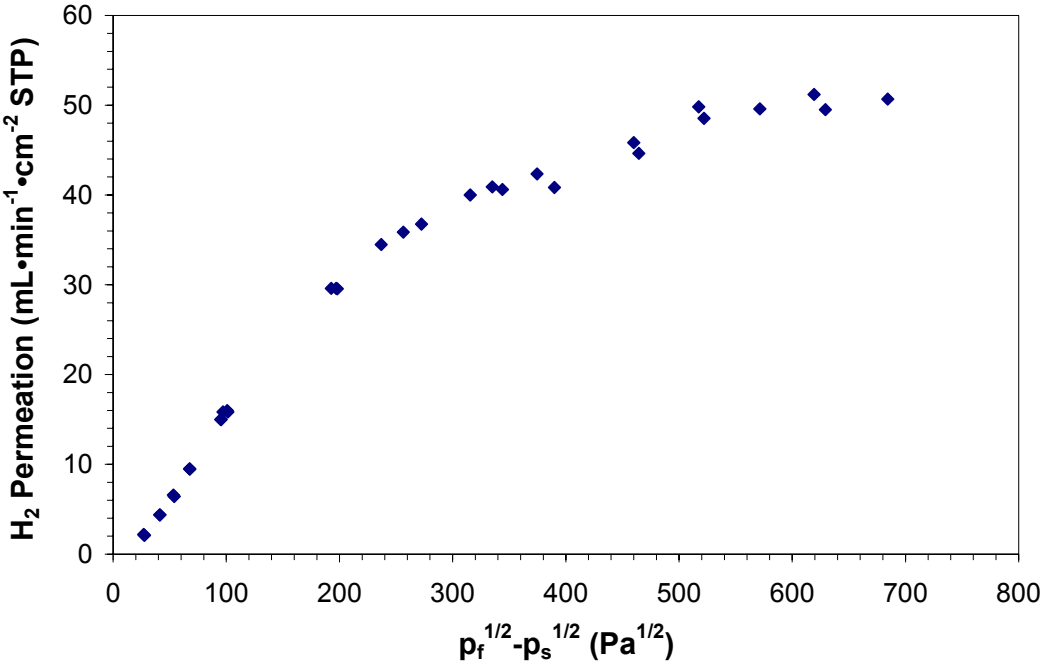

Figure 101. Plot of permeation vs. the difference in the square roots of the hydrogen partial pressure across the membrane.

CONCLUSIONS

As described above, Eltron Research Inc. exceeded or met all goals in the course of completing this project. Ceramic, cermet, and layered composite membranes were prepared and evaluated during this project. Hydrogen permeation was improved from 0.01 mL•min^{-1}•cm^{-2} for single phase ceramic membranes up to 423 mL•min^{-1}•cm^{-2} for layered composite membranes tested at high pressures. In addition, thin film membranes were prepared, surface catalysis and the effect of impurities was investigated, membranes were tested up to 1000 psig feed pressure, the economics of membrane scale-up and manufacture were determined, and the appropriate engineering documentation was completed. The results of this project led to a new DOE funded program as part of the FutureGen initiative.

References:

1. Paglieri, S. N.; Way, J. D. *Sep. and Pur. Methods* **2002**, *31*, 1-169.
2. Iwahara, H.; Yajim, T.; Hibino, T.; Ozaki, K.; Suzuki, H. *Solid State Ionics* **1993**, *61*, 65.
3. Yajima, T.; Suzuki, H.; Yogo, T.; Iwahara, H. *Solid State Ionics* **1992**, *51*, 101.
4. Kreuer, K. D. *Solid State Ionics* **1997**, *97*, 1-15.
5. Balachandran, U., et al. *Development of Dense Ceramic Membranes for Hydrogen Separation*. In *26th International Technical Conference on Coal Utilization and Fuel Systems*, 2001, Clearwater, FL.
6. Siriwardane *et al. Appl. Surf. Sci.* **2000**, 167, 34.
7. Elshof *et al. J. Electrochem. Soc*. **1997**, 144, 4361.
8. Balachandran, U., T.H. Lee, and S.E. Dorris. *Development of Mixed-Conducting Ceramic Membranes for Hydrogen Separation*. In *Sixth International Pittsburgh Coal Conference*, 1999, Pittsburgh, PA.
9. Wachsman, E.D. and J. Naixiong, *Two-Phase Hydrogen Permeation Membrane. Patent No. 6,235,417*. 2001, Her Majesty the Queen in right of Canada: USA.
10. Roark, S.E., et al., *Mixed-Conducting Membranes for the Spontaneous Oxidative Dehydrogenation of Alkanes to Olefins (DOE SBIR Final Report, Contract No. DE-FG0397ER82571)*. 1999, Eltron Research Inc.: Boulder, CO.